# Substrate-bound and substrate-free outward-facing structures of a multidrug ABC exporter

Vincent Chaptal, Veronica Zampieri, Benjamin Wiseman, Cédric Orelle, Juliette Martin, Kim-Anh Nguyen, Alexia Gobet, Margot Di Cesare, Sandrine Magnard, Waqas Javed, et al.

BIOCHEMISTRY

# Substrate-bound and substrate-free outward-facing structures of a multidrug ABC exporter

Vincent Chaptal[1]†, Veronica Zampieri[1]†‡, Benjamin Wiseman[1,2]†§, Cédric Orelle[3]||, Juliette Martin[4]||, Kim-Anh Nguyen[5]||, Alexia Gobet[1]||, Margot Di Cesare[3]||, Sandrine Magnard[1], Waqas Javed[3]¶, Jad Eid[1], Arnaud Kilburg[1], Marine Peuchmaur[6], Julien Marcoux[7], Luca Monticelli[4], Martin Hogbom[2], Guy Schoehn[8], Jean-Michel Jault[3]#, Ahcène Boumendjel[5]#, Pierre Falson[1]*



**Multidrug ABC transporters translocate drugs across membranes by a mechanism for which the molecular features of drug release are so far unknown. Here, we resolved three ATP-$Mg^{2+}$–bound outward-facing conformations of the *Bacillus subtilis* (homodimeric) BmrA by x-ray crystallography and single-particle cryo–electron microscopy (EM) in detergent solution, one of them with rhodamine 6G (R6G), a substrate exported by BmrA when overexpressed in *B. subtilis*. Two R6G molecules bind to the drug-binding cavity at the level of the outer leaflet, between transmembrane (TM) helices 1–2 of one monomer and TM5′–6′ of the other. They induce a rearrangement of TM1–2, highlighting a local flexibility that we confirmed by hydrogen/deuterium exchange and molecular dynamics simulations. In the absence of R6G, simulations show a fast postrelease occlusion of the cavity driven by hydrophobicity, while when present, R6G can move within the cavity, maintaining it open.**

## INTRODUCTION

Multidrug ATP-binding cassette (ABC) exporters transport a large panel of drugs conferring a multidrug resistance (MDR) cell phenotype that leads to chemotherapy failures against pathogenic microbes and cancers. Early conceptualized (*1*) ABC exporters mainly switch between a high drug affinity inward-facing (IF) conformation in which the drug-binding pocket in the membrane domain is exposed to the inner membrane leaflet, and a low drug affinity outward-facing (OF) conformation, favoring drug release outside the cells. These proteins are made of two transmembrane domains (TMDs) typically built with 12 transmembrane helices and two nucleotide-binding domains (NBDs). Drugs bind to the TMD, accessible from the inner membrane leaflet in the IF conformation. Two ATP molecules bind at the interface between the two NBDs (*2*, *3*), thereby stabilizing the dimer and favoring the drug occlusion that leads the reorganization of the TMD in an OF conformation (*4*).

Several exporter structures have been obtained (*5*–*13*), complemented with biochemical and biophysical characterizations [e.g., (*14*–*16*)], together contributing to a mechanistic understanding of the IF-to-OF transition. Moreover, the molecular mechanism by which structurally divergent drugs and compounds bind to the IF conformation is presently better understood, thanks to the structure of the human ABCB1 in complex with the anticancer drug taxol (*14*). This structure revealed that the substrate recognition is driven by the intrinsic plasticity of TM4 and TM10, required to accommodate the structure of the drug.

The question remains open as to how the structural variability of those substrates is handled by MDR ABC exporters to expel them and which molecular features of the protein in the OF conformation are driving this release step (*17*). So far, since the first structure released in 2006 (*5*) and almost 50 years after their discovery (*18*), no OF structure of an MDR ABC exporter with a bound substrate has been solved. To that aim, the ATP-bound cryo-EM structure of ABCC1 in the presence of its substrate, leukotriene C4, was resolved, but the location of the substrate was not determined (*19*). Previously, the crystal structure of the antibacterial peptide transporter McjD was obtained in complex with adenylyl-imidodiphosphate (AMP-PNP), and two molecules of nonyl-glucoside that were used as crystallization additive were bound in the putative drug-binding cavity (*8*). Molecular dynamics simulation based on that structure predicted a marked flexibility of the TM1–2 region (*20*), pointing to a possible role of this region in the release of substrates. However, so far, structural information is lacking to corroborate this hypothesis, mainly because of the poor affinity of the transported substrate in the OF conformation.

Here, we tackled the question by resolving three OF conformations of BmrA, a type IV ABC transporter (*21*, *22*) from *Bacillus subtilis* (*23*) conferring resistance to cervimycin C, an antibiotic produced by *Streptomyces tandæ* against gram-positive bacteria (*24*). Using an ATPase inactive mutant, E504A (*25*), we resolved its x-ray structure in complex with ATP-$Mg^{2+}$, which required several key steps optimization and to design specific stabilizers. We also resolved its cryo–electron microscopy (cryo-EM) structure in complex with

[1]Drug Resistance and Membrane Proteins Group, Molecular Microbiology and Structural Biochemistry Laboratory, CNRS UMR 5086, University of Lyon, IBCP, 7, passage du Vercors, 69367 Lyon, France. [2]Department of Biochemistry and Biophysics, Arrhenius Laboratories for Natural Sciences, Stockholm University, Stockholm, Sweden. [3]Bacterial Nucleotide-Binding Proteins Group, Molecular Microbiology and Structural Biochemistry Laboratory, CNRS UMR 5086, University of Lyon, IBCP, 7, passage du Vercors, 69367 Lyon, France. [4]Modeling Biological Macromolecules Group, Molecular Microbiology and Structural Biochemistry Laboratory, CNRS UMR 5086, University of Lyon, IBCP, 7, passage du Vercors, 69367 Lyon, France. [5]University of Grenoble Alpes, INSERM, LRB, 38000 Grenoble, France. [6]University of Grenoble Alpes, CNRS, DPM UMR 5063, 38041 Grenoble, France. [7]Institut de Pharmacologie et de Biologie Structurale (IPBS), UMR 5089, Université de Toulouse, CNRS, UPS, 31000 Toulouse, France. [8]University of Grenoble Alpes, CEA, CNRS, IBS, F-38000 Grenoble, France.
*Corresponding author. Email: pierre.falson@univ-lyon1.fr
†These authors contributed equally to this work as co-first authors.
‡Present address: European Molecular Biology Laboratory, 71 Avenue des Martyrs, CS 90181, 38042, Grenoble, Cedex 9, France.
§Present address: Department of Biosciences and Nutrition, Karolinska Institutet, Huddinge, Sweden.
||These authors contributed to this work as co-second authors.
¶Present address: University of Grenoble Alpes, CEA, CNRS, IBS, F-38000 Grenoble, France.
#These authors contributed to this work as co-penultimate authors.

ATP-$Mg^{2+}$ and rhodamine 6G, a lipophilic cationic substrate of exporters, either from the ABC superfamily such as LmrA, a close homolog of BmrA (*26*), Cdr1 (*27*), Pdr5 (*28*) in yeast, and *Cyanidioschyzon merolæ* ABCB1 (*15*), or from Bmr and Blt, two other MDR transporters of *B. subtilis* (*29*), and AcrB of the resistance nodulation cell division (*30*). Comparison of the present structures enlightens how the drug binds before its release and shows how the flexibility of the TM1–2 segment drives this process, and this was confirmed by H/D exchange coupled to mass spectrometry (HDX-MS) and molecular dynamics simulations.

## RESULTS

### Crystal structure of BmrA in OF conformation in complex with ATP-$Mg^{2+}$

We first stabilized BmrA in its OF conformation by introducing the E504A mutation that prevents hydrolysis of ATP (*25*, *31*) and doxorubicin transport (fig. S1). The protein crystallized following the procedure setup for the mouse P-glycoprotein, using Triton X-100 for extraction and a mixture of *N*-dodecyl-β-D-*n*-maltopyranoside (DDM) and cholate for purification (*32*), which maintains a high ATPase activity level compared to DDM alone (fig. S1B). Quantification of detergents bound to BmrA (*33*) was helpful to produce high-quality crystals, as increasing cholate reduced the amount of DDM bound to BmrA up to 50%, which proportionally reduced the estimated detergent-belt size (Fig. 1A). Diffraction patterns of the resulting crystals displayed a lattice-doubling problem that prevented their processing and which we overcame by designing a series of tailored amphiphiles **3a**-**e** (Fig. 1B) with a scaffold based on glycosyl-substituted dicarboxylates surfactants (*34*). Of note, these additives increase the thermal stability of BmrA up to ~30°C for **3d** (Fig. 1C and data file S2), which helped produce better diffracting protein crystals (Fig. 1, D and E).

We reached 3.9-Å resolution for the BmrA E504A-ATP-$Mg^{2+}$ complex in detergent solution (Fig. 2, left; figs. S2 and S3; and table S1). Even if the overall 3.9-Å resolution of this x-ray structure is modest, the quality of the phases from the model yielded very good maps for this resolution. Two dimers of BmrA were found in the asymmetric unit, with a root mean square deviation (RMSD) of 0.7 Å over 525 residues (fig. S2). Electron densities of each transmembrane helix were good enough to position them unambiguously (fig. S3A). It was also the same for TM1 and its following loop, pointed in this study, observed in each monomer (fig. S3B). The structure displays the characteristic type IV fold of ABC transporters (*21*), in which the NBDs bind two ATP-$Mg^{2+}$ in a head-to-tail mode, capturing the BmrA-E504A mutant in complex with ATP-$Mg^{2+}$ in a typical OF conformation. The E504A mutation stabilizes the efflux pump in an OF prehydrolytic state, similar to the one displayed by the wild-type (WT) BmrA trapped in the transition state for ATP hydrolysis in the presence of vanadate (*35*). The extracellular side of BmrA displays an opening to a cavity likely corresponding to the drug-exit path. In the context of this study, the crystal structure shows that some residues of the loop connecting TM1 to TM2 make contacts between half of the monomers of chains B and C (fig. S2, C and D) and another moiety of another dimer, while the other half remains free of movement (chains A and D). This suggests that these contacts are not required for maintaining the conformation of TM1–2 and/or modify the structure. For all structures, TM1 and TM2 are visible (fig. S3B), and the electron density for the loop in between is continuous for chains C and D. For chains A and B, small linkers between the TM and the middle of the loop are missing, denoting some intrinsic flexibility, but nevertheless still present and observable

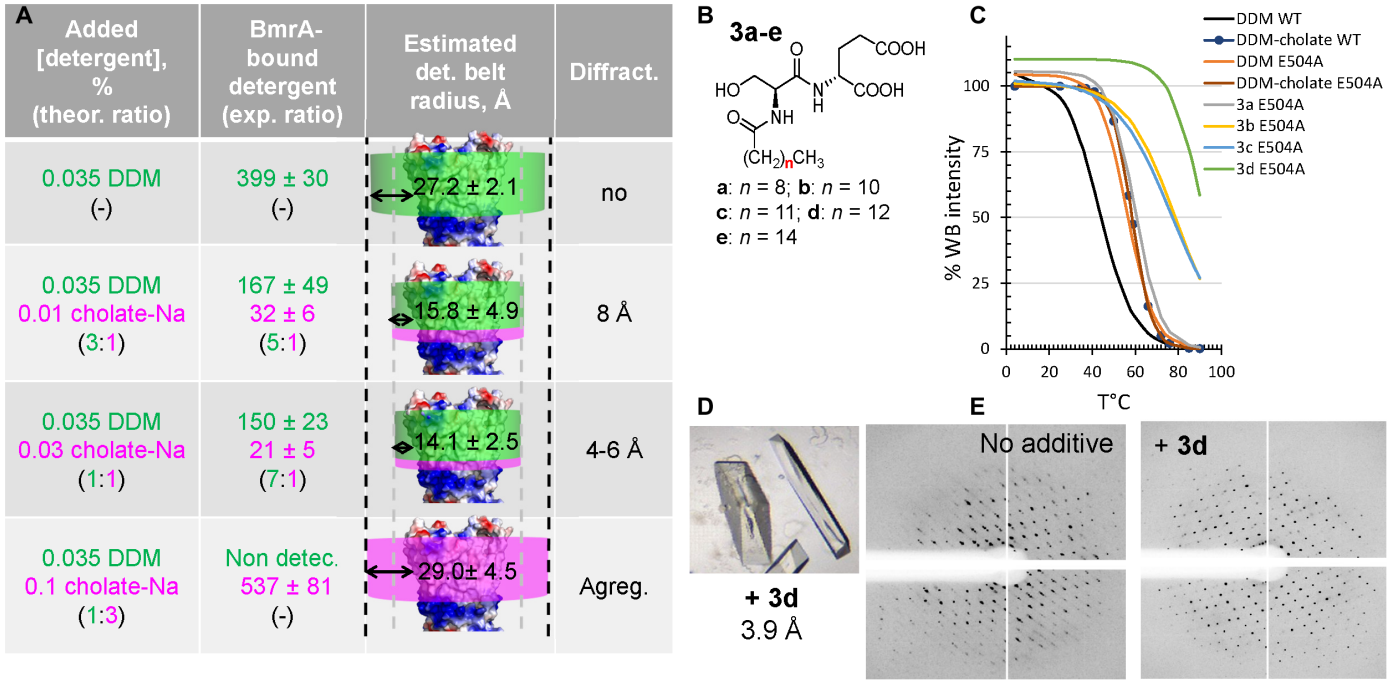


**Fig. 1. Crystallization of BmrA in detergent solution.** (**A**) Quantification of detergents bound to BmrA. See Materials and Methods and data file S1 for details. (**B**) Structure of the thermostabilizing amphiphilic additives. (**C**) Thermostabilization of BmrA. For clarity, fits (two to three independent assays) are displayed, with circles for the reference condition (DDM + cholate). Full data are provided in data file S2. (**D**) BmrA crystals in the presence of **3d**. (**E**) Lattice problem resolution with **3d**.

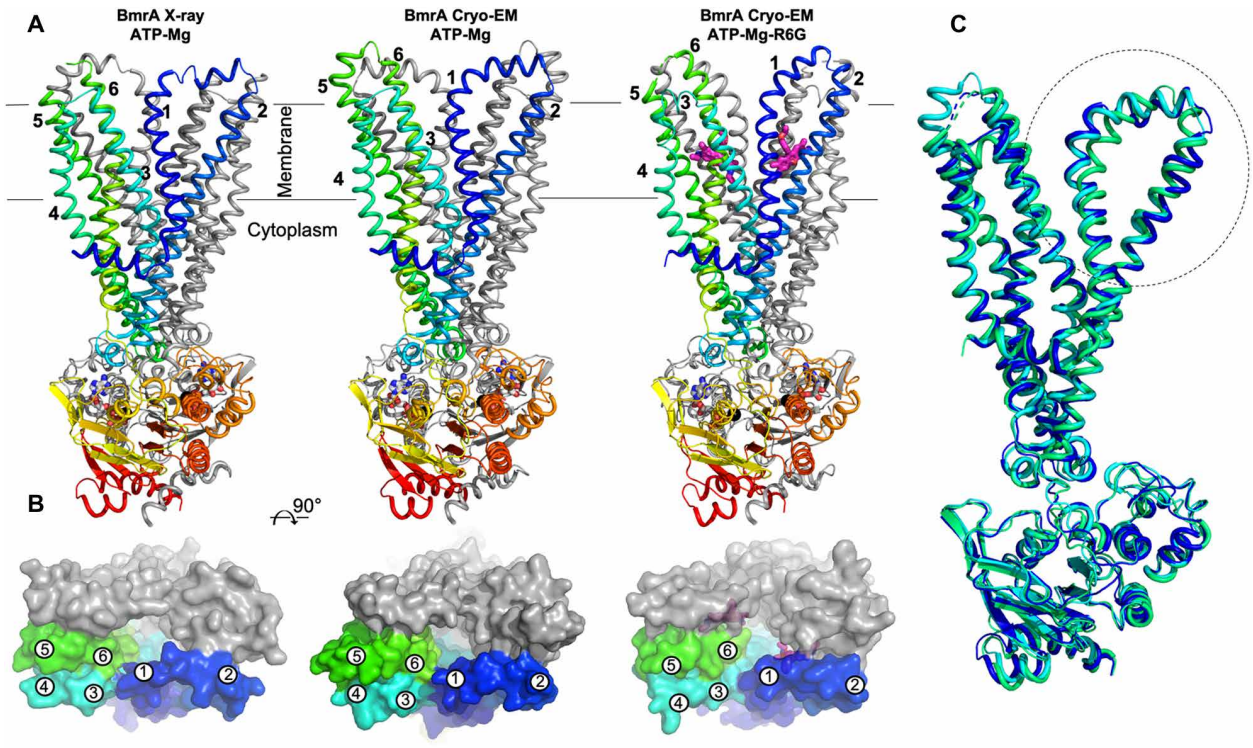


**Fig. 2. X-ray and cryo-EM structures of the BmrA E504A mutant in complex with ATP-$Mg^{2+}$ and R6G in detergent solution.** (**A**) Cartoons of the transporter normal to the plane of the membrane. One monomer is in gray, and the other one is rainbow colored. TM helices are numbered for the colored monomer. ATP and R6G are displayed as sticks colored by atom type and $Mg^{2+}$ as black sphere. (**B**) Surface representation of BmrA viewed from the extracellular side to highlight the difference in the OF cavity. (**C**) Superposition of the x-ray BmrA E504A [ATP-$Mg^{2+}$] (blue), cryo-EM BmrA E504A [ATP-$Mg^{2+}$] (cyan), and cryo-EM BmrA E504A [ATP-$Mg^{2+}$, R6G] (green).

when map contour is decreased. All the TM1–2 loops distribute around similar positions showing both the correctness of this position and the flexibility of this region (fig. S2E).

### Cryo-EM structure of BmrA in the OF conformation in complex with R6G and ATP-$Mg^{2+}$ in detergent solution

Incubating BmrA with known ligands (*23*) gave the best crystals with R6G. We could, however, not optimize them beyond 5 Å (fig. S4), leading us to move to single-particle cryo-EM (Fig. 2 and figs. S5 to S7). This approach allowed building the structure using the highest-resolution map using a C2 symmetry. Refinement up to 3.9 Å was carried out using both sharpened and unsharpened maps. Notably, the unsharpened map allowed observing the density corresponding to the TM1–2 loop (fig. S6). The resulting fold is very similar to that of the crystal structure with the difference in conformation of the region TM1–2 where TM1 is shifted toward TM2, resulting in a more pronounced opening of the cavity (Fig. 2B and table S2).

We observed two densities in the cryo-EM density map (Fig. 3A, bottom, and fig. S7CD), seen more clearly without the application of symmetry, and not present in the x-ray structure in which R6G was not added (Fig. 3A, top). To confirm this observation, we resolved by cryo-EM the structure of BmrA E504A in the same state, i.e., with ATP-$Mg^{2+}$ and without R6G (Fig. 2, center, and figs. S8 to S10). The resolution increased to 3.6 Å with a map of better quality, allowing to build a full model of BmrA including notably the TM5–6 loop, which was not resolved before. The x-ray and cryo-EM structures are similar, with 1.06-Å RMSD over 573 residues, especially at the level of the TM1–2 region (Fig. 2C and fig. S11). Last, as for the x-ray structure, no additional density could be observed in the cryo-EM structure at the level of those observed in the central cavity of BmrA in the presence of R6G (Fig. 3A, middle).

Given the limited resolution, R6G, cholate, or the polar head of DDM could be positioned in these densities. We therefore carried out a series of biochemical assays with the WT and E504A mutant to discriminate between these possible ligands. Both proteins were purified in DDM or DDM-cholate, followed by a reconstitution into nanodiscs (*36*), on which we probed the binding of the three compounds. When purified in DDM-cholate, BmrA E504A binds R6G with a modest affinity of ~13 μM but is two times better in the presence of ATP-$Mg^{2+}$ (Fig. 3C). The reverse effect was also observed, that is, ATP-$Mg^{2+}$ binding with a twofold higher affinity when R6G is added (Fig. 3C). When purified in DDM, both WT and mutant BmrA displayed a similar better affinity for R6G (4.8 ± 0.9 and 3.3 ± 0.7 μM, $P < 0.0001$), while no specific interaction could be detected with cholate (fig. S12A) or DDM (or decyl maltoside at higher concentrations) when carrying the binding experiments with BmrA reconstituted into nanodiscs (fig. S12B). In contrast, R6G binds to the BmrA-nanodisc complexes with affinities as high as ~0.07 ± 0.09 μM ($P = 0.4$) and ~0.03 ± 0.02 μM ($P = 0.1$) for WT and mutant, respectively. Of note, R6G binds to nanodiscs themselves with an affinity of 3 to 7 μM (fig. S12, C and D). These results indicate that cholate and DDM do not bind to the drug-binding site of BmrA in contrast to R6G affinity that seems to be partially attenuated in that case by the ATP. Together, this led us to assume that this density reveals the occupancy of R6G, as displayed in Figs. 2 and 3 (A and B) and fig. S7 (C and D).

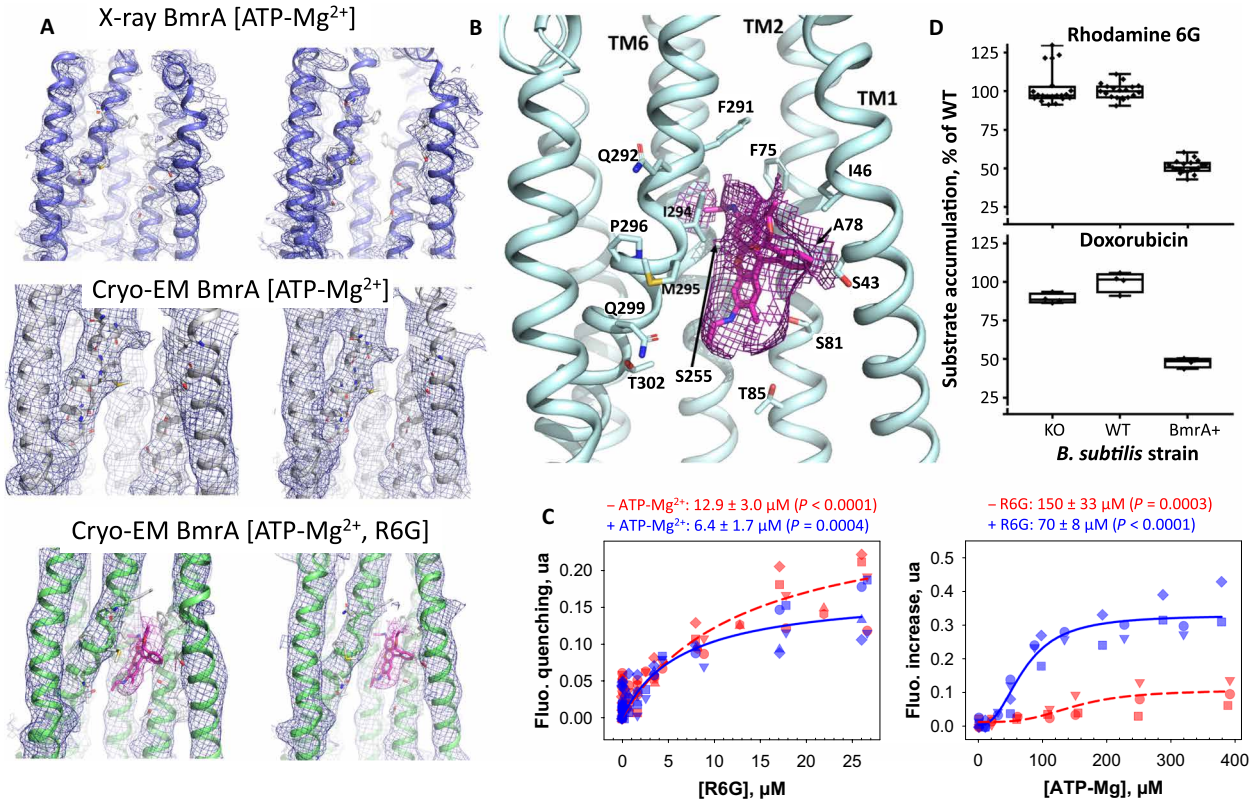


**Fig. 3. R6G in the cryo-EM structure of BmrA E504A, efflux, and binding.** (**A**) Superposition of the x-ray and cryo-EM structures and zoom in the two R6G regions. The x-ray map (2mFo-DFc) is displayed at 1σ and 0.8σ (EM BmrA E504A [ATP-$Mg^{2+}$] map) for the loop between TM1 and TM2. R6G structure and density are in magenta. (**B**) Detail of one R6G-binding site. (**C**) Binding of R6G (left) and ATP-$Mg^{2+}$ (right) to BmrA E504A in DDM-cholate probed by intrinsic fluorescence, in the presence (blue) or absence (red) of 5 mM ATP-$Mg^{2+}$ or 100 µM R6G, respectively. Symbols correspond to three to four independent experiments, fitted with equations S1 for R6G and S2 for ATP-$Mg^{2+}$. (**D**) R6G and doxorubicin accumulations in *B. subtilis* strains 168 ("WT"), KO for the gene coding for BmrA ("KO"), and 8R, a mutant of *B. subtilis* 168 strain overexpressing BmrA ("BmrA+"). Cells incubated with 5 µM substrate for 30 min at 37°C were then washed, lysed, and their intracellular fluorescence measured on supernatants, taking as reference the WT strain. Data are the average of 3 independent 3 to 10 replicates ($P < 10^{-10}$).

The observation above that R6G binding is enhanced by ATP-$Mg^{2+}$, even modestly, prompted us to investigate the possibility that BmrA could import R6G, since so far this molecule was only reported as a ligand of the pump (*23*). We therefore compared the intracellular accumulations of R6G and doxorubicin in three strains of *B. subtilis* previously described (*24*), either WT, invalidated for BmrA, or overexpressing BmrA (WT, KO, and BmrA+, respectively; Fig. 3D). While WT and KO strains display the same trends, the BmrA+ strain accumulates ~50% less each compound, therefore supporting the fact that R6G is a substrate of BmrA, which works as an exporter. Last, we also look at the stimulation of the ATPase activity of BmrA by the addition of substrates, but we could not detect any substantial effect of R6G, doxorubicin, or even Hoechst 33342 (fig. S12E), probably because of its high basal ATPase activity, as previously reported for this protein (*23*), and also for Cdr1 (*37*) and Pdr5 (*28*).

Two R6G molecules could be fitted in each density, although not in a perfect symmetrical position (Fig. 3A and fig. S7, C to F), explaining why the C2 symmetry does not improve those densities. R6G binds at the level of the outward leaflet, between TM1–2 of one monomer and TM5′–6′ of the other one. Each molecule is maintained in a hydrophobic cavity by a movement of TM1 toward TM2, mainly stabilized by van der Walls contacts with lateral chains of residues T39, S43, I46, F75, A78, I254′, S255′, L258′, F291′, I294′, and M295′. Few polar groups contribute also to the binding site including the alcohol group of S81, S225′, and T302′ and the carbonyl groups of A78, G251′, and F291′ (Fig. 3B and fig. S7, E and F). Such organization of the R6G pockets is close to that previously found in AcrB, together with the conformation of the R6G molecules themselves (fig. S7G). Several of these residues correspond to those found in the taxol-binding pocket of human ABCB1 in IF conformation (fig. S13) (*14*).

## Structural differences between the structures of BmrA with and without substrate highlight the mobility of the TM1–2 region

Although quite similar, these structures of BmrA display important local differences rendering the substrate-exit path substantially different between them (Fig. 2). The differences originate from a displacement of the TM1–2 region, in the proximity of a kink starting in TM1 at residue P47 toward the end of TM1. Such displacement allows the central part of TM1 to shift from TM3 in the x-ray/cryo-EM structure toward TM2 in the cryo-EM + R6G structure. These differences between structures solved under identical or nearly identical conditions highlight a major local plasticity at the level of TM1–2. To evaluate its structural relevance, we tentatively

compared these structures with a panel of nucleotide-bound exporters of the same subtype IV: *Escherichia coli* McjD (*8*, *11*), *Thermus thermophilus* TmrAB (*13*), human (*4*) and *C. merolæ* (*15*) ABCB1, *E. coli* MsbA (*16*), *Staphylococcus aureus* Sav1866 (*5*), and *Thermotoga maritima* TM287/288 (*38*). Although the structural disparity of these different proteins, positioning them from the most occluded to the widest open (Fig. 4, A and B), suggested that TM1 in the x-ray and cryo-EM structures of BmrA without R6G may be oriented similarly as in McjD, ABCB1, and MsbA, conversely, TM2 may be shifted toward the OF conformation typically observed as in Sav1866. The loop connecting TM1 and TM2 has unwound on each side, allowing and/or accompanying the movement of TM2. In the cryo-EM structure with R6G, a consecutive displacement of TM1 shifting toward TM2 is seen, with an unwinding that takes place downward on TM1. The most open structures of Sav1866 and TM287/288 show TM1 and TM2 segments close together and separated from those forming the TM3–6 core. This motion of TM1–2 is concomitant with a wide opening of the cavity and a physical separation of the two TM3–6 cores that behave as rigid bodies. The movement might be granted by the intrinsic flexibility of ABC transporters on their external side, as suggested by molecular dynamics simulations carried out with McjD (*20*) and hinted by the B factors displayed in Fig. 4A.

Aligning the TM1–2 regions of these transporters with respect to their topologically conserved regions encompassing TM3–6 core and NBD allows visualizing the various conformations adopted by TM1–2, suggesting a hand fan motion (Fig. 4B and shown and detailed in Fig. 5F). We therefore explored the level of accessibility of TM1–2 of BmrA E504A in detergent solution by HDX-MS experiments (Fig. 4, C and D). We first observed that the trapping of the OF conformation by adding ATP-$Mg^{2+}$ to the mutant increases the accessibility of the TM1–2 region (Fig. 4C). Several transmembrane peptides display a significantly higher deuterium uptake when adopting the OF conformation, notably those localized in the

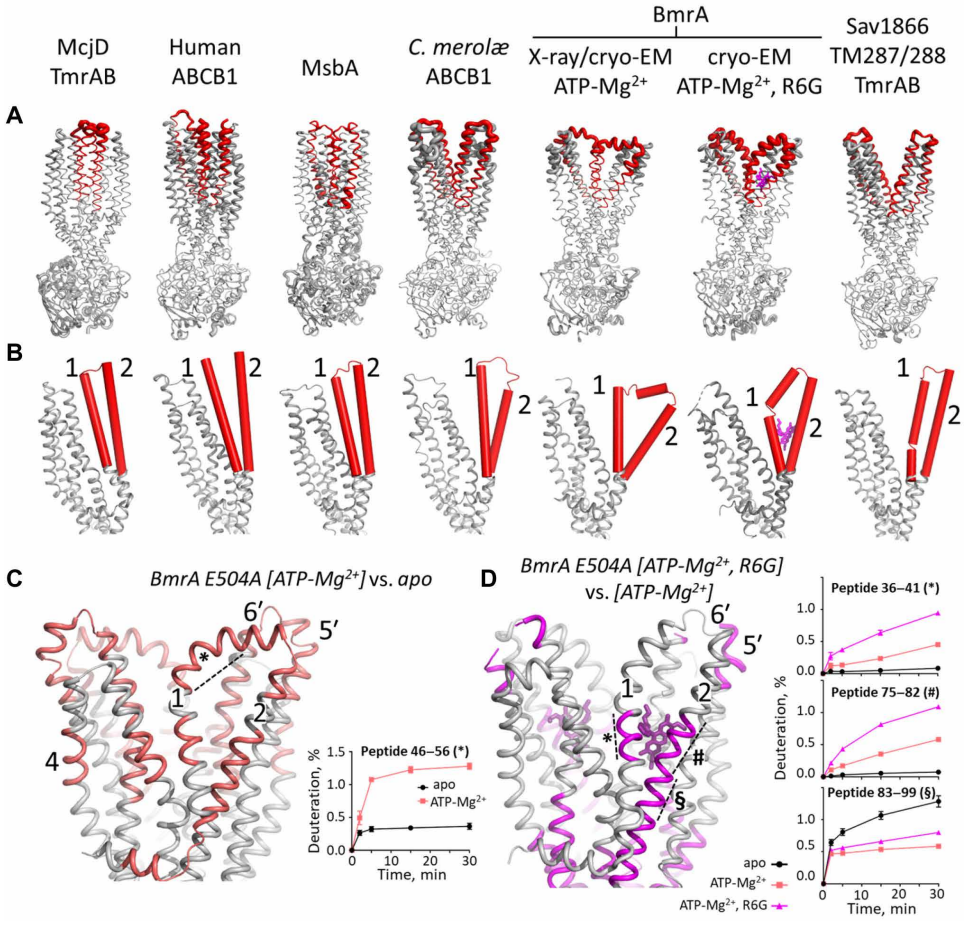


**Fig. 4. Conformations and mobilities of TM1–2 in OF BmrA and other type IV ABC transporters.** (**A**) Views (PDB codes) of McjD (**4pl0**, 5ofr), TmrAB (left: **6rai**, 6rak; right: 6rah-6raj), human (**6c0v**) and *C. merolæ* ABCB1 (**6a6m**), MsbA (**5ttp**), BmrA [this study, with ATP-$Mg^{2+}$ (x-ray: 6r72; cryo-EM: **7ow8**) and with ATP-$Mg^{2+}$and R6G cryo-EM: **7bg4**), Sav1866 (**2hyd**), and TM287/288 (**6qv0**, 6qv1, 6qv2), superimposed from TM3 to TM6 and displayed from left to right from the most occluded to the widest open conformation. For clarity, only structures with bold PDB codes are displayed. Cartoon thickness is proportional to B factor. TM1–2 is colored in red. (**B**) Close-up view of TM1–6 of each monomer (and of the N-terminal half of ABCB1) with the TM1–2 segment in red cylinders. (**C** and **D**) HDX-MS experiments of BmrA E504A in DDM-cholate identifying the TM regions with increased deuterium accessibility in the OF state. (C) displays the ATP-$Mg^{2+}$-bound state as compared to the apo state. (D) compares the ATP-$Mg^{2+}$–bound state with and without R6G. Pictures display the accessible regions after 30-min exchange, colored in salmon ($P < 0.01$) and magenta ($P < 0.001$). Time-dependent deuteration plots of the indicated peptides are shown.

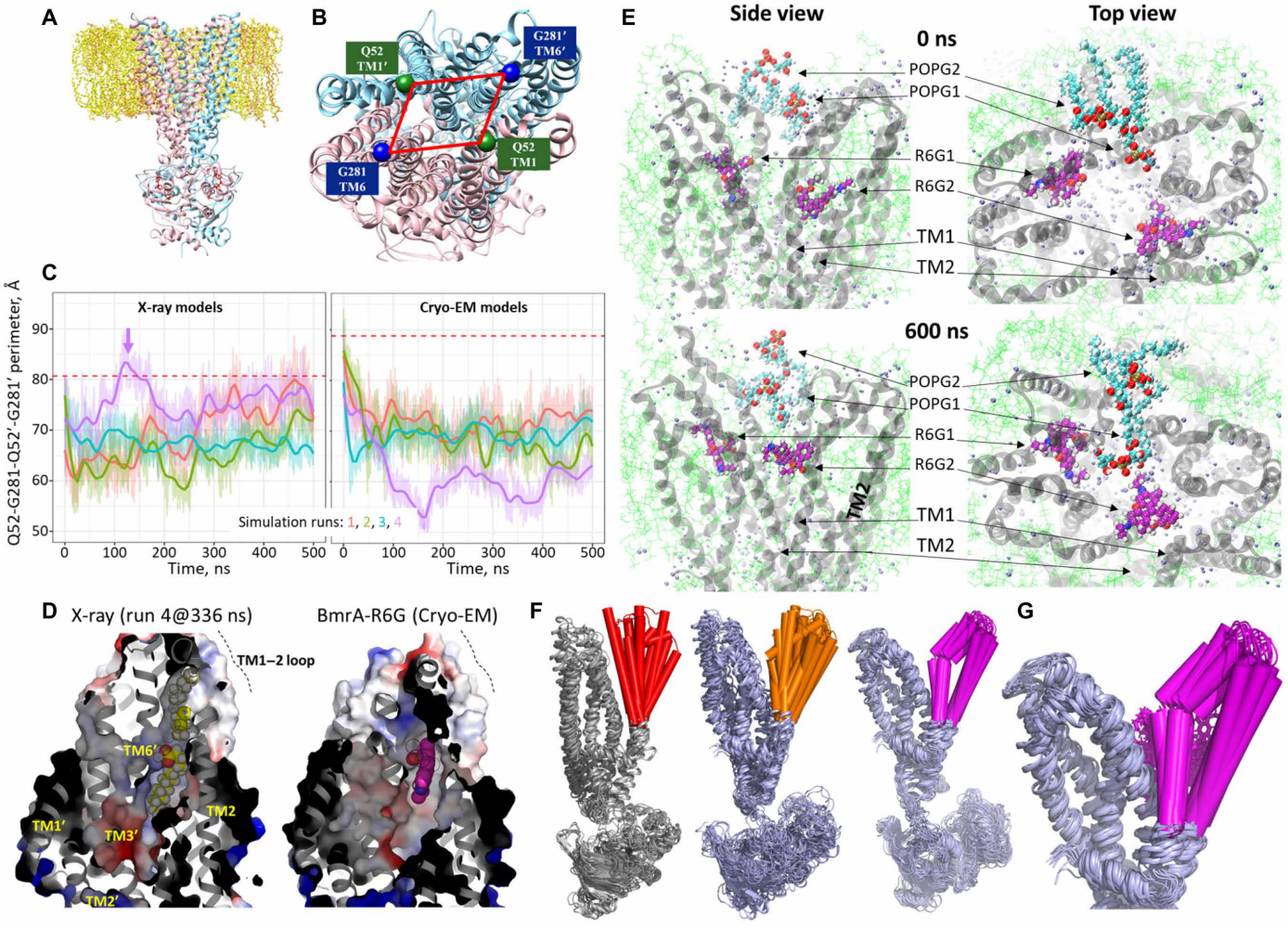


**Fig. 5. Dynamics of the BmrA TMD region.** (**A**) Starting model of BmrA in a lipid bilayer. Chains A and B are colored in pink and cyan, ATP in red, and lipids in yellow. (**B**) Close-up view showing residues chosen for measuring the perimeter of the cavity. (**C**) Time evolution of the cavity perimeter for each simulation. Red dashed lines indicate the initial values of the distances. The arrow indicates the time at which a POPG molecule inserts through TM1–2 in the fourth simulation. (**D**) Electrostatic maps of the BmrA, either from simulation 4 from the x-ray structure taken at 336 ns with the POPG binding to the substrate-binding pocket (left) and from the cryo-EM structure with R6G (right). (**E**) Snapshots of the molecular dynamics of BmrA E504A [ATP-$Mg^{2+}$, R6G] at 0 and 600 ns. Additional snapshots at 300 and 900 ns are displayed in fig. S19A. POPG molecules coming into the cavity are in cyan. (**F**) Superimposition of the structures displayed in Fig. 3A with TM1–2 in red and comparison with the poses got by molecular dynamic simulations carried out without (orange) and with (magenta) R6G (R6G molecules have been omitted for clarity. (**G**) Close-up view of the poses with R6G.

TM1–2 region such as the peptides 46 to 56 (asterisk in Fig. 4C). Such trend is also observed in nanodiscs and comparable to the WT BmrA stabilized by Vi trapping (fig. S14). Note that as compared to the detergent environment, in nanodiscs, a smaller number of transmembrane peptides show an increased deuteration, but they still mostly localize to TM1, TM2, and TM6. We then observed that the addition of R6G to BmrA E504A in complex with ATP-$Mg^{2+}$ significantly increases the accessibility to deuterium of the main chain of transmembrane parts surrounding the R6G-binding region, notably peptides 36 to 41 and 75 to 82 in TM1 and TM2, respectively, translating a structural rearrangement consistent with a widener opening of TM1–2 in the presence of R6G (Fig. 4D). Together, these results are consistent with the mechanical plasticity of TM1–2 inferred from the x-ray and cryo-EM structures of BmrA, which may be a key feature of MDR pumps allowing the release of substrates varying in size and shape.

## Molecular dynamics simulations of x-ray and cryo-EM structures of BmrA

To get a dynamic view of the substrate-exit site of BmrA, we performed two series of all-atom molecular dynamics simulations of BmrA in complex with ATP-$Mg^{2+}$ reconstituted in a lipid bilayer (Fig. 5A), either without or with R6G.

First, we investigated dynamics of BmrA in the absence of R6G. We carried out four simulations of 500 ns on each x-ray and cryo-EM (+R6G from which we removed it) structures under identical conditions using different starting velocities. We estimated the size of the substrate-exit cavity by measuring the variation with time of the perimeter formed by the Cα of the two residues Q52 in TM1 and G281 in TM6 of each monomer (Fig. 5, B and C). As shown, the initial perimeter of the cryo-EM structure, up to 90 Å, was larger than that of the x-ray one, up to 80 Å. Considering the simulation settings and the limited resolution of the structures, we expected to

observe only changes driven by strong forces. All the models undergo a closure (Fig. 5C and fig. S15), reaching a common perimeter of ~70 Å. BmrA shifts toward the most occluded states, as the one observed in MsbA and ABCB1 in Fig. 4 (A and B). This closure is rapid, generally occurring within the initial 100 ns, as also proposed for the extracellular gate of TmrAB (*13*). It contrasts with the stabilized wider open conformation of the x-ray and cryo-EM experiments, possibly because of the DDM-cholate mixture in which BmrA is maintained in these experiments contrarily to the simulations. This fast closure is followed by large-scale structural fluctuations (fig. S16). Of note, a closure was also obtained in simulations with longer equilibration steps. An unexpected result came from the fourth simulation generated from the x-ray structure, which, by contrast to the others, rapidly opens during the first 100 ns its substrate-exit cavity up to ~83 Å (magenta trace in Fig. 5C, left). This movement enlarges enough the lateral opening between TM1 and TM2 to allow a POPG [2-oleoyl-1-palmitoyl-sn-glycero-3-phospho-rac-(1-glycerol)] molecule to penetrate through it and move to the substrate-binding cavity (Fig. 5D, left) in one R6G-binding site (Fig. 5D, right). One aliphatic chain of the lipid lays in the hydrophobic pocket, while its polar head is oriented toward the center of the cavity, as R6G.

Then, we carried out three simulations starting with the cryo-EM structure with R6G for 1 μs and using the same settings. We parameterized the R6G, starting from the molecule in the cryo-EM structure, and then optimized it in a membrane environment (R6G parameterization files rhodamine6G.itp and forcefieldR6G.itp; fig. S17). By contrast with the dynamics carried out above without R6G, in the present ones, BmrA remains open in the OF conformation, leading to a rather constant Q52-G281-Q52′-G281′ perimeter, which ranges between 95 and 115 Å (fig. S18A). One R6G (R6G2 in run 1) among the six of the three simulations substantially moved within the binding pocket (fig. S18B), going to the center of the cavity in ~300 ns and then coming back to its initial location (Fig. 5E and fig. S18C). The movement of this R6G is accompanied with more contacts with water (fig. S19A) and less with protein (fig. S19B), which is typical of a solvation step preceding the release. However, such release does not occur as, early in the simulations, two lipids invade the pocket above the R6G molecules, forming a cap preventing their release (POPG 1 and 2 in Fig. 5E and fig. S18C). Since it cannot be expelled through the center of the pocket, the R6G2 molecules go back to its original location near TM1–2 in ~400 ns, through which it also cannot be expelled because of the presence of lipids blocking this access (Fig. 5E). A longer simulation time would be necessary to allow a release of the substrate.

Last, we observed that the poses generated by the molecular dynamics of BmrA carried out in absence of R6G nicely reproduces the hand fan motion of TM1–2 introduced above as suggested by the superposition of the various type IV ABC structures displayed in Fig. 4A (Fig. 5F, left versus center). In presence of R6G, this hand fan movement is substantially reduced (Fig. 5F, right), with TM1–2 being stabilized by the substrate (Fig. 5G). Notably, for the half of the transporter where R6G moves away from the binding site, the transporter moves in concert accompanying R6G movement with plastic deformation of the binding site, highlighting adaptation of BmrA to its local substrate presence (fig. S19C).

## DISCUSSION

The BmrA structures presented here unravel new conformations in the landscape of structures of multidrug ABC transporters resolved in OF conformations, and one of them reveals a structure of a type IV MDR ABC transporter with its transported substrate in a substrate-release competent state. The R6G molecules are located at the level of the outer leaflet and are poised to be released from the transporter. Several parameters have contributed to stabilize this ternary complex, among them the positive effect of R6G and ATP-$Mg^{2+}$ on their mutual affinities, together with the amphipathic nature of R6G added of a marked hydrophobicity. The present structures reveal a substrate-release site made of flexible (TM1–2) and rigid (TM3–6) regions. Combined with HDX-MS and molecular dynamics simulations, they provide new information on the mechanism of substrate release from the substrate-binding pocket and suggest how the transporter may reset to an occluded conformation by closing back on itself immediately after substrate release. The flexibility of multidrug ABC transporters has been well established in IF states, sampling different conformations that facilitate recognition of multiple compounds (*35*, *39*, *40*). The current study reveals that such a flexibility is also sampled in OF conformations, presumably with a lower amplitude. We propose that this flexibility is required to adapt the site to various substrates' sizes, essential to secure their release to the extracellular side, and also to reset the transporter back to an occluded state, thereby preventing any trans-inhibition mechanism as reported recently (*41*). Such flexibility is also consistent with the fast dynamics of the extracellular gate of TM287/288 observed in EPR experiments (*42*) and suggests that no additional energy input is needed for substrate release.

A key point arises when comparing the fast closure revealed by the simulations with the stabilized outward states observed in both x-ray and cryo-EM structures. A similar flexibility of the external part of the transmembrane segments is observed in the structures and simulations. In the case of experimental structures, the hydrophobic nature of the substrate-binding cavity, together with the accessibility to water, may favor its filling with amphipathic detergents and stabilize this conformation, as seen previously by molecular dynamic simulations carried out on the OF conformation of Sav1866 in the presence of DDM (*33*). The fact that detergents are poor membrane mimetics and that the structures are those of a biochemically

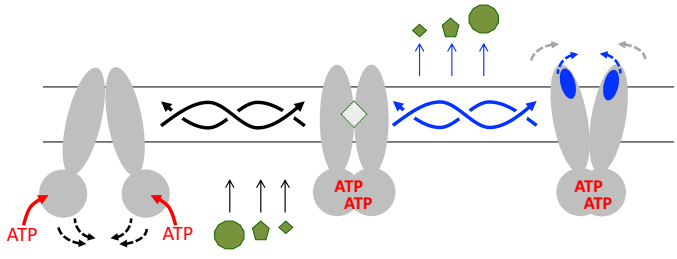


**Fig. 6. Model of mechanism of efflux. Left:** IF conformation of the transporter displaying flexibility at the NBD level, with different degrees of opening of the substrate-binding cavity (black dotted arrows) and allowing for diverse shapes and sizes of substrates. **Middle:** Occluded conformation. **Right:** OF substrate-release conformation. Release occurs via a plastic deformation of the external part of the transmembrane region. Deformation of the apex is adapted to the size or chemical property of the substrates (blue dotted arrows). Hydrophobicity of the substrate-binding pocket triggers the immediate closing of the external part of the transporter, which swings back to the occluded state. ATP hydrolysis occurs, followed by ADP and Pi release resulting in the opening in the IF conformation again, ready for another swing. Twisted arrows exemplify the different routes the transporter can take to reach any conformation, granted by the local deformability of the transmembrane helices.

stabilized version of BmrA (E504A) may have also contributed to stabilize this conformation. Although detergent molecules are too mobile and flexible to be observed at these resolutions, they do however constitute excellent tools to capture such transient states. In the case of simulations in lipid membrane, the hydrophobic pocket is exposed to water, which is extremely unfavorable and leads to a rapid motion of TM1–2 that closes the pocket to shield it from water. Molecular dynamics simulations carried out with McjD have predicted a marked flexibility of the TM1–2 region (*20*), later observed by single-molecule Förster resonance energy transfer (*43*), pointing to a possible role of this region in the release of substrates. This motion appears sufficient per se to reset the transporter back to an occluded conformation. The hydrophobicity of the substrate-binding pocket is so important that in one simulation, a lipid moved into the cavity (Fig. 5, C and D), causing the cavity to remain open. This result fits well with the presence of a detergent molecule in the binding pocket of McjD (*8*) together with the very recent discovery of a lipid inside the structure of the major facilitator superfamily protein LrmP (*44*).

Together, these data emphasize that independent of ATP hydrolysis, hydrophobicity of the substrate-binding pocket alone could promote pocket closure, following a mechanism that may be similar to the hydrophobic collapse described for ion-gated channels (*45*). The intrinsic flexibility of the IF and OF conformations, documented here and well characterized at the level of the NBDs and TMD (*39*, *43*, *46*, *47*), together with this hydrophobic collapse, leads us to favor a mechanism of transport as depicted in Fig. 6. As schematized, the intrinsic flexibility of the exporter in the IF state first allows it to sample multiple conformations adjusting for chemically unrelated substrates. Binding of ATP then leads to the occluded conformation that transiently traps the substrate, and then followed by a plastic deformation of the outward-most part of the exporter (e.g., exemplified with the cartoon thickness proportional to the B factor in Fig. 4A). Again, this plasticity allows the exporter first to accommodate the chemical variability of the substrates and second to release them. The hydrophobic collapse of the substrate-binding pocket then triggers the closing of the transporter, without additional energy input [leading to the hypothesis that ATP hydrolysis occurs after substrate release, as already proposed (*19*, *38*)], allowing the exporter to swing back toward the IF conformation, ready to take on a new molecule. Consequently, in this model, intrinsic plasticity and hydrophobicity collapse alleviate the need for precisely defined conformations at each stage of transport (symbolized by the twisted blue and black arrows in Fig. 6).

## MATERIALS AND METHODS

Materials and Methods are detailed in the Supplementary Materials and Methods. BmrA expression and purification were adapted from methods previously reported (*23*, *48*). Thermostabilization assays were carried out as previously reported (*34*). DDM and cholate quantifications were done as described in (*33*) and (*49*), respectively. The ATPase activity of BmrA was measured as previously described (*34*). The MSP1E3D1 protein was expressed and purified and reconstituted with lipids and BmrA as previously described (*36*). Ligand binding, transport, accumulation, and HDX experiments are detailed in the Supplementary Materials and Methods. BmrA crystallization and additive syntheses, cryo-EM assays, and in silico simulations are detailed in the Supplementary Materials and Methods.

## SUPPLEMENTARY MATERIALS

Supplementary material for this article is available at https://science.org/doi/10.1126/sciadv.abg9215

View/request a protocol for this paper from *Bio-protocol*.

## REFERENCES AND NOTES


1. O. Jardetzky, Simple allosteric model for membrane pumps. *Nature* **211**, 969–970 (1966).
2. K. Linton, C. Higgins, Structure and function of ABC transporters: The ATP switch provides flexible control. *Pflügers Arch.* **453**, 555–567 (2007).
3. K. P. Locher, Mechanistic diversity in ATP-binding cassette (ABC) transporters. *Nat. Struct. Mol. Biol.* **23**, 487–493 (2016).
4. Y. Kim, J. Chen, Molecular structure of human P-glycoprotein in the ATP-bound, outward-facing conformation. *Science* **359**, 915–919 (2018).
5. R. J. Dawson, K. P. Locher, Structure of a bacterial multidrug ABC transporter. *Nature* **443**, 180–185 (2006).
6. A. Ward, C. L. Reyes, J. Yu, C. B. Roth, G. Chang, Flexibility in the ABC transporter MsbA: Alternating access with a twist. *Proc. Natl. Acad. Sci.* **104**, 19005–19010 (2007).
7. A. B. Ward, P. Szewczyk, V. Grimard, C. W. Lee, L. Martinez, R. Doshi, A. Caya, M. Villaluz, E. Pardon, C. Cregger, D. J. Swartz, P. G. Falson, I. L. Urbatsch, C. Govaerts, J. Steyaert, G. Chang, Structures of P-glycoprotein reveal its conformational flexibility and an epitope on the nucleotide-binding domain. *Proc. Natl. Acad. Sci. U.S.A.* **110**, 13386–13391 (2013).
8. H. G. Choudhury, Z. Tong, I. Mathavan, Y. Li, S. Iwata, S. Zirah, S. Rebuffat, H. W. van Veen, K. Beis, Structure of an antibacterial peptide ATP-binding cassette transporter in a novel outward occluded state. *Proc. Natl. Acad. Sci. U.S.A.* **111**, 9145–9150 (2014).
9. A. Blees, D. Januliene, T. Hofmann, N. Koller, C. Schmidt, S. Trowitzsch, A. Moeller, R. Tampé, Structure of the human MHC-I peptide-loading complex. *Nature* **551**, 525–528 (2017).
10. Z. L. Johnson, J. Chen, Structural basis of substrate recognition by the multidrug resistance protein MRP1. *Cell* **168**, 1075–1085.e9 (2017).
11. K. Bountra, G. Hagelueken, H. G. Choudhury, V. Corradi, K. el Omari, A. Wagner, I. Mathavan, S. Zirah, W. Yuan Wahlgren, D. P. Tieleman, O. Schiemann, S. Rebuffat, K. Beis, Structural basis for antibacterial peptide self-immunity by the bacterial ABC transporter McjD. *EMBO J.* **36**, 3062–3079 (2017).
12. H. Göddeke, M. H. Timachi, C. A. J. Hutter, L. Galazzo, M. A. Seeger, M. Karttunen, E. Bordignon, L. V. Schäfer, Atomistic mechanism of large-scale conformational transition in a heterodimeric ABC exporter. *J. Am. Chem. Soc.* **140**, 4543–4551 (2018).
13. S. Hofmann, D. Januliene, A. R. Mehdipour, C. Thomas, E. Stefan, S. Brüchert, B. T. Kuhn, E. R. Geertsma, G. Hummer, R. Tampé, A. Moeller, Conformation space of a heterodimeric ABC exporter under turnover conditions. *Nature* **571**, 580–583 (2019).
14. A. Alam, J. Kowal, E. Broude, I. Roninson, K. P. Locher, Structural insight into substrate and inhibitor discrimination by human P-glycoprotein. *Science* **363**, 753–756 (2019).
15. A. Kodan, T. Yamaguchi, T. Nakatsu, K. Matsuoka, Y. Kimura, K. Ueda, H. Kato, Inward- and outward-facing X-ray crystal structures of homodimeric P-glycoprotein CmABCB1. *Nat. Commun.* **10**, 88 (2019).
16. W. Mi, Y. Li, S. H. Yoon, R. K. Ernst, T. Walz, M. Liao, Structural basis of MsbA-mediated lipopolysaccharide transport. *Nature* **549**, 233–237 (2017).
17. O. Lewinson, C. Orelle, M. A. Seeger, Structures of ABC transporters: Handle with care. *FEBS Lett.* **594**, 3799–3814 (2020).
18. R. L. Juliano, V. Ling, A surface glycoprotein modulating drug permeability in Chinese hamster ovary cell mutants. *Biochim. Biophys. Acta* **455**, 152–162 (1976).
19. Z. L. Johnson, J. Chen, ATP binding enables substrate release from multidrug resistance protein 1. *Cell* **172**, 81–89.e10 (2018).
20. R. X. Gu, V. Corradi, G. Singh, H. G. Choudhury, K. Beis, D. P. Tieleman, Conformational changes of the antibacterial peptide ATP binding cassette transporter McjD revealed by molecular dynamics simulations. *Biochemistry* **54**, 5989–5998 (2015).
21. C. Thomas, R. Tampé, Structural and mechanistic principles of ABC transporters. *Annu. Rev. Biochem.* **89**, 605–636 (2020).
22. C. Thomas, S. G. Aller, K. Beis, E. P. Carpenter, G. Chang, L. Chen, E. Dassa, M. Dean, F. Duong van Hoa, D. Ekiert, R. Ford, R. Gaudet, X. Gong, I. B. Holland, Y. Huang, D. K. Kahne, H. Kato, V. Koronakis, C. M. Koth, Y. Lee, O. Lewinson, R. Lill, E. Martinoia, S. Murakami, H. W. Pinkett, B. Poolman, D. Rosenbaum, B. Sarkadi, L. Schmitt, E. Schneider, Y. Shi, S. L. Shyng, D. J. Slotboom, E. Tajkhorshid, D. P. Tieleman, K. Ueda, A. Váradi, P. C. Wen, N. Yan, P. Zhang, H. Zheng, J. Zimmer, R. Tampé, Structural and functional diversity calls for a new classification of ABC transporters. *FEBS Lett.* **594**, 3767–3775 (2020).
23. E. Steinfels, C. Orelle, J. R. Fantino, O. Dalmas, J. L. Rigaud, F. Denizot, A. di Pietro, J. M. Jault, Characterization of YvcC (BmrA), a multidrug ABC transporter constitutively expressed in *Bacillus subtilis*. *Biochemistry* **43**, 7491–7502 (2004).
24. H. Krügel, A. Licht, G. Biedermann, A. Petzold, J. Lassak, Y. Hupfer, B. Schlott, C. Hertweck, M. Platzer, S. Brantl, H. P. Saluz, Cervimycin C resistance in *Bacillus subtilis* is due to a promoter up-mutation and increased mRNA stability of the constitutive ABC-transporter gene bmrA. *FEMS Microbiol. Lett.* **313**, 155–163 (2010).

25. C. Orelle, O. Dalmas, P. Gros, A. Di Pietro, J. M. Jault, The conserved glutamate residue adjacent to the Walker-B motif is the catalytic base for ATP hydrolysis in the ATP-binding cassette transporter BmrA. *J. Biol. Chem.* **278**, 47002–47008 (2003).
26. H. W. van Veen, K. Venema, H. Bolhuis, I. Oussenko, J. Kok, B. Poolman, A. J. Driessen, W. N. Konings, Multidrug resistance mediated by a bacterial homolog of the human multidrug transporter MDR1. *Proc. Natl. Acad. Sci. U.S.A.* **93**, 10668–10672 (1996).
27. S. Nim, L. G. Lobato, A. Moreno, V. Chaptal, M. K. Rawal, P. Falson, R. Prasad, Atomic modelling and systematic mutagenesis identify residues in multiple drug binding sites that are essential for drug resistance in the major *Candida* transporter Cdr1. *Biochim. Biophys. Acta* **1858**, 2858–2870 (2016).
28. R. Ernst, P. Kueppers, C. M. Klein, T. Schwarzmueller, K. Kuchler, L. Schmitt, A mutation of the H-loop selectively affects rhodamine transport by the yeast multidrug ABC transporter Pdr5. *Proc. Natl. Acad. Sci. U.S.A.* **105**, 5069–5074 (2008).
29. M. Ahmed, L. Lyass, P. N. Markham, S. S. Taylor, N. Vázquez-Laslop, A. A. Neyfakh, Two highly similar multidrug transporters of *Bacillus subtilis* whose expression is differentially regulated. *J. Bacteriol.* **177**, 3904–3910 (1995).
30. H. Sjuts, A. V. Vargiu, S. M. Kwasny, S. T. Nguyen, H. S. Kim, X. Ding, A. R. Ornik, P. Ruggerone, T. L. Bowlin, H. Nikaido, K. M. Pos, T. J. Opperman, Molecular basis for inhibition of AcrB multidrug efflux pump by novel and powerful pyranopyridine derivatives. *Proc. Natl. Acad. Sci. U.S.A.* **113**, 3509–3514 (2016).
31. C. Orelle, F. Gubellini, A. Durand, S. Marco, D. Lévy, P. Gros, A. di Pietro, J. M. Jault, Conformational change induced by ATP binding in the multidrug ATP-binding cassette transporter BmrA. *Biochemistry* **47**, 2404–2412 (2008).
32. S. G. Aller, J. Yu, A. Ward, Y. Weng, S. Chittaboina, R. Zhuo, P. M. Harrell, Y. T. Trinh, Q. Zhang, I. L. Urbatsch, G. Chang, Structure of P-glycoprotein reveals a molecular basis for poly-specific drug binding. *Science* **323**, 1718–1722 (2009).
33. V. Chaptal, F. Delolme, A. Kilburg, S. Magnard, C. Montigny, M. Picard, C. Prier, L. Monticelli, O. Bornert, M. Agez, S. Ravaud, C. Orelle, R. Wagner, A. Jawhari, I. Broutin, E. Pebay-Peyroula, J. M. Jault, H. R. Kaback, M. le Maire, P. Falson, Quantification of detergents complexed with membrane proteins. *Sci. Rep.* **7**, 41751 (2017).
34. K. A. Nguyen, M. Peuchmaur, S. Magnard, R. Haudecoeur, C. Boyère, S. Mounien, I. Benammar, V. Zampieri, S. Igonet, V. Chaptal, A. Jawhari, A. Boumendjel, P. Falson, Glycosyl-substituted dicarboxylates as detergents for the extraction, overstabilization, and crystallization of membrane proteins. *Angew. Chem. Int. Ed. Engl.* **57**, 2948–2952 (2018).
35. D. Lacabanne, C. Orelle, L. Lecoq, B. Kunert, C. Chuilon, T. Wiegand, S. Ravaud, J. M. Jault, B. H. Meier, A. Böckmann, Flexible-to-rigid transition is central for substrate transport in the ABC transporter BmrA from *Bacillus subtilis*. *Commun. Biol.* **2**, 149 (2019).
36. F. J. Alvarez, C. Orelle, A. L. Davidson, Functional reconstitution of an ABC transporter in nanodiscs for use in electron paramagnetic resonance spectroscopy. *J. Am. Chem. Soc.* **132**, 9513–9515 (2010).
37. S. Shukla, V. Rai, D. Banerjee, R. Prasad, Characterization of Cdr1p, a major multidrug efflux protein of *Candida albicans*: Purified protein is amenable to intrinsic fluorescence analysis. *Biochemistry* **45**, 2425–2435 (2006).
38. C. A. J. Hutter, M. H. Timachi, L. M. Hürlimann, I. Zimmermann, P. Egloff, H. Göddeke, S. Kucher, S. Štefanić, M. Karttunen, L. V. Schäfer, E. Bordignon, M. A. Seeger, The extracellular gate shapes the energy profile of an ABC exporter. *Nat. Commun.* **10**, 2260 (2019).
39. S. Mehmood, C. Domene, E. Forest, J. M. Jault, Dynamics of a bacterial multidrug ABC transporter in the inward- and outward-facing conformations. *Proc. Natl. Acad. Sci. U.S.A.* **109**, 10832–10836 (2012).
40. P. C. Wen, B. Verhalen, S. Wilkens, H. S. McHaourab, E. Tajkhorshid, On the origin of large flexibility of P-glycoprotein in the inward-facing state. *J. Biol. Chem.* **288**, 19211–19220 (2013).
41. K. Barth, S. Hank, P. E. Spindler, T. F. Prisner, R. Tampé, B. Joseph, Conformational coupling and trans-inhibition in the human antigen transporter ortholog TmrAB resolved with dipolar EPR spectroscopy. *J. Am. Chem. Soc.* **140**, 4527–4533 (2018).
42. M. H. Timachi, C. A. J. Hutter, M. Hohl, T. Assafa, S. Böhm, A. Mittal, M. A. Seeger, E. Bordignon, Exploring conformational equilibria of a heterodimeric ABC transporter. *eLife* **6**, e20236 (2017).
43. F. Husada, K. Bountra, K. Tassis, M. Boer, M. Romano, S. Rebuffat, K. Beis, T. Cordes, Conformational dynamics of the ABC transporter McjD seen by single-molecule FRET. *EMBO J.* **37**, e100056 (2018).
44. V. Debruycker, A. Hutchin, M. Masureel, E. Ficici, C. Martens, P. Legrand, R. A. Stein, H. S. Mchaourab, J. D. Faraldo-Gómez, H. Remaut, C. Govaerts, An embedded lipid in the multidrug transporter LmrP suggests a mechanism for polyspecificity. *Nat. Struct. Mol. Biol.* **27**, 829–835 (2020).
45. M. O. Jensen, D. W. Borhani, K. Lindorff-Larsen, P. Maragakis, V. Jogini, M. P. Eastwood, R. O. Dror, D. E. Shaw, Principles of conduction and hydrophobic gating in K+ channels. *Proc. Natl. Acad. Sci. U.S.A.* **107**, 5833–5838 (2010).
46. P. P. Borbat, K. Surendhran, M. Bortolus, P. Zou, J. H. Freed, H. S. Mchaourab, Conformational motion of the ABC transporter MsbA induced by ATP hydrolysis. *PLoS Biol.* **5**, e271 (2007).
47. M. Yang, N. Livnat Levanon, B. Acar, B. Aykac Fas, G. Masrati, J. Rose, N. Ben-Tal, T. Haliloglu, Y. Zhao, O. Lewinson, Single-molecule probing of the conformational homogeneity of the ABC transporter BtuCD. *Nat. Chem. Biol.* **14**, 715–722 (2018).
48. B. Wiseman, A. Kilburg, V. Chaptal, G. C. Reyes-Mejia, J. Sarwan, P. Falson, J. M. Jault, Stubborn contaminants: Influence of detergents on the purity of the multidrug ABC transporter BmrA. *PLOS ONE* **9**, e114864 (2014).
49. E. Heftmann, S. T. Ko, R. D. Bennett, Response of steroids to sulfuric acid in thin-layer chromatography. *J. Chromatogr.* **21**, 490–494 (1966).
50. C. M. Hebling, C. R. Morgan, D. W. Stafford, J. W. Jorgenson, K. D. Rand, J. R. Engen, Conformational analysis of membrane proteins in phospholipid bilayer nanodiscs by hydrogen exchange mass spectrometry. *Anal. Chem.* **82**, 5415–5419 (2010).
51. A. M. Lau, J. Claesen, K. Hansen, A. Politis, Deuteros 2.0: Peptide-level significance testing of data from hydrogen deuterium exchange mass spectrometry. *Bioinformatics* **37**, 270–272 (2021).
52. Y. Perez-Riverol, A. Csordas, J. Bai, M. Bernal-Llinares, S. Hewapathirana, D. J. Kundu, A. Inuganti, J. Griss, G. Mayer, M. Eisenacher, E. Pérez, J. Uszkoreit, J. Pfeuffer, T. Sachsenberg, Ş. Yılmaz, S. Tiwary, J. Cox, E. Audain, M. Walzer, A. F. Jarnuczak, T. Ternent, A. Brazma, J. A. Vizcaíno, The PRIDE database and related tools and resources in 2019: Improving support for quantification data. *Nucleic Acids Res.* **47**, D442–D450 (2019).
53. J. Y. Lee, J. G. Yang, D. Zhitnitsky, O. Lewinson, D. C. Rees, Structural basis for heavy metal detoxification by an Atm1-type ABC exporter. *Science* **343**, 1133–1136 (2014).
54. L. Zimmermann, A. Stephens, S. Z. Nam, D. Rau, J. Kübler, M. Lozajic, F. Gabler, J. Söding, A. N. Lupas, V. Alva, A completely reimplemented MPI bioinformatics toolkit with a new HHpred server at its core. *J. Mol. Biol.* **430**, 2237–2243 (2018).
55. M. A. Lomize, I. D. Pogozheva, H. Joo, H. I. Mosberg, A. L. Lomize, OPM database and PPM web server: Resources for positioning of proteins in membranes. *Nucleic Acids Res.* **40**, D370–D376 (2012).
56. J. Lee, X. Cheng, J. M. Swails, M. S. Yeom, P. K. Eastman, J. A. Lemkul, S. Wei, J. Buckner, J. C. Jeong, Y. Qi, S. Jo, V. S. Pande, D. A. Case, C. L. Brooks III, A. D. MacKerell Jr., J. B. Klauda, W. Im, CHARMM-GUI input generator for NAMD, GROMACS, AMBER, OpenMM, and CHARMM/OpenMM simulations using the CHARMM36 additive force field. *J. Chem. Theory Comput.* **12**, 405–413 (2016).
57. B. Hess, C. Kutzner, D. van der Spoel, E. Lindahl, GROMACS 4: Algorithms for highly efficient, load-balanced, and scalable molecular simulation. *J. Chem. Theory Comput.* **4**, 435–447 (2008).
58. U. Essmann, L. Perera, M. L. Berkowitz, T. Darden, H. Lee, L. G. Pedersen, A smooth particle mesh Ewald method. *J. Chem. Phys.* **103**, 8577–8593 (1995).
59. S. Páll, B. Hess, A flexible algorithm for calculating pair interactions on SIMD architectures. *Comput. Phys. Commun.* **184**, 2641–2650 (2013).
60. G. Bussi, D. Donadio, M. Parrinello, Canonical sampling through velocity rescaling. *J. Chem. Phys.* **126**, 014101 (2007).
61. M. Parrinello, A. Rahman, Polymorphic transitions in single crystals: A new molecular dynamics method. *J. Appl. Phys.* **52**, 7182–7190 (1981).
62. K. Vanommeslaeghe, E. Hatcher, C. Acharya, S. Kundu, S. Zhong, J. Shim, E. Darian, O. Guvench, P. Lopes, I. Vorobyov, Mackerell AD Jr, CHARMM general force field: A force field for drug-like molecules compatible with the CHARMM all-atom additive biological force fields. *J. Comput. Chem.* **31**, 671–690 (2010).


**Acknowledgments:** We thank K. Martin Pos for the gift of the CD43(DE3)Δ*AcrB E. coli* strain and H. Krügel for those of *B. subtilis* 168 and 8R. We thank L. Martinez for input in the BrmA purification process in introducing the cholate-DDM mixture. We thank the Synchrotron SOLEIL and ESRF staff, the crystallogenesis platform from SFR Bioscience UMS 3444, and IBCP. We thank C. Von Rhein and P. Legrand for the help in anisotropic data processing. Cryo-EM sample screening, optimization, and data collection were performed at the Cryo-EM Swedish National Facility in Stockholm, Sweden, funded by the Knut and Alice Wallenberg, Family Erling Persson and Kempe Foundations, SciLifeLab, Stockholm University, and the Umeå University. B.W. thanks M. Carroni and J. Conrad from the Swedish National Facility in Stockholm for the technical assistance in cryo-EM data collection. We thank the staff of beamline CM01 at ESRF for rapid access data collection through the proposal MX2344. We also thank the reviewers for the constructive inputs that contributed to substantial improvement of the manuscript. Last but not least, P.F. thanks G. Deleage for the constant support along these years, particularly at the beginning of the study. **Funding:** This work was supported by the Centre National de la Recherche Scientifique (CNRS), l'Institut National de la Santé et de la Recherche Médicale (INSERM), the Lyon University, the Grenoble-Alpes University, the French Research Agency (ANR), and Auvergne-Rhône-Alpes region (ARC1) as follows: ARC1-CLAMP grant no. 13 009802 01 to A.B., V.C., and P.F.; ANR-CLAMP-13-BSV5-0001-01 to P.F., A.B., V.C., and A.K.; ANR-NMX-14-CE09-0024-03 to P.F., J.-M.J., and V.C.; ANR-CAVEOTANK-17-CE11-0015-03 to P.F. and V.C.; ANR-CLAMP2-18-CE11-0002-01 to P.F., A.B., M.H., and V.C.; ANR-17-EURE-0003 (CBH-EUR-GS) to A.B. and M.P.; and ANR-19-CE11-0023-01 to C.O., V.C., J.-M.J., and P.F. Molecular dynamics calculations were carried out at CINES, GENCI grant no.

A0040710138 to L.M. Financial support was also provided to M.H. by the Swedish Research Council (2017-04018) and the Knut and Alice Wallenberg Foundation (2017.0275). A.K. and V.Z. PhDs were funded by ARC1 and EDISS school, respectively. K.-A.N.'s PhD was funded by EDCSV of Grenoble-Alpes University. B.W.'s postdoc was funded by the ANR projects CAVEOTANK and CLAMP2. J.E. was funded by the ANR CLAMP2. The HDX-MS experiments were supported by the French Ministry of Research (Investissements d'Avenir Program, Proteomics French Infrastructure, ANR-10-INBS-08), the Fonds Européens de Développement Régional Toulouse Métropole, and the Région Midi-Pyrénées. The cryo-EM data for resolving the apo-BmrA structure were collected using the platforms of the Grenoble Instruct–ERIC Center (ISBG; UMS 3518 CNRS-CEA-UGA-EMBL) within the Grenoble Partnership for Structural Biology (PSB), supported by FRISBI (ANR-10-INBS-05-02) and GRAL, financed within the University Grenoble Alpes graduate school (Ecoles Universitaires de Recherche) CBH-EUR-GS (ANR-17-EURE-0003). The electron microscope facility is supported by the Auvergne-Rhône-Alpes Region, the Fondation pour la Recherche Médicale (FRM), the fonds FEDER, and the GIS–Infrastructures en Biologie Santé et Agronomie (IBiSA). **Author contributions:** V.C., V.Z., A.K., A.G., and S.M. purified BmrA and carried out the crystallogenesis experiments. M.H. granted access to cryo-EM equipment, and B.W. carried out the cryo-EM experiments for the R6G-BmrA complex. G.S., A.G., and V.C. carried out the cryo-EM experiments with the apo form using the Grenoble Instruct–ERIC platform. V.Z., V.C., and P.F. carried out the detergent quantifications. V.C., V.Z., A.G., and B.W. resolved the structures. C.O. and V.Z. prepared the E504A mutant. V.Z., C.O., S.M., and A.G. carried out the ATPase assays. A.B. and P.F. conceived the crystallization additives, and K.-A.N., M.P., and A.B. synthesized them. S.M. and P.F. carried out the thermostability assays. J.Mart., J.E., and L.M. carried out the dynamic simulations. W.J., M.D.C., and J.Marc. performed the HDX-MS experiments supervised by J.-M.J. and C.O. J.-M.J. and C.O. contributed to the analysis of the results. V.Z., A.G., M.D.C., S.M., C.O., J.-M.J., V.C., and P.F. carried out the biochemical experiments. P.F. managed the overall project. The manuscript was written through contributions of all the authors who gave their approval to its final version. **Competing interests:** P.F., J.D., A.B., M.P., K.-A.N., and S.M. are inventors on a patent related to this work filed by the Centre National de la Recherche Scientifique, the Claude Bernard–Lyon 1 University and the Grenoble–Alpes University (nos. FR3063730B1, US20210130385A1, and WO2018162806A1), filed 9 March 2017, published 13 September 2018 (WO2018162806A1), 6 May 2021 (US20210130385A1), and 17 September 2021 (FR3063730B1). Crystallization additive requests can be addressed for research only to pierre.falson@univ-lyon1.fr or to ahcene.boumendjel@univ-grenoble-alpes.fr. The other authors declare that they have no competing interests. **Data and materials availability:** Crystal and cryo-EM structures of BmrA-E504A [ATP-$Mg^{2+}$] have been deposited in the Protein Data Bank and Electron Microscopy Data Bank with the following codes: x-ray: PDB 6r72; cryo-EM (with R6G unresolved): PDB 6r81, EMDB 4749 (C2 symmetry); cryo-EM (with R6G resolved): PDB 7BG4, EMDB 12170 (no symmetry); cryo-EM (without R6G): PDB 7ow8, EMDB-13095. The HDX-MS data have been deposited to the ProteomeXchange Consortium via the PRIDE partner repository with the dataset identifier PXD027447. Simulations are available online on Zenodo, with the DOI 10.5281/zenodo.5543740. All data needed to evaluate the conclusions in the paper are present in the paper and/or the Supplementary Materials.

Submitted 4 February 2021
Accepted 30 November 2021
Published 26 January 2022
10.1126/sciadv.abg9215

ScienceAdvances

# Substrate-bound and substrate-free outward-facing structures of a multidrug ABC exporter

Vincent ChaptalVeronica ZampieriBenjamin WisemanCédric OrelleJuliette MartinKim-Anh NguyenAlexia GobetMargot Di CesareSandrine MagnardWaqas JavedJad EidArnaud KilburgMarine PeuchmaurJulien MarcouxLuca MonticelliMartin HogbomGuy SchoehnJean-Michel JaultAhcène BoumendjelPierre Falson

*Sci. Adv.*, 8 (4), eabg9215. • DOI: 10.1126/sciadv.abg9215

Science Advances
AAAS

# Supplementary Materials for

## Substrate-bound and substrate-free outward-facing structures of a multidrug ABC exporter

Vincent Chaptal, Veronica Zampieri, Benjamin Wiseman, Cédric Orelle, Juliette Martin, Kim-Anh Nguyen, Alexia Gobet, Margot Di Cesare, Sandrine Magnard, Waqas Javed, Jad Eid, Arnaud Kilburg, Marine Peuchmaur, Julien Marcoux, Luca Monticelli, Martin Hogbom, Guy Schoehn, Jean-Michel Jault, Ahcène Boumendjel, Pierre Falson*

*Corresponding author. Email: pierre.falson@univ-lyon1.fr

Published 26 January 2022, *Sci. Adv.* **8**, eabg9215 (2022)
DOI: 10.1126/sciadv.abg9215

**The PDF file includes:**



**Other Supplementary Material for this manuscript includes the following:**

Data S1 and S2
Rhodamine6G.itp
ForcefieldR6G.itp

**Supplementary Text**

**Materials and Methods**

Chemistry

Solvents and reagents were purchased from commercial sources and used without further purification. Reactions were monitored by thin layer chromatography (TLC) using commercial silica gel 60 $F_{254}$ coated plates from Macherey-Nagel. Visualization was carried out under UV light at 254 and 365 nm and/or heating with a solution of sulfuric acid/acetic acid/water or phosphomolybdic acid/cerium sulfate/sulfuric acid/water or ninhydrin stain or iodine vapor. Purifications were performed by gravity column chromatography using silica gel 60 (230-400 mesh) from Macherey-Nagel or by automatic Reveleris® X2 flash chromatography system. MPs were measured using a Büchi B540 melting point apparatus and are uncorrected. Electrospray ionization (ESI) mass spectra were obtained on an Esquire 3000 Plus Bruker Daltonis instrument with a nanospray inlet. Accurate mass measurements (HRMS) were carried out on an ESI/QTOF with the Waters Xevo G2-S QTof device. Analyses were performed by the analytical service of *Institut de Chimie Moléculaire de Grenoble* (ICMG). Spectra were recorded in deuterated solvents on Bruker Avance spectrometers at 400 or 500 MHz for $^{1}H$ and 100 or 125 MHz for $^{13}C$ NMR, respectively. Chemical shifts ($\delta$) are reported in parts per million (ppm) relative to the solvent [$^{1}H$: $\delta$(acetone-$d_6$) = 2.05 ppm, $\delta$(DMSO-$d_6$) = 2.50 ppm, $\delta(CD_3OD)$ = 3.31 ppm, $\delta(CDCl_3)$ = 7.26 ppm; $^{13}C$: $\delta$(DMSO-$d_6$) = 39.5 ppm, $\delta(CD_3OD)$ = 49.0 ppm, $\delta(CDCl_3)$ = 77.2 ppm, $\delta$(acetone-$d_6$) = 206.3 ppm]. Multiplicity of signals is reported as followed: s (singlet), bs (broad singlet), d (doublet), t (triplet), q (quartet), qt (quintet), st (septet), dd (doublet of doublet), ddd (doublet of doublet of doublet), dt (doublet of triplet) ddt (doublet of doublet of triplet) and m (multiplet). Coupling constants (J) are given in Hertz (Hz). When direct signal assignments were difficult, additional spectra were acquired (J-mod, COSY, HMQC or HMBC).

**Synthesis of amphiphiles 3a-3e as crystallization additives**

Crystallization additives were obtained according to the synthetic scheme shown below.

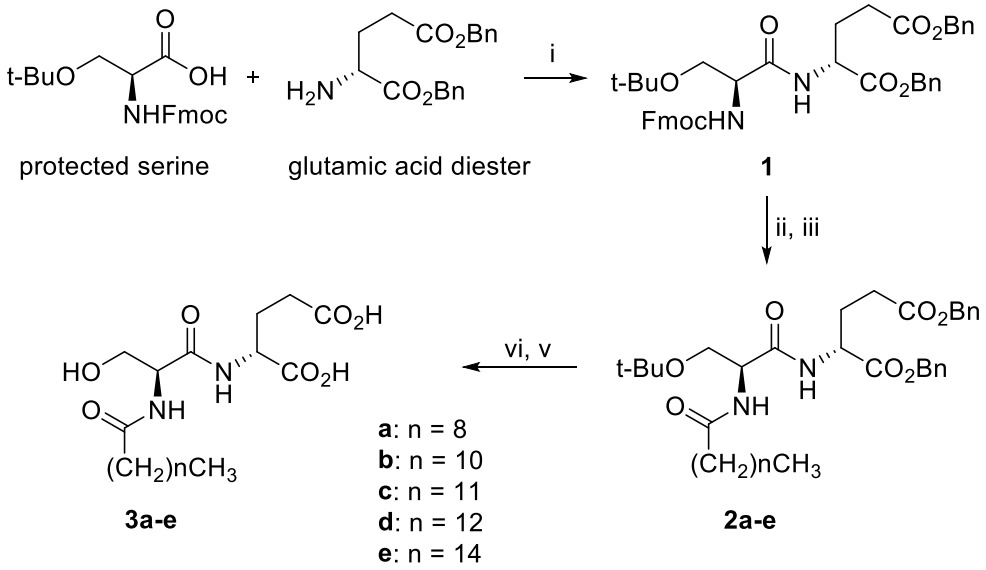

Reagents and Conditions. **i**. TBTU, DIEA, DMF; **ii**. $Et_2NH$, $CH_2Cl_2$; **iii**. R-CO-Cl, DMAP, pyridine, $CH_2Cl_2$; **vi**. $H_2$, Pd/C, MeOH; **v**. TFA, $CH_2Cl_2$.

Synthesis of compound 1. Dibenzyl (R)-2-{(S)-2-[((9H-fluoren-9-yl)methoxycarbonyl) amino]-3-tert-butoxypropanamido} glutarate.

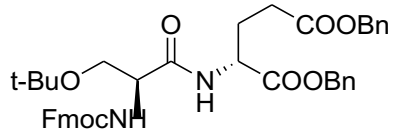


To a solution of protected serine (3.5 g, 9.12 mmol) in anhydrous DMF (15 mL/mmol) were successively added the glutamic acid diester (9.0 g, 18.24 mmol, 2 equiv.), TBTU (1.2 equiv.) and DIPEA (5 equiv.). The mixture was stirred at room temperature (rt) under $N_2$ atmosphere for 3 h. After completion of the reaction, water (15 mL/mmol) was added. The compound precipitated and was crystallized in a mixture of $CH_2Cl_2/Et_2O$ to provide compound 1 (5.14 g, 81% yield).

R*f* = 0.50 (cyclohexane/EtOAc 7:3); MP = 126-128 °C; $^1$H NMR (400 MHz, $CDCl_3$) δ ppm 1.19 (s, 9H), 1.99-2.11 (m, 1H), 2.22-2.35 (m, 1H), 2.32-2.55 (m, 2H), 3.41 (dd, *J* = 8.3, 8.3 Hz, 1H), 3.75-3.87 (m, 1H), 4.23 (t, *J* = 7.1 Hz, 1H), 4.24-4.33 (m, 1H), 4.40 (d, *J* = 6.8 Hz, 2H), 4.68-4.76 (m, 1H), 5.09 (s, 2H), 5.17 (s, 2H), 5.78 (bs, 1H), 7.21-7.46 (m, 15H), 7.61 (d, *J* = 7.0 Hz, 2H), 7.76 (d, *J* = 7.5 Hz, 2H). $^{13}$C NMR (100 MHz, $CDCl_3$) δ ppm 27.4 (3x$CH_3$), 27.5 ($CH_2$), 30.0 ($CH_2$), 47.1 (CH), 51.8 (CH), 54.6 (CH), 61.7 ($CH_2$), 66.5 ($CH_2$), 67.2 ($CH_2$), 67.4 ($CH_2$), 74.3 (C), 120.0 (2xCH), 125.1 (2xCH), 127.1 (2xCH), 127.7 (2xCH), 128.2-128.7 (10xCH), 135.1 (C), 135.7 (C), 141.3 (2xC), 143.7 (2xC), 156.1 (C), 170.1 (C), 171.2 (C), 172.3 (C); MS (ESI+) m/z (%) 426 (100), 570 (3), 715 (1) $[M+Na]^+$; HRMS (ESI+) m/z, calculated for $C_{41}H_{45}N_2O_8$ 693.3176, found 693.3156.

**Synthesis of compounds 2.**

*Fmoc deprotection.* To a solution of compound **1** (1 equiv.) in anhydrous dichloromethane (20 mL/mmol) was added diethylamine (20 equiv.). The reaction mixture was stirred at rt under $N_2$ atmosphere overnight. The volatiles were removed under reduced pressure. To eliminate the residual diethylamine, the crude product was diluted in dichloromethane, washed with a saturated sodium bicarbonate ($NaHCO_3$) solution, dried over $MgSO_4$, filtered and concentrated under reduced pressure and used for the next steps without further purification.

*Amide formation.* The crude compound obtained in the previous step (1 equiv.) was dissolved in anhydrous dichloromethane (30 mL/mmol). The acyl chloride derivative was added (2 equiv.), together with dimethylaminopyridine (DMAP) (0.5 equiv.) and pyridine (34 equiv.). The reaction mixture was stirred at rt under $N_2$ atmosphere overnight. The reaction mixture was acidified to pH = 3 with an aqueous solution of HCl 10% and extracted with dichloromethane. The combined organic layers were washed with brine and dried over $MgSO_4$, filtered, and concentrated under reduced pressure. The crude product was purified by silica gel column chromatography.

**Compound 2a**. Dibenzyl (R)-2-[(S)-3-tert-butoxy-2-(decanamido)propanamido]glutarate

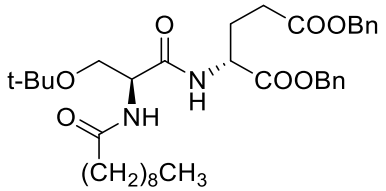


The crude product was prepared starting from **1** (500 mg, 0.70 mmol) and commercially available decanoyl chloride (267 mg, 1.40 mmol). After purification by column chromatography on silica gel (cyclohexane/EtOAc 8:2 to 7:3), the pure product **2a** (195 mg, 0.31 mmol, 45%) was obtained as a white solid.

R*f* = 0.18 (cyclohexane/EtOAc 7:3). MP = 82-85 °C; $^{1}$H NMR (400 MHz, $CDCl_3$) $\delta$ ppm 0.87 (t, *J* = 6.9 Hz, 3H), 1.16 (s, 9H), 1.19-1.35 (m, 12H), 1.55-1.66 (m, 2H), 1.96-2.07 (m, 1H), 2.21 (t, *J* = 7.8 Hz, 2H), 2.21-2.30 (m, 1H), 2.32-2.50 (m, 2H), 3.31 (dd, *J* = 8.7, 8.7 Hz, 1H), 3.80 (dd, *J* = 8.7, 4.2 Hz, 1H), 4.44-4.50 (m, 1H), 4.65-4.72 (m, 1H), 5.08 (s, 2H), 5.15 (s, 2H), 6.40 (d, *J* = 6.4 Hz, 1H, NH), 7.27-7.36 (m, 11H) ; $^{13}$C NMR (100 MHz, $CDCl_3$) $\delta$ ppm 14.1 ($CH_3$), 22.7 (2x$CH_2$), 25.6 ($CH_2$), 27.4 (3x$CH_3$), 27.5 ($CH_2$), 29.3-29.44 (4x$CH_2$), 30.0 ($CH_2$), 31.9 ($CH_2$), 36.6 ($CH_2$), 51.8 (CH), 53.0 (CH), 61.3 ($CH_2$), 66.5 ($CH_2$), 67.3 ($CH_2$), 74.3 (C), 128.3-128.7 (10xCH), 135.2 (C), 135.8 (C), 170.4 (C), 171.2 (C), 172.3 (C), 173.3 (C) ; MS (ESI+) *m/z* (%) 626 (30) $[M+H]^+$, 648 (100) $[M+Na]^+$; HRMS (ESI+) *m/z*, calculated for $C_{36}H_{53}N_2O_7$ 625.3853, found 625.3846.

**Compound 2b**. Dibenzyl (R)-2-[(S)-3-tert-butoxy-2-(dodecanamido)propanamido]glutarate

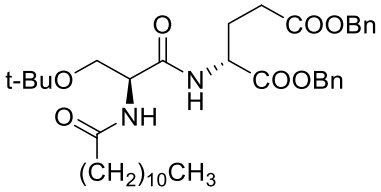


The crude product was prepared starting from **1** (400mg, 0.58 mmol) and commercially available dodecanoyl chloride (252 mg, 1.15 mmol). After purification by column chromatography on silica gel (cyclohexane/EtOAc 8:2 to 7:3), the pure product **2b** (182 mg, 0.28 mmol, 48%) was obtained as a white solid.

R*f* = 0.12 (cyclohexane/EtOAc 8:2) ; MP = 67-69 °C ; $^{1}$H NMR (400 MHz, $CDCl_3$) $\delta$ ppm 0.88 (t, *J* = 6.9 Hz, 3H), 1.17 (s, 9H), 1.19-1.35 (m, 16H), 1.56-1.67 (m, 2H), 1.96-2.08 (m, 1H), 2.21 (t, *J* = 7.6 Hz, 2H), 2.21-2.32 (m, 1H), 2.32-2.50 (m, 2H), 3.30 (dd, *J* = 8.7, 8.7 Hz, 1H), 3,81 (dd, *J* = 8.7, 4.2 Hz, 1H), 4.42-4.49 (m, 1H), 4.64-4.72 (m, 1H), 5.09 (s, 2H), 5.16 (s, 2H), 6.38 (d, *J* = 6.3 Hz, 1H, NH), 7.23-7.39 (m, 11H); $^{13}$C NMR (100 MHz, $CDCl_3$) $\delta$ ppm 14.2 ($CH_3$), 22.8 ($CH_2$), 25.6 ($CH_2$), 27.5 (3x$CH_3$), 27.6 ($CH_2$), 29.4-29.7 (6x$CH_2$), 30.0 ($CH_2$), 32.0 ($CH_2$), 36.7 ($CH_2$), 51.9 (CH), 53.1 (CH), 61.4 ($CH_2$), 66.6 ($CH_2$), 67.5 ($CH_2$), 74.4 (C), 128.4-128.8 (10xCH), 135.2 (C), 135.9 (C), 170.4 (C), 171.3 (C), 172.4 (C), 173.4 (C) ; MS (ESI+) *m/z* (%) 131 (30), 199 (40), 654 (50) $[M+H]^+$, 677 (100), 699 (20); HRMS (ESI+) *m/z*, calculated for $C_{38}H_{57}N_2O_7$ 653.4166, found 653.4158.

**Compound 2c**. Dibenzyl (R)-2-[(S)-3-tert-butoxy-2-(tridecanamido)propanamido]glutarate.

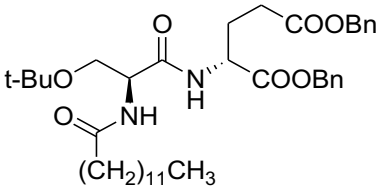


The crude product was prepared starting from **1** (500 mg, 0.70 mmol) and commercially available tridecanoyl chloride (326 mg, 1.40 mmol). After purification by column chromatography on silica gel (cyclohexane/EtOAc 8:2 to 7:3), the pure product **2c** (233 mg, 0.35 mmol, 50%) was obtained as a white solid.

R*f* = 0.24 (cyclohexane/EtOAc 7:3); MP = 68-71 °C ; $^{1}$H NMR (400 MHz, $CDCl_3$) $\delta$ ppm 0.88 (t, *J* = 6.9 Hz, 3H), 1.17 (s, 9H), 1.20-1.36 (m, 18H), 1.55-1.67 (m, 2H), 1.96-2.08 (m, 1H), 2.21 (t, *J* = 7.6 Hz, 2H), 2.21-2.32 (m, 1H), 2.32-2.50 (m, 2H), 3.31 (dd, *J* = 8.7, 8.7 Hz, 1H), 3.80 (dd, *J* = 8.7, 4.2 Hz, 1H), 4.44-4.50 (m, 1H), 4.63-4.73 (m, 1H), 5.08 (s, 2H), 5.15 (s, 2H), 6.41 (d, *J* = 6.4 Hz, 1H, NH), 7.25-7.37 (m, 11H); $^{13}$C NMR (100 MHz, $CDCl_3$) $\delta$ ppm 14.1 ($CH_3$), 22.7 ($CH_2$), 25.5 ($CH_2$), 27.4 (3x$CH_3$), 27.5 ($CH_2$), 29.3-29.7 (7x$CH_2$), 29.9 ($CH_2$), 31.9 ($CH_2$), 36.5 ($CH_2$), 51.8 (CH), 53.0 (CH), 61.3 ($CH_2$), 66.5 ($CH_2$), 67.3 ($CH_2$), 74.2 (C), 128.3-128.6 (10xCH), 135.2 (C), 135.8 (C), 170.4 (C), 171.2 (C), 172.3 (C), 173.3 (C) ; MS (ESI+) *m/z* (%) 668 (20) $[M+H]^+$, 690 (100) $[M+Na]^+$; HRMS (ESI+) *m/z*, calculated for $C_{39}H_{59}N_2O_7$ 667.4322, found 667.4334.

**Compound 2d**. Dibenzyl (R)-2-[(S)-3-t-butoxy-2-(tetradecanamido)propanamido] glutarate.

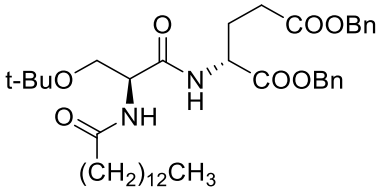


The crude product was prepared starting from **1** (400 mg, 0.58 mmol) and commercially available tetradecanoyl chloride (285 mg, 1.15 mmol). After purification by column chromatography on silica gel (cyclohexane/EtOAc 8:2 to 7:3), the pure product **2d** (187 mg, 0.27 mmol, 48%) was obtained as a white solid.

R*f* = 0.07 (cyclohexane/EtOAc 8:2); MP = 71-73 °C ; $^{1}$H NMR (400 MHz, $CDCl_3$) $\delta$ ppm 0.88 (t, *J* = 6.9 Hz, 3H), 1.17 (s, 9H), 1.20-1.36 (m, 20H), 1.56-1.67 (m, 2H), 1.97-2.08 (m, 1H), 2.21 (t, *J* = 7.6 Hz, 2H), 2.23-2.50 (m, 3H), 3.29 (dd, *J* = 8.7, 8.7 Hz, 1H), 3.80 (dd, *J* = 8.7, 4.2 Hz, 1H), 4.41-4.49 (m, 1H), 4.63-4.72 (m, 1H), 5.09 (s, 2H), 5.14 (d, *J* = 12.3 Hz, 1H), 5.18 (d, *J* = 12.3 Hz, 1H), 7.25-7.39 (m, 11H); $^{13}$C NMR (100 MHz, $CDCl_3$) $\delta$ ppm 14.2 ($CH_3$), 22.8 ($CH_2$), 25.6 ($CH_2$), 27.5 (3x$CH_3$), 27.6 ($CH_2$), 29.4-29.8 (8x$CH_2$), 30.0 ($CH_2$), 32.0 ($CH_2$), 36.7 ($CH_2$), 51.9 (CH), 53.1 (CH), 61.4 ($CH_2$), 66.6 ($CH_2$), 67.5 ($CH_2$), 74.4 (C), 128.4-128.8 (10xCH), 135.2 (C), 135.8 (C), 170.5 (C), 171.3 (C), 172.4 (C), 173.4 (C) ; MS (ESI+) *m/z* (%) 131 (65), 199 (100), 682 (60) $[M+H]^+$ ; HRMS (ESI+) *m/z* calculated for $C_{40}H_{61}N_2O_7$ 681,4479, found 681,4447.

**Compound 2e**. Dibenzyl (R)-2-[(S)-3-tert-butoxy-2-(hexadecanamido)propanamido]glutarate

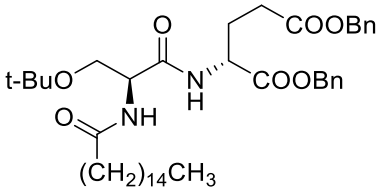


The crude product was prepared starting from **1** (300 mg, 0.43 mmol) and commercially available hexadecanoyl chloride (238 mg, 0.87 mmol). After purification by column chromatography on silica gel (cyclohexane/EtOAc 8:2), the pure product **2e** (93 mg, 0.13 mmol, 30%) was obtained as a white solid.

R*f* = 0.11 (8:2 cyclohexane/EtOAc). MP = 69-71 °C. $^{1}$H NMR (400 MHz, $CDCl_3$) $\delta$ ppm 0.88 (t, *J* = 6.8 Hz, 3H), 1.17 (s, 9H), 1.20-1.37 (m, 24H), 1.55-1.68 (m, 2H), 1.97-2.09 (m, 1H), 2.21 (t, *J* = 7.6 Hz, 2H), 2.16-2.51 (m, 3H), 3.29 (dd, *J* = 8.7, 8.7 Hz, 1H), 3.81 (dd, *J* = 8.7, 4.2 Hz, 1H), 4.39-4.49 (m, 1H), 4.62-4.72 (m, 1H), 5.09 (s, 2H), 5.14 (d, *J* = 12.3 Hz, 1H), 5.18 (d, *J* = 12.3 Hz, 1H), 6.36 (d, *J* = 6.3 Hz, 1H), 7.20-7.40 (m, 11H); $^{13}$C NMR (100 MHz, $CDCl_3$) $\delta$ ppm 14.3 ($CH_3$), 22.8 ($CH_2$), 25.7 ($CH_2$), 27.5 (3x$CH_3$), 27.6 ($CH_2$), 29.4-29.8 (10x$CH_2$), 30.1 ($CH_2$), 32.1 ($CH_2$), 36.7 ($CH_2$), 51.9 (CH), 53.1 (CH), 61.4 ($CH_2$), 66.6 (CH2), 67.5 (CH2), 74.5 (C), 128.4-128.8 (10xCH), 135.2 (C), 135.9 (C), 170.5 (C), 171.3 (C), 172.4 (C), 173.5 (C); MS (ESI+) *m/z* (%) 199 (15), 710 (100) $[M+H]^+$, 732 (15) $[M+Na]^+$; HRMS (ESI+) *m/z* calculated for $C_{42}H_{65}N_2O_7$ 709.4792 $[M+H]^+$, found 709.4805.

**Synthesis of compounds 3**

*Catalytic hydrogenolysis.* To a degassed solution of a compound **2** (1 equiv.) in MeOH (100 mL/mmol) was added Pd/C 10% (200 mg/mmol). The reaction mixture was stirred at rt under $H_2$ atmosphere from 4 h to overnight. After filtration over Celite® to remove the catalyst, the solvent was evaporated under reduced pressure. The residue was used directly for the next step or washed with cyclohexane and/or dichloromethane to obtain the product which was used as is for the *t*-Bu deprotection step.

*t-Butyl deprotection.* To a solution of *t*-Bu-intermediate, obtained in the previous step (1 equiv.) in anhydrous dichloromethane (12 mL/mmol) at 0 °C was added dropwise TFA (4 mL/mmol). The reaction mixture was stirred at rt under $N_2$ atmosphere overnight. The

volatiles were removed under reduced pressure and the residue was dissolved in DCM. A solution of NaOH (2 M) was added to pH = 11-12. The aqueous layer was washed with EtOAc before being acidified to pH 1-2 with concentrated HCl and extracted 3 times with EtOAc. The combined organic layers were dried over $MgSO_4$, filtered and concentrated under reduced pressure. The residue was washed with DCM to obtain the pure product.

**Compound 3a**. (R)-2-[(S)-2-(Decanamido)-3-hydroxypropanamido]glutaric acid.

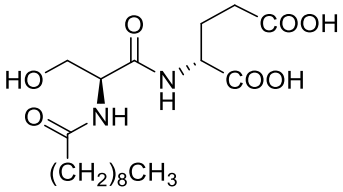


The pure product (white solid, 182 mg, 0.47 mmol, 94%) was prepared starting from **2a** (310 mg, 0.50 mmol). MP = 53-57 °C; $^1$H NMR (400 MHz, $CD_3OD$) $\delta$ ppm 0.89 (t, $J$ = 6.8 Hz, 3H), 1.22-1.38 (m, 12H), 1.56-1.69 (m, 2H), 1.90-2.03 (m, 1H), 2.14-2.26 (m, 1H), 2.29 (t, $J$ = 7.3 Hz, 2H), 2.36-2.43 (m, 2H), 3.73-3.84 (m, 2H), 4.42-4.52 (m, 2H); $^{13}$C NMR (100 MHz, $CD_3OD$) $\delta$ ppm 14.4 ($CH_3$), 23.7 ($CH_2$), 26.8 ($CH_2$), 27.9 ($CH_2$), 30.3-30.5 (4x$CH_2$), 31.1 ($CH_2$), 33.0 ($CH_2$), 36.9 ($CH_2$), 53.3 (CH), 56.6 (CH), 63.1 ($CH_2$), 172.5 (C), 174.9 (C), 176.5 (C), 176.5 (C); MS (ESI-) *m/z* (%) 387 (100) $[M-H]^-$, 404 (20); HRMS (ESI-) *m/z* calculated for $C_{18}H_{31}N_2O_7$ 387.2131 $[M-H]^-$, found 387.2140.

**Compound 3b.** (R)-2-[(S)-2-(Dodecanamido)-3-hydroxypropanamido]glutaric acid.

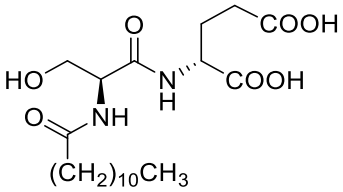


The pure product (white solid, 1.68 g, 4.04 mmol, 70%) was prepared starting from **2b** (3.76 g, 5.80 mmol). MP = 100-102 °C; $^1$H NMR (400 MHz, $CD_3OD$) $\delta$ ppm 0.90 (t, $J$ = 6.9 Hz, 3H), 1.22-1.38 (m, 16H), 1.57-1.67 (m, 2H), 1.91-2.01 (m, 1H), 2.15-2.26 (m, 1H), 2.29 (t, $J$ = 7.2 Hz, 2H), 2.37-2.44 (m, 2H), 3.72-3.81 (m, 2H), 4.43-4.51 (m, 2H); $^{13}$C NMR (100 MHz, $CD_3OD$) $\delta$ ppm 14.4 ($CH_3$), 23.7 ($CH_2$), 26.8 ($CH_2$), 27.9 ($CH_2$), 30.4-30.7 (6x$CH_2$), 31.0 ($CH_2$), 33.1 ($CH_2$), 36.9 ($CH_2$), 53.1 (CH), 56.6 (CH), 63.1 ($CH_2$), 172.6 (C), 174.6 (C), 176.4 (C), 176.5 (C); MS (ESI-) *m/z* (%) 157 (40), 199 (30), 387 (80), 415 (100) $[M-H]^-$; HRMS (ESI-) *m/z* calculated for $C_{20}H_{35}N_2O_7$ 415.2444 $[M-H]^-$, found 415.2447.

**Compound 3c**. (R)-2-[(S)-2-(Tridecanamido)-3-hydroxypropanamido]glutaric acid.

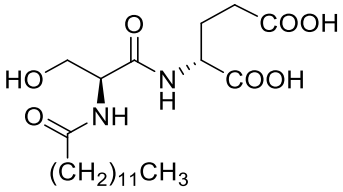


The pure product (white solid, 115 mg, 0.27 mmol, 89%) was prepared starting from **2c** (198 mg, 0.30 mmol). MP = 58-63 °C; $^1$H NMR (400 MHz, $CD_3OD$) $\delta$ ppm 0.89 (t, $J$ = 6.9 Hz, 3H), 1.21-1.41 (m, 18H), 1.54- 1.68 (m, 2H), 1.90-2.04 (m, 1H), 2.14-2.27 (m, 1H), 2.29 (t, $J$ = 7.4 Hz, 2H), 2.36-2.48 (m, 2H), 3.71-3.83 (m, 2H), 4.43-4.53 (m, 2H); $^{13}$C NMR (100 MHz, $CD_3OD$) $\delta$ ppm 14.4 ($CH_3$), 23.7 ($CH_2$), 26.8 ($CH_2$), 27.8 ($CH_2$), 30.3-30.9 (7x$CH_2$), 31.0 ($CH_2$), 33.0 ($CH_2$), 36.9 ($CH_2$), 53.1 (CH), 56.6 (CH), 63.1 ($CH_2$), 172.6 (C), 174.6 (C), 176.4 (C), 176.5 (C); MS (ESI-) *m/z* (%) 429 (100) $[M-H]^-$, 446 (30); HRMS (ESI-) *m/z* calculated for $C_{21}H_{37}N_2O_7$ 429.2601 $[M-H]^-$, found 429.2599.

**Compound 3d**. (R)-2-[(S)-2-(Tetradecanamido)-3-hydroxypropanamido]glutaric acid

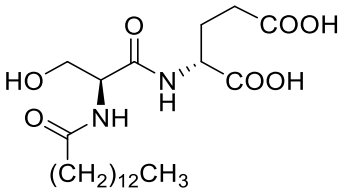


The pure product (white solid, 57 mg, 0.13 mmol, quantitative) was prepared starting from **2d** (87 mg, 0.13 mmol). MP = 109-112 °C; $^{1}$H NMR (400 MHz, $CD_3OD$) $\delta$ ppm 0.90 (t, $J$ = 6.8 Hz, 3H), 1.19-1.39 (m, 20H), 1.57- 1.67 (m, 2H), 1.90-2.02 (m, 1H), 2.16-2.26 (m, 1H), 2.29 (t, $J$ = 7.4 Hz, 2H), 2.36-2.45 (m, 2H), 3.71-3.84 (m, 2H), 4.43-4.52 (m, 2H); $^{13}$C NMR (100 MHz, $CD_3OD$) $\delta$ ppm 14.4 ($CH_3$), 23.7 ($CH_2$), 26.8 ($CH_2$), 27.9 ($CH_2$), 30.4-30.9 (8x$CH_2$), 31.1 ($CH_2$), 33.0 ($CH_2$), 36.9 ($CH_2$), 53.3 (CH), 56.6 (CH), 63.1 ($CH_2$), 172.6 (C), 174.9 (C), 176.5 (C), 176.5 (C); MS (ESI-) *m/z* (%) 443 (100) $[M-H]^-$; HRMS (ESI-) *m/z* calculated for $C_{22}H_{39}N_2O_7$ 443.2757 $[M-H]^-$, found 443.2754.

**Compound 3e.** (R)-2-[(S)-2-(Hexadecanamido)-3-hydroxypropanamido]glutaric acid

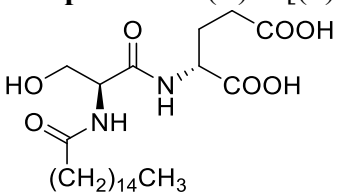


The pure product (white solid, 36 mg, 0.08 mmol, 65%) was prepared starting from **2e** (83 mg, 0.18 mmol). MP = 111-113 °C; $^{1}$H NMR (400 MHz, $CD_3OD$) $\delta$ ppm 0.90 (t, $J$ = 6.8 Hz, 3H), 1.19-1.37 (m, 24H), 1.55-1.68 (m, 2H), 1.90-2.03 (m, 1H), 2.15-2.26 (m, 1H), 2.29 (t, $J$ = 7.4 Hz, 2H), 2.36-2.44 (m, 2H), 3.72-3.82 (m, 2H), 4.43-4.52 (m, 2H); $^{13}$C NMR (100 MHz, $CD_3OD$) $\delta$ ppm 14.4 ($CH_3$), 23.7 ($CH_2$), 26.8 ($CH_2$), 27.9 ($CH_2$), 30.4-30.8 (10x$CH_2$), 31.1 ($CH_2$), 33.1 ($CH_2$), 36.9 ($CH_2$), 53.2 (CH), 56.6 (CH), 63.1 ($CH_2$), 172.6 (C), 174.7 (C), 176.5 (C), 176.5 (C); MS (ESI) *m/z* (%) 471 (100) $[M-H]^-$; HRMS (ESI-) *m/z* calculated for $C_{24}H_{43}N_2O_7$ 471.3070, found 471.3057.

Biochemistry

**Products**. Products were from Sigma except when indicated. SOC medium was from Invitrogen, LB broth medium from Roth, ampicillin and Triton X100 from Euromedex, anti-protease tablets from Roche, $Ni^{2+}$-NTA resin from Generon, DDM and DM from Anatrace, Amicon Ultra-15 devices from Millipore and Superdex 200 10/300 GL from GE.

**BmrA expression**. BmrA expression was adapted from methods previously reported (*23, 48*). The E504A mutant was generated and fused to a 6-histidine *N*-terminal Nickel-affinity tag in the pET15(+) plasmid and overexpressed in the CD43(DE3)Δ*acrB E. coli* strain, a gift of Pr. Klaas Martinus Pos. A freshly transformed colony was incubated in 3 mL LB containing 50 µg/mL for 7-8 h at 37 °C. Thirty microliters of this preculture were added to 1 L LB containing 50 µg/mL of ampicillin, which was then incubated at 22 °C until reaching 0.6 $OD_{600}$. BmrA expression was induced by 0.7 mM IPTG followed by a 5-6 h incubation at 22 °C. Bacteria were collected at 5000 xg for 15 min., 4 °C and then suspended in 10 mL 50 mM Tris-HCl pH 8.0, 5 mM $MgCl_2$ and 1 mM PMSF. Bacteria were lysed by 3 passages at 18,000 psi through a microfluidizer 100 (Microfluidics IDEX Corp). The solution was centrifuged 30 min. at 15,000 xg at 4 °C. The membrane fraction was pelleted by centrifugation for 1 h at 180,000 xg at 4°C, suspended in 50 mM Tris-HCl pH 8.0, 1 mM PMSF and 1 mM EDTA and centrifuged again. The final pellet was suspended in 20 mM Tris-HCl pH 8.0, 0.3 M sucrose and 1 mM EDTA, frozen in liquid nitrogen and stored at -80 °C.

**BmrA purification**. Membranes were solubilized at 5 mg/mL in 20 mM Tris-HCl pH 8.0, 100 mM NaCl, 15% glycerol (v/v), anti-protease tablets, 0.1 mM TCEP and 4.5% (w/v)

Triton X100, under gentle agitation for 90 min. and then centrifuged 40 min. at 100,000 xg. The supernatant was loaded onto a $Ni^{2+}$-NTA equilibrated in 20 mM Tris-HCl pH 8.0, 100 mM NaCl, 15% (v/v) glycerol, anti-protease tablets, 4.5% Triton X100 and 20 mM imidazole. The resin was washed with 20 mM Hepes-HCl pH 8.0, 100 mM NaCl, 20 mM imidazole, 1.3 mM DDM and 1 mM sodium cholate. The protein was eluted by adding 200 mM imidazole to the same buffer. BmrA fractions were pooled and diluted ten times in the Hepes buffer (same composition as above) without imidazole and loaded again on the same resin for another step of affinity chromatography. The pool of BmrA fractions was concentrated on 50 kDa cutoff Amicon Ultra-15 devices, with the centrifuge speed set at 1000 xg for 10-15 min, and then loaded onto Superdex 200 10/300 using as mobile phase 20 mM Hepes-HCl pH 7.5, 100 mM NaCl, 0.7 mM DDM and 0.7 mM sodium cholate (DDM:cholate molar ratio of 1:1). The same step was also carried out at DDM-cholate ratio of 3:1 or 1:3. Cholate was systematically removed from the Superdex resin by a washing with 1M NaOH. The elution peak was then pooled and stored at 4 °C before use. BmrA was particularly stable when not concentrated as previously reported (*34*).

**Thermostabilisation assays** were carried out as previously reported (*34*). Membranes of BmrA diluted at 2 g proteins/L were solubilized with 10 mM DDM, with or without 1 mM of compounds **3a**-**3e** in a final volume of 2 mL, for 2 h at 4 °C. Solutions were clarified by centrifugation at 100,000 xg for 1 h at 4 °C and supernatants were aliquoted (50 µL) and individually submitted 30 min to a temperature of 25 to 90 °C using a PCR thermal cycler (PeqSTAR 2x gradient; Peqlab). Samples were then centrifuged 40 min at 20,000 xg and supernatants were analyzed by SDS-PAGE and Western-blot using anti-His antibody. The relative intensity of BmrA at each temperature was quantified on Western blot using Image Lab software 4.1 (Bio-Rad). Each condition was performed twice or thrice. Intensity was plotted as a function of the temperature and normalized. Data were fitted with equation 5 (see data fit section).

**Detergents quantification.** DDM bound to BmrA was quantified by mass spectrometry as described (*33*). Cholate was quantified as previously reported (*49*). Modelling of the detergent belt radius was done following the same protocol and using the DeltBelt server (www.deltbelt.ibcp.fr).

**ATPase activity.** The ATPase activity of BmrA was measured as previously described (*34*). The protein in solution in 20 mM Hepes-HCl pH 7.5, 100 mM NaCl, 0.7 mM DDM and 0.7 mM cholate was diluted in the ATPase activity assay buffer containing either 1 mM DDM or a mixture of 0.7 mM DDM and 0.7 mM cholate, and the ATPase activity recorded.

**Membrane-scaffold protein (MSP) production and purification**. The MSP1E3D1 protein was expressed in BL21 *E. coli* (p1E3D1 plasmid, Addgene) as previously described (*36*). Bacteria were suspended in 50 mL of 40 mM Tris-HCl pH 7.4, 100 mM NaCl, 1 % (w/v) Triton X100, 0.5 mM EDTA, 1 mM PMSF. Two microliters of Benzonase (24 U/mL, Merck) were added and the bacteria were lysed by 2 passages at 18,000 psi through a microfluidizer 100 (Microfluidics IDEX Corp) and then centrifuged during 30 min. at 30,000 xg, 4°C. The supernatant was loaded onto a 0.5-mL $Ni^{2+}$-NTA column (GE Healthcare) resin pre-equilibrated with 5 resin-volumes of 40 mM Tris-HCl pH 7.4, 100 mM NaCl, 1 % (w/v) Triton X100, 0.5 mM EDTA and 1 mM PMSF. The resin was then washed with 10 resin-volume with 3 different buffers: wash buffer 1 composed of 40 mM Tris-HCl pH 8.0, 300 mM NaCl and 1% (w/v) Triton X100; wash buffer 2 composed of 40 mM Tris-HCl pH 8.0, 300 mM NaCl, 50 mM sodium cholate and 20 mM Imidazole; wash buffer 3 composed of 40 mM Tris-HCl pH 8.0, 300 mM NaCl, 50 mM Imidazole. MSP1E3D1 was eluted with 15 mL of 40 mM Tris-HCl pH 8.0, 300 mM NaCl and 500 mM Imidazole. The factions of the elution pic were pooled and the TEV (2 mg/mL) was added to remove the His tag, at a ratio of 1 mg TEV for 40 mg MSP1E3D1. The mixture was then dialyzed (cutoff 12-14 kDa), a first time

against 300 mL 40 mM Tris-HCl, pH 7.4, 100 mM NaCl and 0.5 mM EDTA for 3 hours and then against 700 mL of the same buffer, overnight at 4 °C. After dialysis 20 mM imidazole was added and the solution loaded on a 0.5 mL $Ni^{2+}$-NTA column equilibrated with 20 mM Tris-HCl pH 7.4 and 100 mM NaCl. The flow-through containing MSP1E3D1 was collected. The uncleaved fraction was eluted with 40 mM Tris-HCl pH 8.0, 300 mM NaCl and 500 mM Imidazole, dialyzed two times as above and finally concentrated spinning at 5,000 xg with a 100 kDa cutoff Amicon Ultra-15. The concentrated samples were frozen in liquid nitrogen and stored at -80 °C.

**BmrA reconstitution into nanodiscs**.

BmrA was reconstituted into nanodiscs as previously described (*36*) with the following modifications. Six hundred micrograms of purified BmrA E504A in 200 µL of Hepes-HCl pH 7.5, 100 mM NaCl, 0.035% DDM and 0.03% sodium cholate were mixed with 1.4 mg of *E. coli* lipids (Avanti Polar) in 56 µL of 99 mM cholate, 20 mM Hepes-HCl pH 7.5, 100 mM NaCl for 10 min at room temperature. The mix was then added of 665 µg MSP1E3D1 in 35 µL of 40 mM Tris-HCl, pH 7.4, 100 mM NaCl and 0.5 mM EDTA. The volume was completed to 1 mL with Hepes-HCl pH 7.5, 100 mM NaCl and incubated 1 h at room temperature. The final molar ratio of BmrA/MSP/lipids was 1/5/400 in 20 mM Hepes-HCl pH 7.5, 100 mM NaCl. SM-2 biobeads (170 mg/100 µg BmrA, Biorad) were then added to the mixture, placed 3 h under gentle agitation at room temperature. Empty nanodiscs were removed from the BmrA-nanodiscs by $Ni^{2+}$-NTA chromatography. The resin was equilibrated with 20 mM Hepes-HCl pH 7.5, 100 mM NaCl, then loaded with the sample, washed with 20 mM Hepes-HCl pH 7.5, 100 mM NaCl, 20 mM imidazole. The BmrA-nanodiscs complex was then eluted with 20 mM Hepes-HCl pH 7.5, 100 mM NaCl, 200 mM imidazole. Imidazole was then removed from the solution by passing through a HiTrap desalting column equilibrated with 20 mM Hepes-HCl pH 7.5, 100 mM NaCl.

**Ligand binding on BmrA in detergents**.

R6G, ATP-$Mg^{2+}$ and cholate binding was carried out by incubating 15 min on ice 0.5 µM BmrA, WT or E504A mutant prepared in DDM or DDM-cholate with or without 5 mM ATP-$Mg^{2+}$ in 20 mM Hepes-HCl pH 7.5, 100 mM NaCl, including 0.7 mM DDM and/or 0.7 mM cholate depending on the experiments. The binding of R6G was probed by intrinsic fluorescence recorded on a SAFAS Xenius spectrophotofluorimeter set up at a constant photo multiplicator voltage of 570 V. Tryptophan residues or *N*-acetyl tryptophan amide (NATA) used as negative control were excited at 280 nm, and their fluorescence emission spectra were recorded between 310 and 380 nm, with a 5-nm bandwidth for excitation and emission. Experiments were done in a quartz cuvette in a final volume of 200 µL, in which increasing amounts of R6G were added. Resulting emission curves were integrated and deduced from the same experiments carried out with NATA, used at the same concentration than that of BmrA tryptophan residues. Data were plotted as a function of R6G concentration. Binding of ATP-$Mg^{2+}$ was carried out in the same way, pre-incubating BmrA E504A with or without 100 µM R6G for 15 min on ice.

**Ligand binding to BmrA-nanodiscs complexes and empty nanodiscs**. R6G, DDM and DM binding assays were carried out as above. Assays with empty nanodiscs (without BmrA) were carried out at the same nanodiscs concentration as that of BmrA-nanodiscs, complexes. This allowed to correct the fluorescence quenching due to the interaction between empty nanodiscs alone and ligands. Two cuvettes of NATA were also used: one for BmrA-nanodiscs complex and the other one for the empty nanodiscs. Data were analyzed in the same way as above.

**Doxorubicin transport by BmrA** was recorded as previously described (*23*). Ten micromolar of doxorubicin and 2 mM ATP were added to 100 µg *E. coli* inverted membrane vesicles containing overexpressed BmrA. Transport was initiated upon addition of 2 mM $MgCl_2$ and monitored at 25 °C in 1-mL quartz cuvettes recording the fluorescence on a

Photon Technology International fluorimeter at 590 nm with a bandwidth of 4 nm upon excitation at 480 nm with a bandwidth of 2 nm. Transport was initiated by adding 2 mM ATP-$Mg^{2+}$.

**R6G accumulation in *Bacillus subtilis* strains.** R6G accumulation assay was performed in *B. subtilis* strain 168 (WT) and 8R (overexpressing *BmrA* (*24*) kindly provided by Pr. Hans Krügel). Strains were grown overnight in LB medium at 37 °C with agitation, and then diluted to 0.05 $OD_{600nm}$ with fresh medium. Once the culture reached 0.5 $OD_{600nm}$, they were incubated with 5 µM R6G for 30 min more. Then 2 mL of each culture (~ 1 $OD_{600nm}$) was centrifuged at 15,000 xg for 10 min at 4 °C. The pellets were washed with 1 mL LB medium and centrifuged. The pellets were suspended in 500 µL of 50 mM Tris-HCl pH 8.0, 150 mM NaCl, 1 mg/mL lysozyme and incubated for 1 h at 37 °C with agitation. The cells were then incubated with 0.5% SDS for 15 min more. R6G fluorescence was recorded with a SAFAS Xenius spectrophotofluorimeter in a black 96 well-plate using 200 µL of cell lysates setting excitation to 526 nm and recording fluorescence between 541 and 650 nm.

**Data fit**. Data were fitted using Microsoft Excel (365), SigmaPlot (v12.5) and GraphPad (v8) using/setting up the following equations:

**Equation 1 (Intrinsic fluorescence quenching, ligand binding, one site saturation)**: $f = F_{max}*abs([L])/(K_D+abs([L]))$, $F_{max}$ = maximal intrinsic fluorescence without ligand, [L] = ligand concentration, $K_D$, ligand dissociation constant.

**Equation 2 (allosteric intrinsic fluorescence increase):**
$f = F_{min}+(F_{max}-F_{min})/(1+([L]/K_D)^{-h})$, $F_{min}$ = minimal intrinsic fluorescence without ligand, $F_{max}$ = maximal intrinsic fluorescence with ligand, [L] = ligand concentration, $K_D$, ligand dissociation constant, $h$ = Hill number.

**Equation 3 (Sigmoidal, 3 parameters)**: $f = F_{max}/(1+\exp(-([L]-[L]_{50})/b))$, $F_{max}$ = maximal intrinsic fluorescence, [L] = ligand concentration, µM, $[L]_{50}$ = ligand concentration at half-maximal intrinsic fluorescence, µM.

**Equation 4 (Intrinsic fluorescence quenching, ligand binding, two sites saturation)**: $f = F_{max1}*abs([L])/(K_{D1}+abs([L])) + F_{max2}*abs([L])/(K_{D2} + abs([L]))$, $F_{max1}$, $F_{max2}$ = maximal intrinsic fluorescence without ligand, [L] = ligand concentration, $K_{D1}$, $K_{D2}$, ligand dissociation constants.

**HDX experiments**

HDX-MS experiments were performed using a Synapt G2-Si mass spectrometer coupled to a NanoAcquity UPLC M-Class System with HDX Technology (Waters™).

*BmrA reconstituted in nanodiscs labelling*. All the reactions were carried out manually. Labeling was initiated by diluting 5 µL of 15 µM BmrA WT or 37 µM BmrA E504A in nanodiscs, in 95 µL $D_2O$ labeling buffer (5 mM Hepes pD 8.0, 50 mM NaCl). For the ATP/Vi- and ATP-incubated conditions, the labeling buffer additionally contained 10 mM ATP, 10 mM $MgCl_2$, 1 mM Vi and 10 mM ATP, 10 mM $MgCl_2$, respectively. For the drug-bound condition, the labeling buffer additionally contained 10 mM ATP, 10 mM $MgCl_2$, and 100 µM R6G. Prior to labeling, the samples were incubated with the respective ligands for 15 min at 20 °C. Samples were labeled for 2, 5, 15 and 30 min at 20 °C. Subsequently, the reactions were quenched by adding 22 µL of ice-cold quenching buffer (0.5 M glycine, 8 M guanidine-HCl pH 2.2, 0.035% DDM and 0.03% sodium cholate) to 100 µL of labelled sample, in ice bath. After 1 min, the 122-µL quenched sample was added into a microtube containing 200 µg of activated zirconium magnetic beads (MagReSyn Zr-IMAC from Resyn Biosciences, USA), to remove the phospholipids (*50*). After 1 min magnetic beads were removed, and the supernatant was injected immediately into a 100-µL loop.

*BmrA in detergent mixture labelling*. The reactions were carried out by a Twin HTS PAL dispensing and labelling robot (LEAP Technologies, Carborro, NC, USA) coupled to a Synapt

G2Si mass spectrometer (Waters, Manchester, UK). Labeling was initiated by diluting 5.2 µL, of typically 37 µM protein, in 98.8 µL $D_2O$ labeling buffer (5 mM Hepes pD 8, 50 mM NaCl, 0.035% DDM, 0.03% sodium cholate). For the drug-bound condition, the labeling buffer additionally contained 10 mM ATP, 10 mM $MgCl_2$, and 100 µM R6G. Prior labeling the samples were incubated with the respective ligands for 15 min at 20 °C. Samples were labeled for 2, 5, 15 and 30 min at 20 °C. Subsequently the samples were quenched by adding 22 µL of ice-cold quenching buffer (0.5 M glycine, 8 M guanidine-HCl pH 2.2) to 100 µL of labelled sample, in ice bath. After 1 min, 105-µL quenched sample were injected immediately into a 100-µL loop.

*UPLC-MS*. Labelled proteins were then subjected to on-line digestion at 15 °C using a pepsin column (Waters Enzymate™ BEH Pepsin Column 300 Å, 5 µm, 2.1 x 30 mm). The resulting peptides were trapped and desalted for 3 min on a C4 pre-column (Waters ACQUITY UPLC Protein BEH C4 VanGuard pre-column 300 Å, 1.7 µm, 2.1 x 5 mm, 10K - 500K) before separating them with a C4 column (Waters ACQUITY UPLC Protein BEH C4 Column 300 Å, 1.7 µm, 1 x 100 mm) using 0.2% formic acid and a 5-40 % linear acetonitrile gradient in 15 min and then 4 alternative cycles of 5% and 95% until 25 min. The valve position was adjusted to divert the sample after 14 min of each run from C4 column to waste, to avoid a contamination of the mass spectrometer with detergent. Two or three full kinetics were run for each condition, one after the other, to get either duplicate or triplicates of each deuteration timepoint. Blanks (equilibration buffer: 5 mM Hepes pH 8.0, 50 mM NaCl) were injected after each sample injection and pepsin column washed during each run with pepsin wash (1.5 M guanidine-HCl, 4% acetonitrile, 0.8% formic acid pH 2.5) to minimize the carryover. Electrospray ionization mass spectra were acquired in positive mode in the m/z range of 50−2000 and with a scan time of 0.3 s. For the identification of non-deuterated peptides, data was collected in MSE mode and the resulting peptides were identified using PLGS™ software (ProteinLynx Global SERVER 3.0.2 from Waters™). Peptides were then filtered in DynamX 3.0 software (Waters™), with the following parameters: minimum intensity of 1000, minimum products per amino acid of 0.3 and file threshold of 2. After manual curation, Deuteros 2.0 software (*51*) was used for data analysis, visualization and statistical treatments. The mass spectrometry data have been deposited to the ProteomeXchange Consortium via the PRIDE (*52*) partner repository with the dataset identifier PXD027447.

Biophysics

**Products**. Crystallization solutions were from Grenier bio-one. The Mosquito crystallization robot is from TTP Labtech. Crystallization plates and cover were from Grace Bio-Labs. The cryoprotection kit was from Molecular Dimensions. Cryschem plates were from Hampton Research. Vitrobot grid freezing device is from FEI. The Talos Arctica and Titan Krios G3 are from Thermo Scientific.

**X-ray**

*Protein crystallization*. The crystallography step was performed at 19 °C. Crystals were obtained by vapor diffusion on hanging drops. E504A BmrA mutant was concentrated by centrifugation-filtration to 7-10 mg/mL spinning at 500 xg on a 50 kDa cutoff Amicon Ultra-15 at 22 °C. BmrA E504A mutant was then incubated with 5 mM ATP-Mg for 30 min. Crystallogenesis was done by mixing with a Mosquito 450 nL of reservoir solution containing 100 µL 0.1 M Tris-HCl pH 8.5, 23-27% PEG 1000 with 50 nL of compounds 3a-3e and 500 nL of BmrA E504A sample. the mix was deposited on a plastic cover, sealed onto the plate and imaged periodically with a Formulatrix. Crystals appear after 3 days, grown up to 5-8 days and progressively disappeared if the incubation lasted longer.

*Crystal cryocooling*. As BmrA E504A mutant crystals were sensitive to cryoprotection, it was therefore performed using the CryoProtX MD1-61 kit. Best results were obtained with a final

solution containing 12.5% (v/v) di-ethylene glycol, 18% (v/v) 2-methyl-2,4-pentanediol, 7% (v/v) ethylene glycol, 12.5% (v/v) 1,2-propanediol, 12.5% (v/v) dimethyl sulfoxide, supplemented with 5 mM ATP-Mg and 1 mM compounds **3a-3e**. One microliter of cryo-solution was divided in 3 drops under the binocular, close to the drop containing the crystal and then gently brought in contact using the freezing loop, at the opposite side where the crystal was sitting, in the course of 1 min. This operation was performed in Cryschem sitting drop plates, with the drop sitting in the middle of a water-filled reservoir to saturate the solution with humidity. Crystals were then harvested and placed on a fresh drop of cryo-solution for 1 min. before harvesting and cryocooling in liquid $N_2$. Crystals were stored in liquid $N_2$ before being analyzed at the synchrotron.

*Diffraction data acquisition*. Diffraction screening has been performed at ESRF and SOLEIL synchrotrons on multiple beamlines over the years. Best data set was collected on PX2 at SOLEIL, consisting of a low-resolution pass at low transmission, and a high-resolution dataset at full transmission collected helicoidally. Crystal polymorphism was strongly present, precluding data merging among several crystals. Crystals diffracted very anisotropically, going to 3.9 Å resolution in the strongest diffracting direction. Data were processed in XDS as spherical to the highest resolution possible (3.9 Å) even though spherical statistics were not usable. Staraniso analysis for diffraction anisotropy revealed that completeness was 78% in the highest resolution shell, therefore revealing that all the data collectable for this crystal had been collected. Data was cut at the diffraction limits suggested by the Staraniso server. Anisotropic diffraction table is available in supplementary Table 1.

*X-ray structure and model building*. Phases were solved by molecular replacement using Phaser on amplitudes, with data corrected for anisotropy using Staraniso, and using the outward facing conformation dimer of Sav1866 (PDB code ID 2hyd) or MsbA (PDB code ID 3b60) as search models. Although Sav1866 and MsbA structures are very similar, the MsbA model yielded higher molecular replacement solution scores. Crystals belonged to the P21 space group with 2 dimers in the asymmetric unit. The molecular replacement solution was clear, but the electron density was very noisy due to the large conformational changes observed on BmrA, and that resulted in poor overall phases. The core of the protein was nevertheless clearly visible with helices as tubes. The nucleotide-binding domain was very blurry as well as external loops. The model was turned into poly-Ala to place helices of the transmembrane region, and initial movement of the TM1-TM2 hinge. Refinement was carried out in autoBUSTER using corrected amplitudes, applying strict NCS. Iterative manual building in Coot followed by refinement resulted in visible continuous electron density with decreasing R-factors. Density for large amino acids appeared, as well as for ATP. Sequence was assigned, and iterative refinement continued with introduction of TLS refinement (1 TLS per chain, 4 total). It yielded R-factors around 30 and 35 for R and Rfree respectively, with small grooves in the helices. Re-definition of TLS (1 for a dimer of TMD, 1 for a dimer of NBD, 4 total) resulted in a dramatic decrease of R-factors by 3 points, and much clearer electron density features, helices with large grooves and side chain density. Unwinding of TM3 next to residue 136 was apparent, as well as helix breaks in the trans-membrane region and clear density for ATP. Some incorrect modeling of ATP became apparent with negative and positive density showing where the correct position was then defined. NCS was relaxed and correct modeling of geometry clashes was carried out in ISOLDE. Registry was built by starting to assign using initial first large density features clearly visible as refinement converged for the TMD, then using superpositions for the NBD. Registry at key locations was then probed by replacing several amino-acids, or by trying to turn helices by one amino-acid clockwise or counterclockwise and probed by refinement. Newly refined structures clearly showed positive or negative densities indicative of incorrectly modeled features, thus granting the modelling of a full amino-acid model guided by restrained-refinement. Ramachandran and

rotamers outliers were corrected, yielding a final model with R = 26.0% and Rfree = 32.1%. The final model was deposited in the Protein Data Bank under the accession code 6r72.

**Cryo-EM**

***BmrA E504A [ATP-$Mg^{2+}$, R6G] sample***

*Sample preparation*. Detergent-purified BmrA E504A mutant at 3.4 mg/mL was incubated with 0.1 mM R6G for 30 min at 4 °C, followed by addition of 5 mM ATP-Mg in the same conditions. Three microliters of this mixture were applied to cryo-EM Au-grids (Cflat 1.2/1.3 3Au) previously discharged in air for 40 s at 20 mA (PELCO easiGlow), blotted for 3 s, and plunge frozen in liquid ethane with a Vitrobot grid freezing device.

*Data acquisition*, image processing. Best grids screened with a Talos Arctica were then imaged with a Titan Krios G3 electron microscope equipped with a K2 camera and operating at 300 keV. A total of 3477 movies of 40 frames each were acquired over 2 data-collection sessions originating from the same grid in electron counting mode at 1.06 Å/pixel, 6.4 electrons/pixel/s, with a total exposure time of 6 s and combined into a single MRC stack using EPU automatic data collection control software using defocus values ranging from 1.2 to 3.2 µm. Contrast transfer function (CTF) parameters were estimated from the averaged movie with CTFFIND4 and 2170 particle images were selected manually and subjected to 2D classification in cryoSPARC v2. Automatic particle selection was performed with templates from the 2D classification. Beam induced particle motion between fractions was corrected with a new implementation of alignparts lmbfgs in cryoSPARC v2. The number of particle images were reduced to 128372 by further 2D and 3D classifications and refinements. Models were calculated ab initio and refined without the application of symmetry with cryoSPARC v2. For each data collection session automatically picked particles were cleaned with 2 rounds of 2D classification followed by a preliminary round of 3D classification to further remove obvious junk particles such as empty detergent micelles that were not eliminated during the 2D classification process. Although no discrete conformation could be isolated to high resolution, removal of additional particles improved the resolution of the final maps suggesting significant non-discrete or continuous flexing. Since these maps suggested a significant amount of small, non-discrete flexing, better resolved maps were obtained using cryoSPARC v2's non-uniform refinement feature. An additional refinement with the application of C2 symmetry was performed that resulted in a gain of 0.3 Å in overall resolution which helped to slightly improve the interpretability of the map in the model building process. The asymmetric and C2 symmetrized maps have been deposited in the Electron Microscopy database under the accession codes EMD-4749 and EMD-12170 respectively.

*Model building and refinement*. The X-ray model was docked into a 3.9 Å C2 symmetrized cryo-EM density map and improved with iterative rounds of manual building in Coot and Isolde followed by real_space_refine in Phenix. Of Note, sharpening the C2 symmetry map using Phenix led to improved features in the trans-membrane domain, but worse in outer loops and the NBD. The final model was thus built using both sharpened and unsharpened maps. The final model was validated with MolProbity and EMringer and deposited in the Protein Data Bank under the accession code 6R81 and electron microscopy database EMDB-4749.

Two small densities were visible in the C2 symmetrized map at the locations of R6G. Re-examination of the data with no symmetry led to the identification of clearer densities in which R6G could be placed and suitably refined. Notably, both densities are not equivalent in the two halves of BmrA, suggesting that in both binding sites there is a heterogeneity/flexibility of binding, reminiscent of substrate release. Understandably, the application of C2 symmetry masked the quality of the reconstructions at these locations since these sites are not identical with respect to R6G binding. Thus, BmrA was refined in the

presence of R6G, following the same procedure as above using the asymmetric map. Final model and maps were deposited in the Protein Data Bank under the accession code 7bg4 and electron microscopy database EMD-12170. Model statistics are provided in supplementary Table S2.

***BmrA E504A [ATP-$Mg^{2+}$] sample***

*Sample preparation*. Detergent purified BmrA E504A mutant at 3.8 mg/mL was incubated with 5 mM ATP-Mg for 30 min at 4 °C.

Three microliters of this mixture were applied to cryo-EM Au-grids (Cflat 1.2/1.3 3Au) previously discharged in air for 40 s at 20 mA (PELCO easiGlow), blotted for 3 s, and plunge frozen in liquid ethane with a Vitrobot grid freezing device.

*Data acquisition*, *image processing*. Grids were imaged with a Titan Krios electron microscope equipped with a K2 camera and operating at 300 keV. A total of 4,221 movies of 40 frames each were acquired in electron counting mode at 1.052 Å/pixel, 8.4 electrons/pixel/s, with a total exposure time of 5 s and combined into a single MRC stack using SerialEM automatic data collection control software using defocus values ranging from -0.8 to -2.2 µm. All processing was done in cryoSPARC v3.1, including motion correction and CTF estimation. Automatic particle picking (blob picker) on the first 200 micrographs followed by 2D classification and particle selection, was then fed into a template picker for the entire data set. Several rounds of 2D classification narrowed down the total amount of particles to about 1 million, which was subjected to ab-initio model generation. The number of particles were reduced to 327,764 by further 3D classifications and refinements. The best resolution was obtained using Non-Uniform refinement in cryoSPARC v3.1 using C2 symmetry. Note that the influence of the amphipathic belt on reconstruction was tested by performing particle subtraction using a mask encompassing the amphipathic belt, followed by focused refinement. A 0.2 Å decrease in overall resolution was observed as expected (FSC=0.143) but no difference was observed on the protein map quality. The maps deposited were thus without particle subtraction. The C2 symmetrized maps have been deposited in the Electron Microscopy database under the accession codes EMD-13095.

*Model building and refinement*. The X-ray model was docked into a 3.6 Å C2 symmetrized cryo-EM density map using Phenix dock_in_map. The model was improved with iterative rounds of manual building in Coot (0.9.4) and Isolde v1.2 followed by real_space_refine in Phenix. No map sharpening was performed on this map. The map quality was of higher quality than the X-ray or cryoEM map with R6G and allowed to build a BmrA model comprising the loop between TM5-6 that was missing in the previous structures. The final model was validated with MolProbity (Phenix) and Coot and deposited in the Protein Data Bank under the accession code 7ow8 and electron microscopy database EMDB-13095. Model statistics are provided in supplementary Table S2.

Bioinformatics

Both the X-ray (6r72) and the cryo-EM (C2, 7bg4 with and without R6G) structures span residues 10 to 589, and both miss a few residues (271-278 in the X-ray structure, 273-278 in the cryo-EM structure), corresponding to the loop region between TM5 and TM6. Complete models of dimeric WT BmrA were generated using Modeler (v9.12), for both the X-ray and the cryo-EM structures, using the structure of the ABC transporter related protein from *Novosphingobium aromaticivorans* (PDB code ID 4mrs) (*53*) as a template for the missing residues, and the alignment generated by HHPred (*54*). The N-termini were capped with acetyl groups, and the missing N-terminal residues were not modeled. Both models contained ATP molecules and $Mg^{2+}$ ions, as observed in both the X-ray and the cryo-EM structures. The models were then oriented using the OPM server (http://sunshine.phar.umich.edu/server.php)

(*55*) and embedded into a mixed POPE/POPG bilayer (ratio 3/1) using the CHARMM-GUI membrane builder (*56*), and the replacement method. The systems were solvated and 150 mM KCl was added to the solution, yielding a total of ~157,000 atoms in tetragonal boxes of dimensions ~100x100x165 $Å^3$. CHARMM-GUI web server was used also to build R6G in POPC lipid bilayer.

***Simulations without R6G***.
All simulations were run with the GROMACS (v2016.4) software package (*57*). The CHARMM36 force field was used for both the lipids and the protein, together with the CHARMM TIP3P water model. Non-bonded interactions were calculated with a cutoff of 1.2 Å, with a shift function on the potential to avoid discontinuities. Neighbor lists were updated using the Verlet scheme. Long-range electrostatic interactions were calculated with the Particle Mesh Ewald method (*58*). Bonds involving hydrogen atoms were constrained using the P-LINCS algorithm (*59*).
Each system was minimized by steepest descent and then equilibrated using a 6-cycle equilibration scheme, using position restraints on the protein and gradually reducing the force constant. Equilibration and production runs were performed at 303.15 K and 1 bar; the temperature was kept constant with the velocity rescale algorithm (*60*) and the pressure with the Parrinello-Rahman barostat (*61*). The integration time step was set to 2 fs. For each system, four replicates were simulated for 500 ns each. The first 200 ns of each simulation were treated as equilibration, and average quantities (average structures, inter-atomic distances, RMSD, RMSF, B factors) were computed on the remaining 300 ns. Two additional replicates were run with long equilibration steps (275 ns before 500 ns of production) to confirm the closing movement of the cavity. Due to the relatively large size and the transmembrane nature of BmrA, we expect functional motions of the transport cycle to take place on time scales much longer than the simulation time (probably 3-4 orders of magnitude longer), which are currently not accessible by all-atom molecular dynamics. Therefore, we only expect to observe relatively fast conformational changes, and changes driven by strong driving forces.

***Simulations with R6G.***
*System setup*. R6G was first extracted from the structure with BmrA E504A and then parametrized with CHARMM General force field (CGenFF) program (*62*) to provide the initial topology file of the R6G molecule compatible with the CHARMM36 force field. Some of the topology parameters required optimizations and verifications because of their high penalty scores. Hence, we carried out molecular dynamic simulations of the R6G molecule alone with 300 POPC molecules forming the lipid membrane for 500 ns at 303 K. The resulting values were used for carrying out three unbiased simulations of two R6G molecule incubated with BmrA and reconstituted in 276 POPE:POPG (3:1 ratio) forming a lipid membrane, ran for 1 µs at 303 K.

*Parametrization of Rhodamine.* The parametrization was carried out following the procedure previously described (*62*). Once the initial topology file was obtained, we carried out molecular dynamic simulations of R6G in POPC membrane for 500 ns and clustered the most probable conformations of R6G in the lipid bilayer (Fig. S18AB). In GROMACS, the *gmx cluster* program allowed clustering the most preferred conformations of R6G during the simulation time. For each conformation, we used the CGenFF program to generate the corresponding topology files, which were then averaged to create the final topology file (Fig. S18C).

*Unbiased simulations.* The system including BmrA E504A, ATP-$Mg^{2+}$, R6G, lipids and water was minimized by steepest descent and then equilibrated using a 7-cycle equilibration scheme,

using position restraints on the protein and gradually reducing the force constant. Three replicates were simulated for 1 μs using different starting velocities.

*Calculating the distances in simulations.* We calculated the distance between the center of mass (COM) of the two R6G molecules and the COM of the protein (along the bilayer normal vector, *i.e.*, the z axis), using the GROMACS command *gmx distance*.

*Calculating the number of contacts between the molecules.* The number of contacts of R6G with water, protein and lipids were quantified during the simulations runs with the GROMACS command *gmx mindist,* considering a maximal distance between the respective COMs of 0.4 nm.

**Fig. S1.**

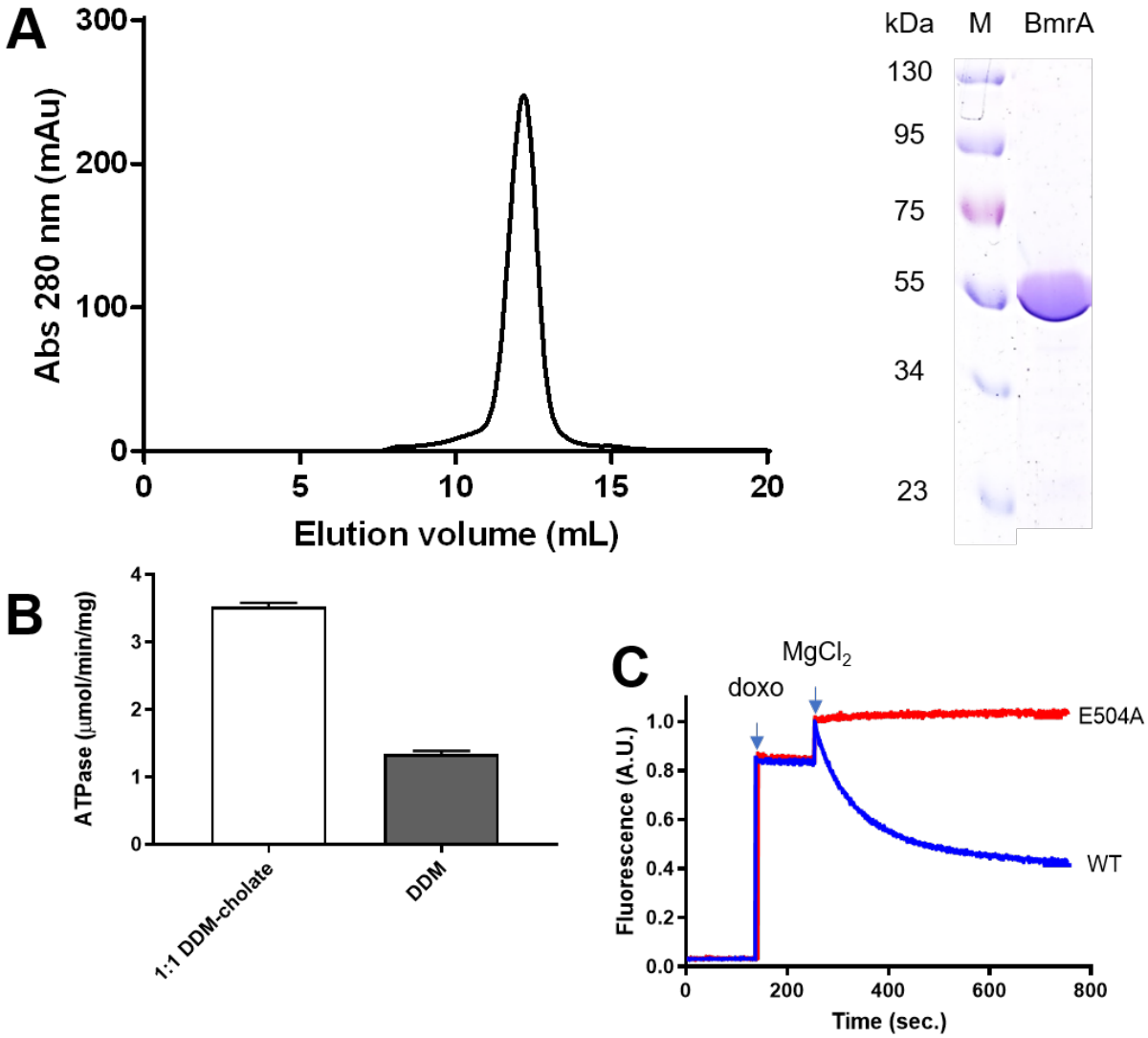


**Fig. S1. Purification of BmrA, ATPase activity and transport assay**. **(A)** Preparative SEC profile of detergent purified BmrA (left panel). The peak fraction was analyzed by SDS-Page (right panel). **(B)** ATPase activities of WT BmrA purified with DDM or DDM-cholate mixture. **(C)** Doxorubicin (doxo) transport activity of WT BmrA and the inactive E504A mutant.

Fig. S2.

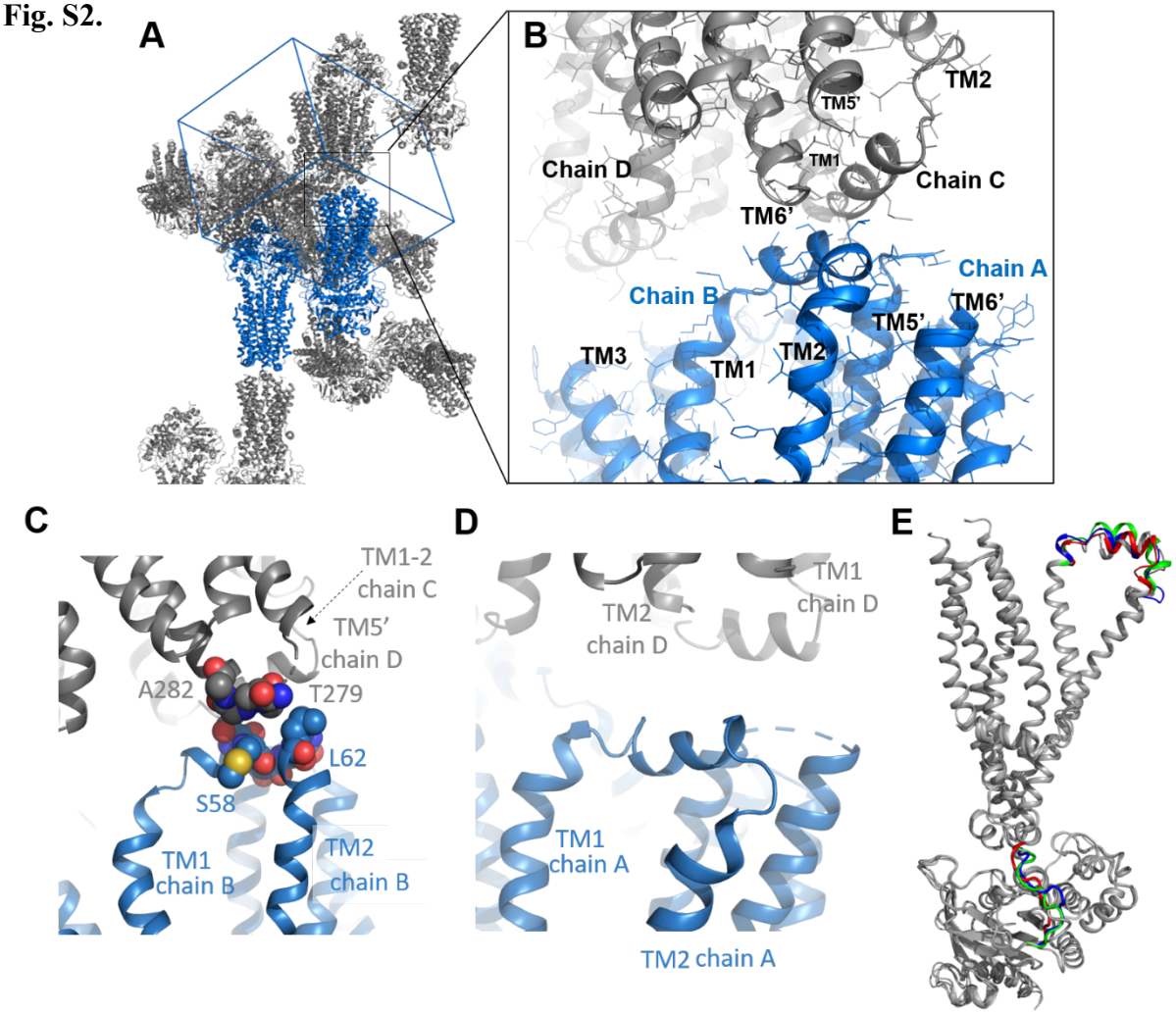


**Fig. S2**. **Crystallographic packing and difference between monomers in the asymmetric unit. (A)** Overall crystal packing. The 4 BmrA monomers A-D of the asymmetric unit, assembled in 2 dimers, AB colored in blue, and the symmetric dimer CD in grey. Proteins are represented as cartoon, and the cell is drawn in blue. (**C**) TM1-2 of chain B interacts with TM5-6 of chain D, and of TM1-2 of chain C (in the back). (**D**) TM1-2 of chain A and chain D are free of crystal contact interactions. **(E)** Differences between monomers in the X-ray structure. Structures are represented in cartoon, colored in grey. Flexible regions are highlighted in green (chain B), blue (chain C) and red (chain D). Each 4 monomers of the asymmetric unit of the crystallographic structure were superposed onto chain A.

**Fig. S3.**

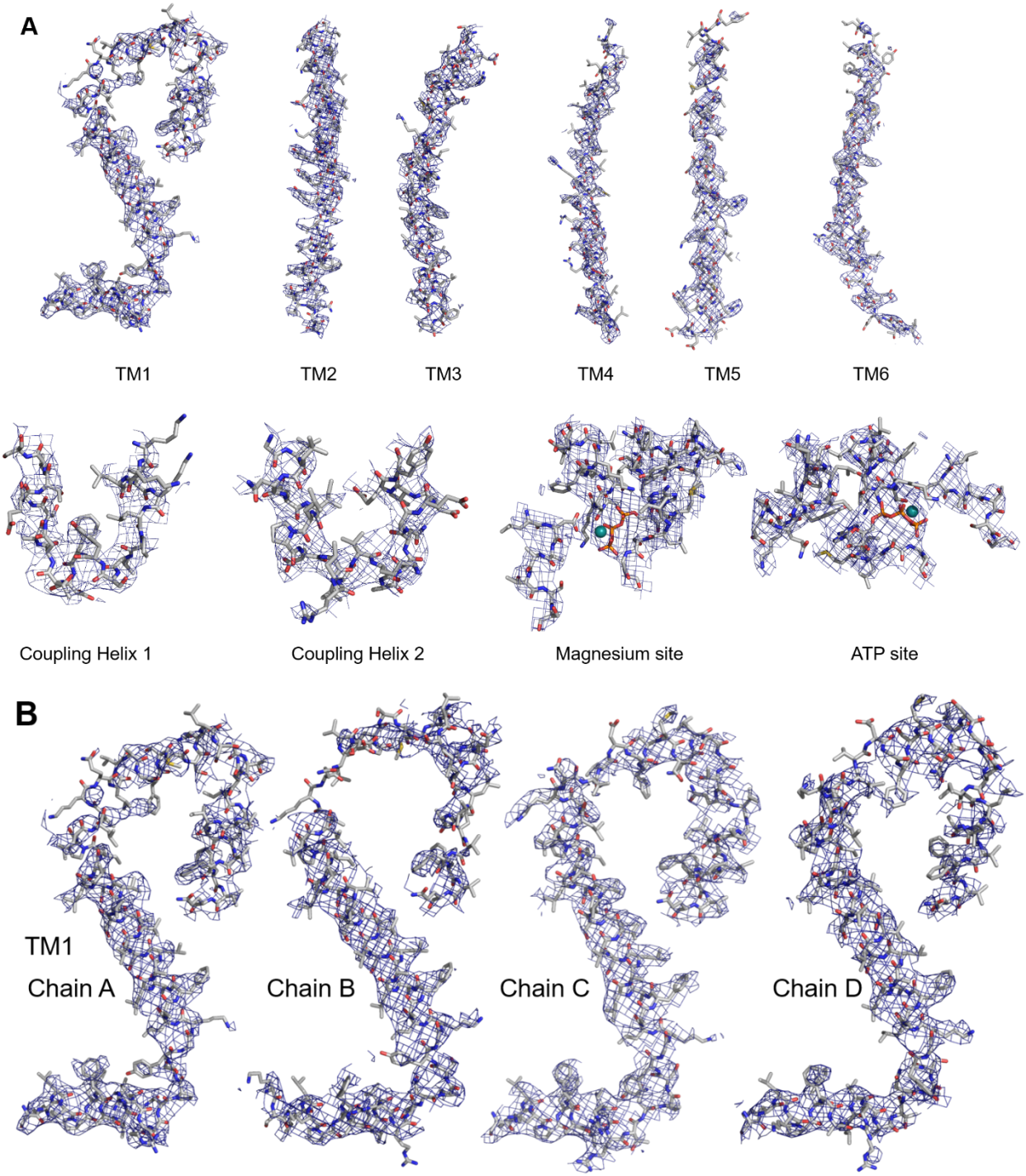


**Fig. S3**. **X-ray 2mFo-DFc density maps of BmrA**. **(A)** TM helices, coupling helices and ATP-$Mg^{2+}$ binding site of chain A. **(B)** Densities displayed at 1σ of the TM1-extracellular loop 1 for each chain.

.

**Fig. S4.**

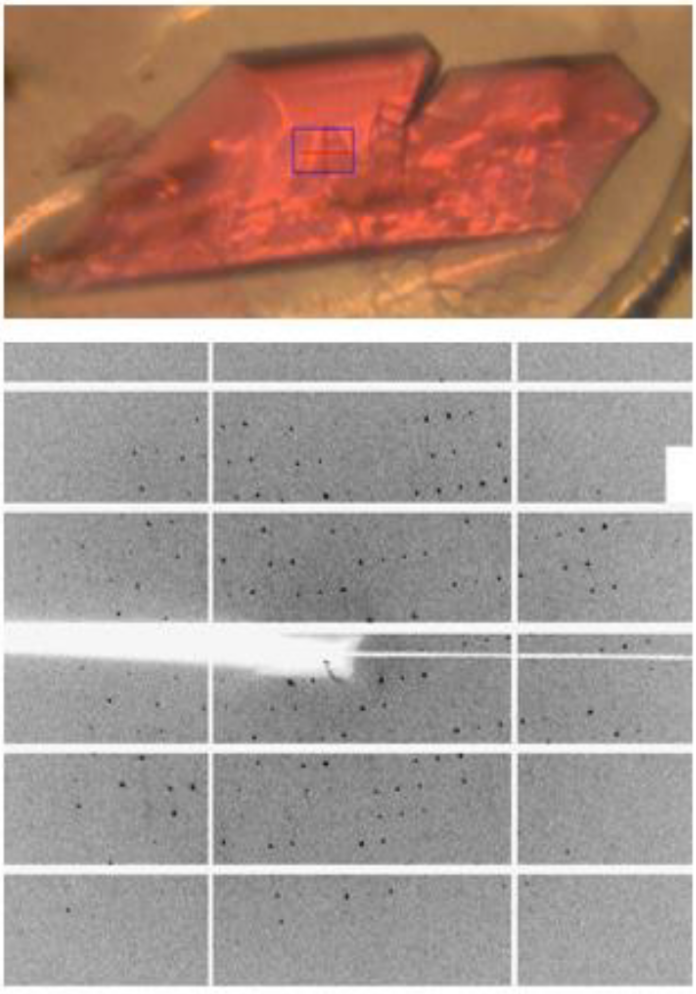

**Fig. S4. Crystallization of BmrA E504A in complex with ATP-$Mg^{2+}$ and R6G**.

**Fig. S5.**

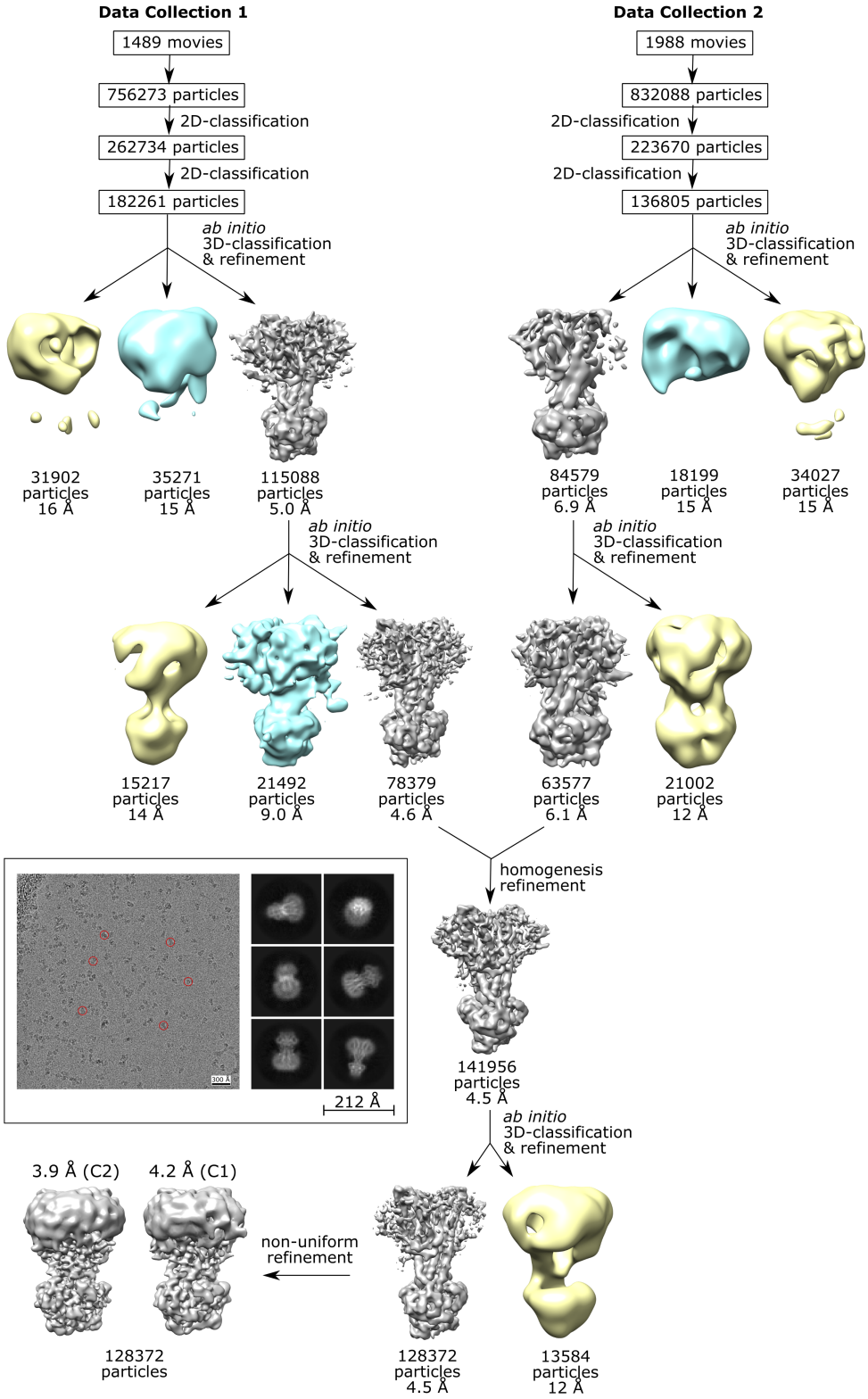


**Fig. S5. Image collection, 2D-3D classification, and processing workflow of cryo-EM image analysis of BmrA in complex with R6G**. Micrographs from two separate data collection sessions done on the same sample and grid were processed in parallel and the best particles from each session were later combined to produce the final maps. For each session, picked particles were cleaned using 2 rounds of 2D classification followed by a 3D

classification. Heterogeneity within the dominating outward-facing conformation was further assessed with additional rounds of 3D classification that removed an additional 35 % of the outward-facing particles. Although removal of these particles improved the resolution of the dominating outward-facing conformation, discrete conformations could not be refined to high resolution suggesting that a large degree of small, non-discrete flexing was interfering with particle alignment. Due to the significant flexing amount, the final maps were refined using cryoSPARC's non-uniform refinement feature resulting in better resolved maps. An additional refinement with the application of C2 symmetry was performed that resulted in an improvement in resolution. **Boxed**: example micrograph with particles used for 2D classification (red circles), and corresponding representative 2D class averages.

**Fig. S6.**

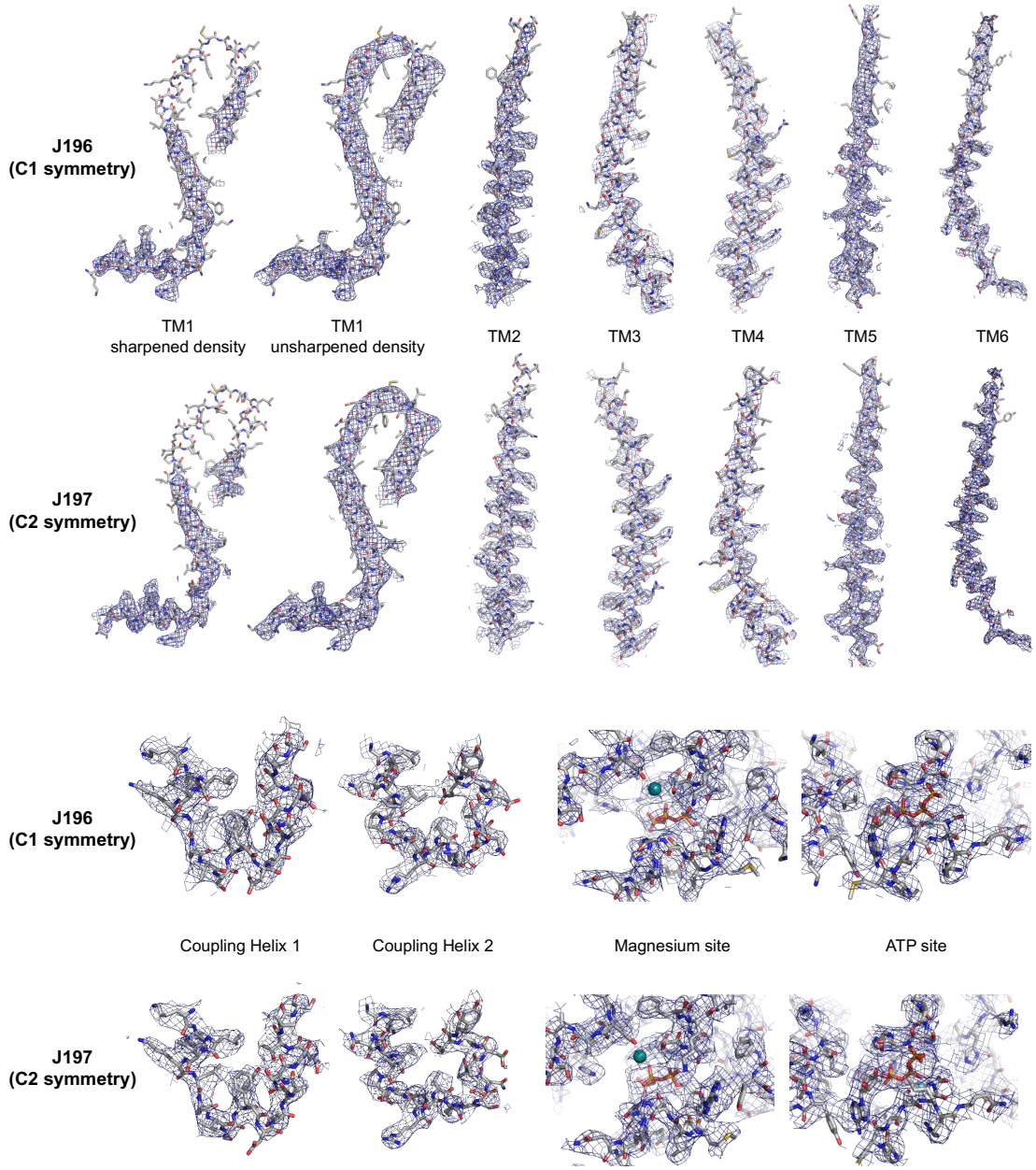


**Fig. S6**. **Cryo-EM densities of BmrA E504A [ATP-$Mg^{2+}$, R6G]**. Sharpened EM densities of the TM helices (and also unsharpened for TM1), coupling helices and the Magnesium and ATP binding sites for J196 (C1, no symmetry) and J197 (C2 symmetry map). Densities are displayed at 1.0σ.

**Fig. S7**

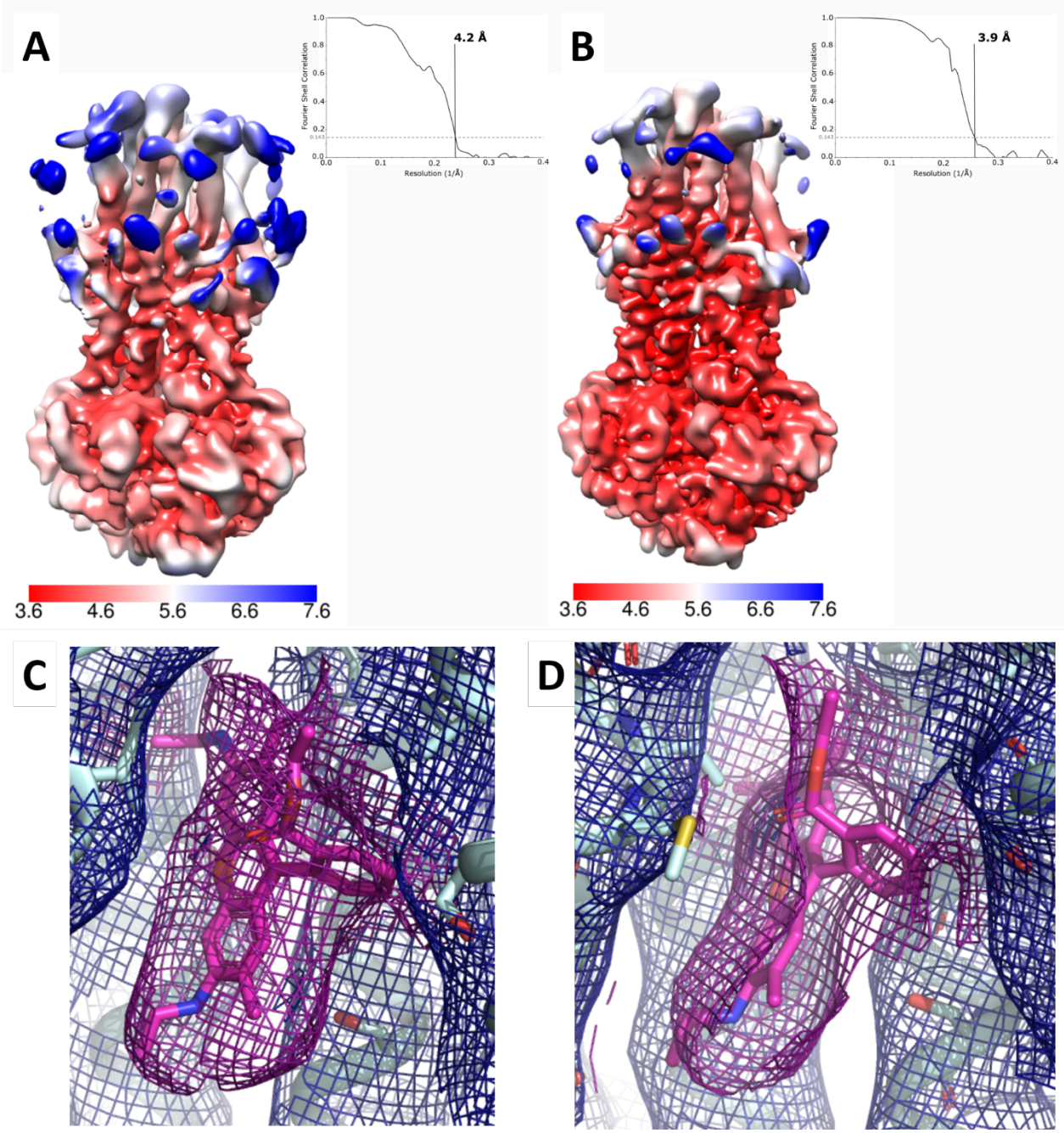
A
4.2 Å
Fourier Shell Correlation
Resolution (1/Å)
3.6 4.6 5.6 6.6 7.6
B
3.9 Å
Fourier Shell Correlation
Resolution (1/Å)
3.6 4.6 5.6 6.6 7.6
C
D

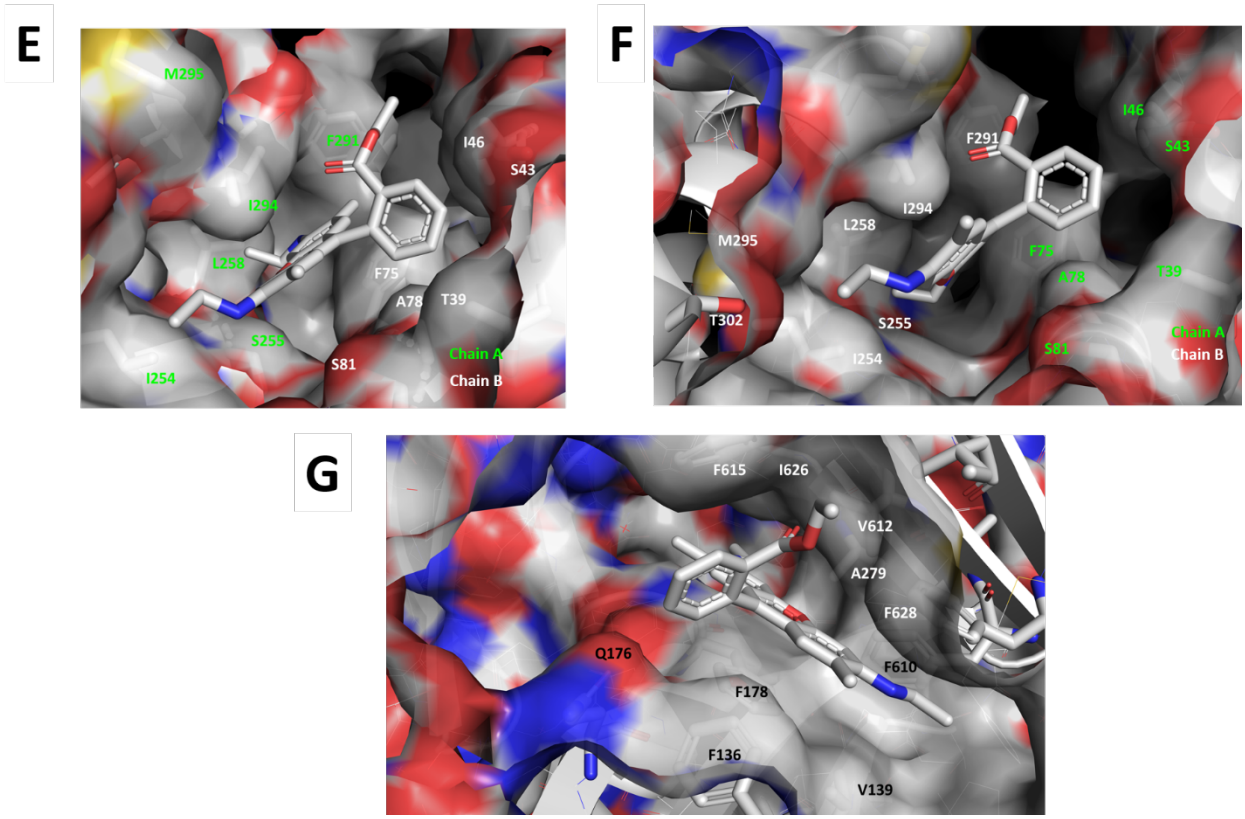


**Fig. S7**. **Assessment of the cryo-EM data**. (**A, B**) Local-resolution estimation of the C1 (**A**) and C2 (**B**) density maps and their corresponding Fourier Shell Correlation (FSC). (**C, D**) Unsharpened C1 maps (no symmetry) of the R6G-binding sites. Densities are displayed at 2.0σ. (**E-F**) Molecular interactions of the two R6G in their binding sites. (**G**) R6G-binding site of AcrB (*30*).

**Fig. S8.**

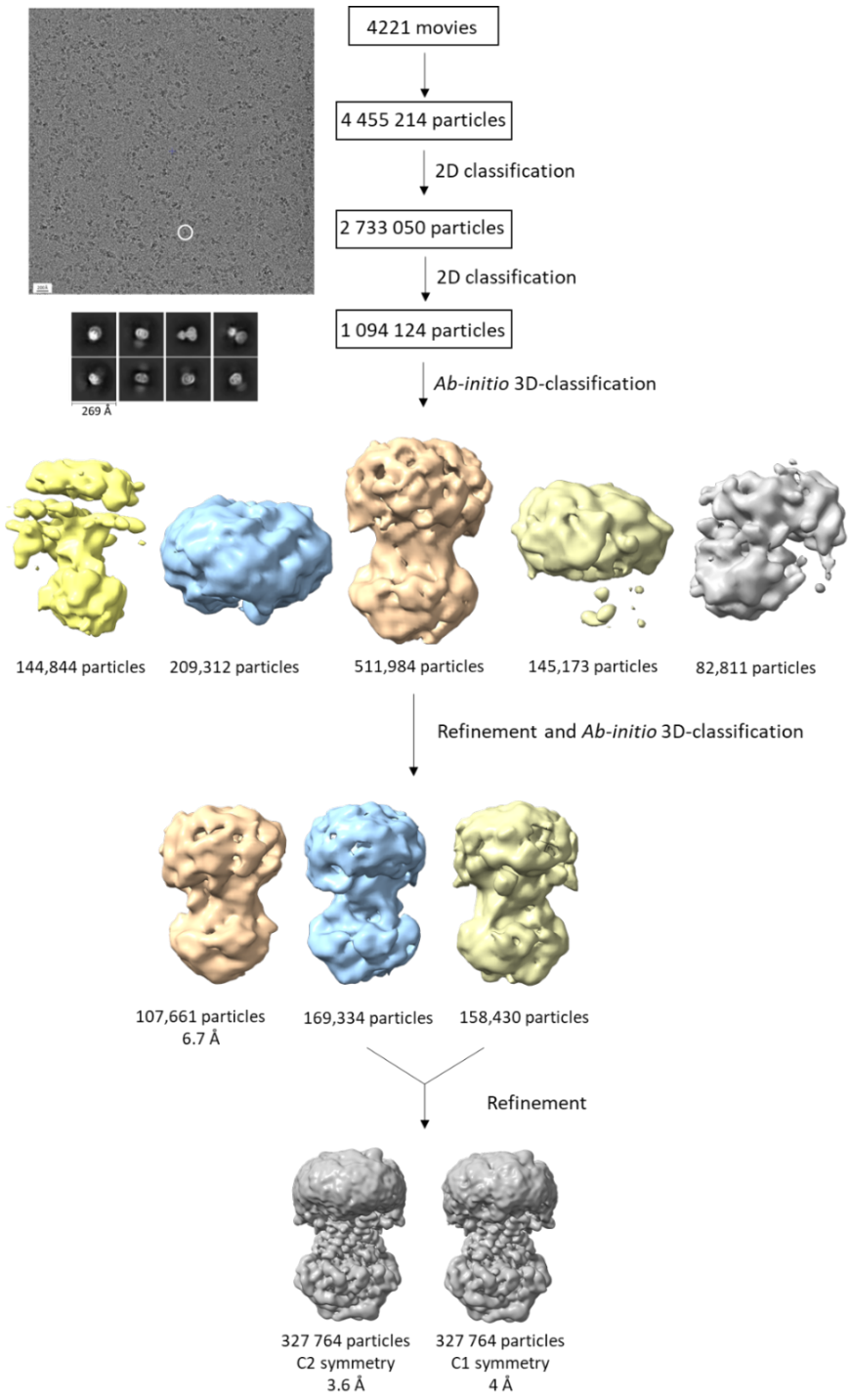


**Fig. S8**. **Image collection, 2D-3D classification, and processing workflow of cryo-EM image analysis of BmrA E504A [ATP-$Mg^{2+}$] condition**. All particles originated from a single data collection with a straightforward data processing scheme, initialed by 2D classification, followed by 2 rounds of 3D classification and refinement. The final maps with C2 symmetry were deposited in the EMDB. A representative micrograph with particles used for 2D classification (white circle), and corresponding representative 2D class averages are displayed.

**Fig. S9.**

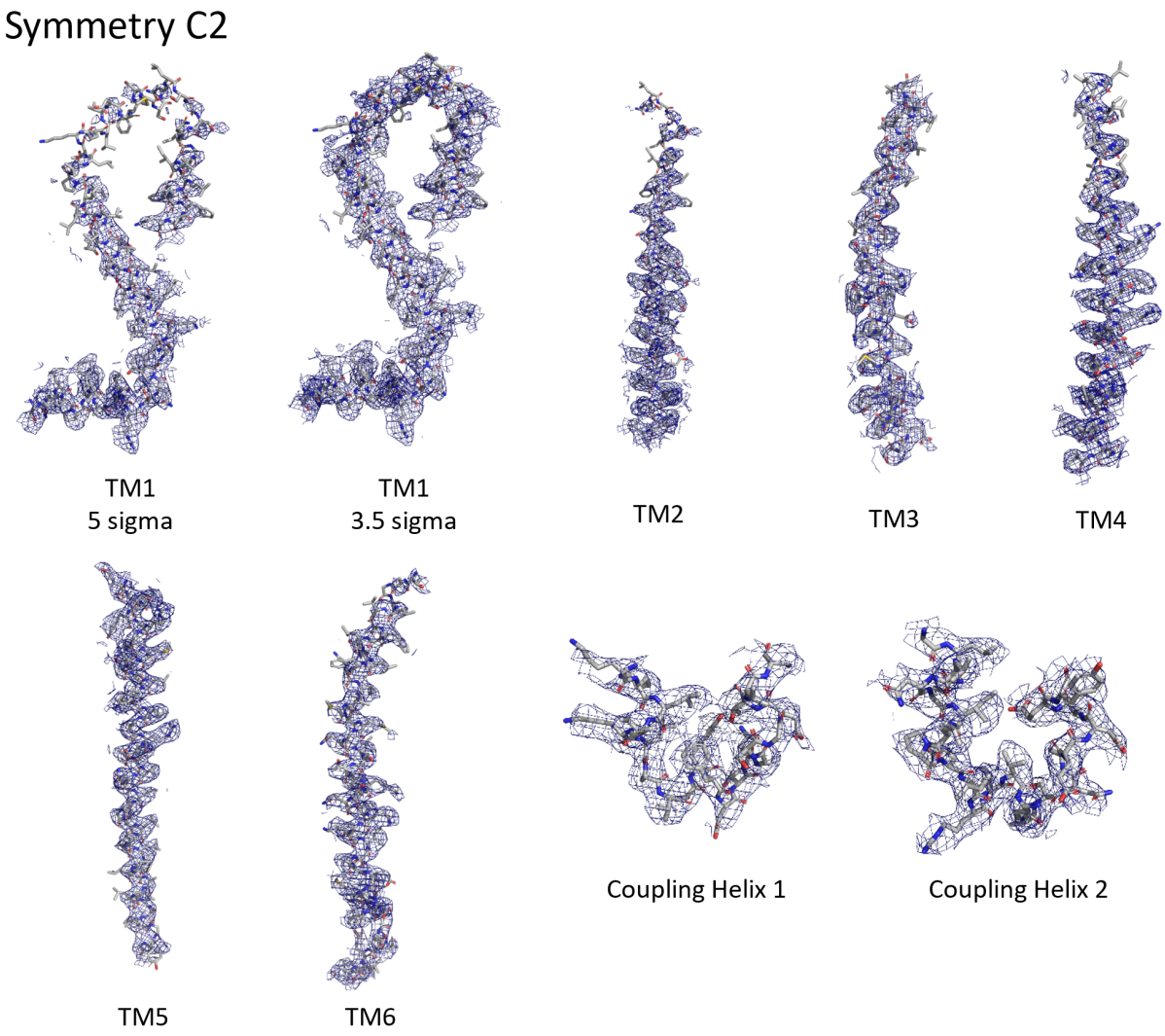


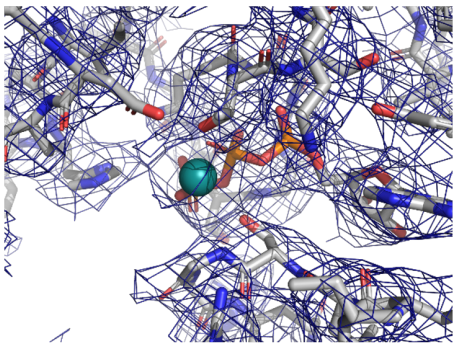

Magnesium site

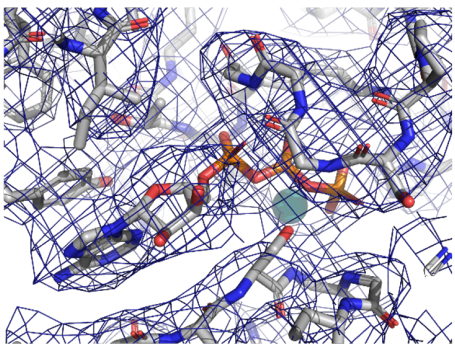

ATP site

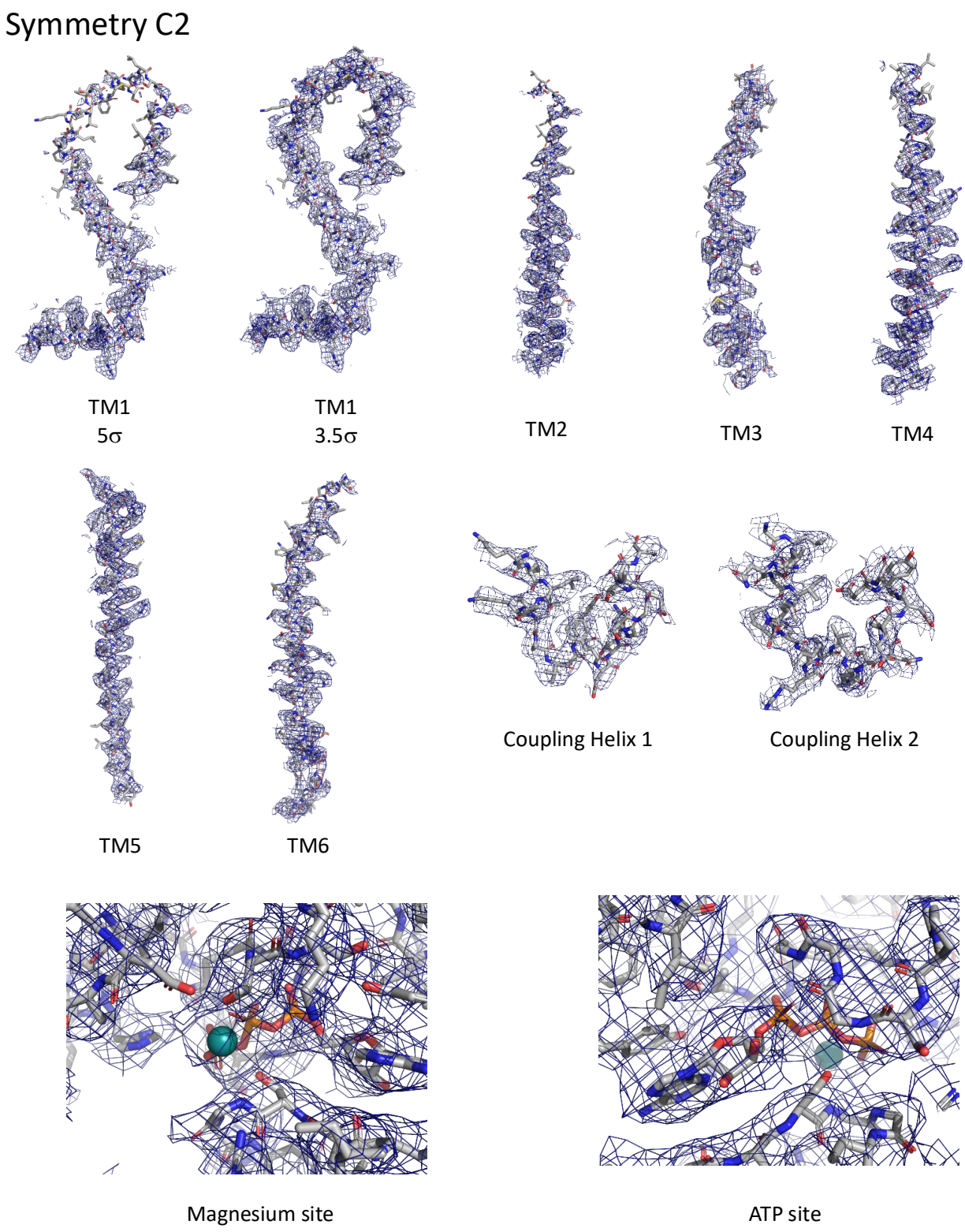


**Fig. S9**. **Cryo-EM densities of BmrA E504A [ATP-$Mg^{2+}$]**. Unsharpened EM densities of the TM helices, coupling helices, and the Magnesium and ATP binding sites for the map with C2 symmetry. Densities are displayed at 5.0σ unless written differently.

**Fig. S10.**

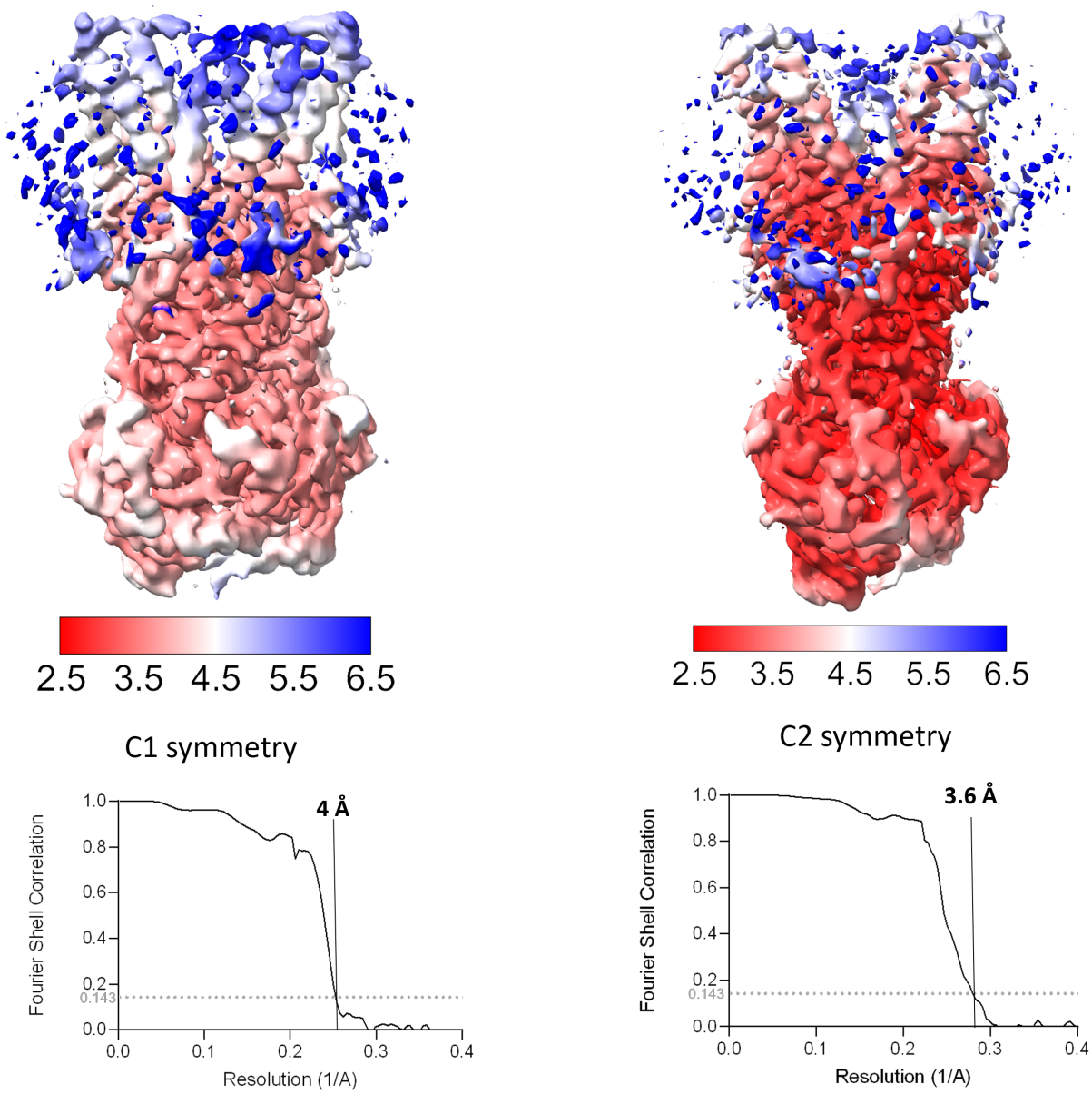


**Fig. S10**. **Assessment of the cryo-EM data for BmrA E504A [ATP-$Mg^{2+}$]**. Local-resolution estimation of the C1 and C2 density maps and their corresponding Fourier Shell Correlation (FSC) with resolution given for FSC value of 0.143.

**Fig. S11.**

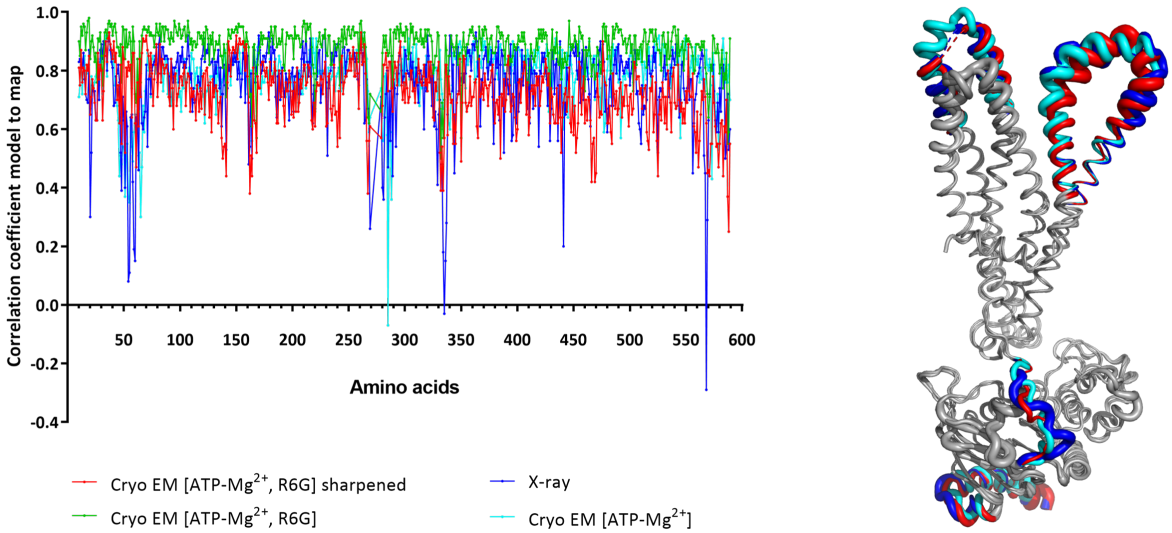


**Fig. S11**. **Correlation coefficient model to map and identification of the flexible parts of X-ray and cryo-EM structures**. **(A)** The value of correlation coefficient model to map was calculated for each model against the corresponding density map. The results are plotted as a function of the amino acid sequence (X-ray in blue, cryo-EM unsharpened in green and sharpened in red). **(B)** The X-ray and the cryo-EM structures are superposed; the flexible parts are colored in red and blue for the cryo-EM and X-ray structure, respectively. These flexible parts correspond to the lowest CC values. The cartoon is represented with the thickness of the sausage corresponding to the B-factor, the higher the B-factor, the larger the sausage.

**Fig. S12.**

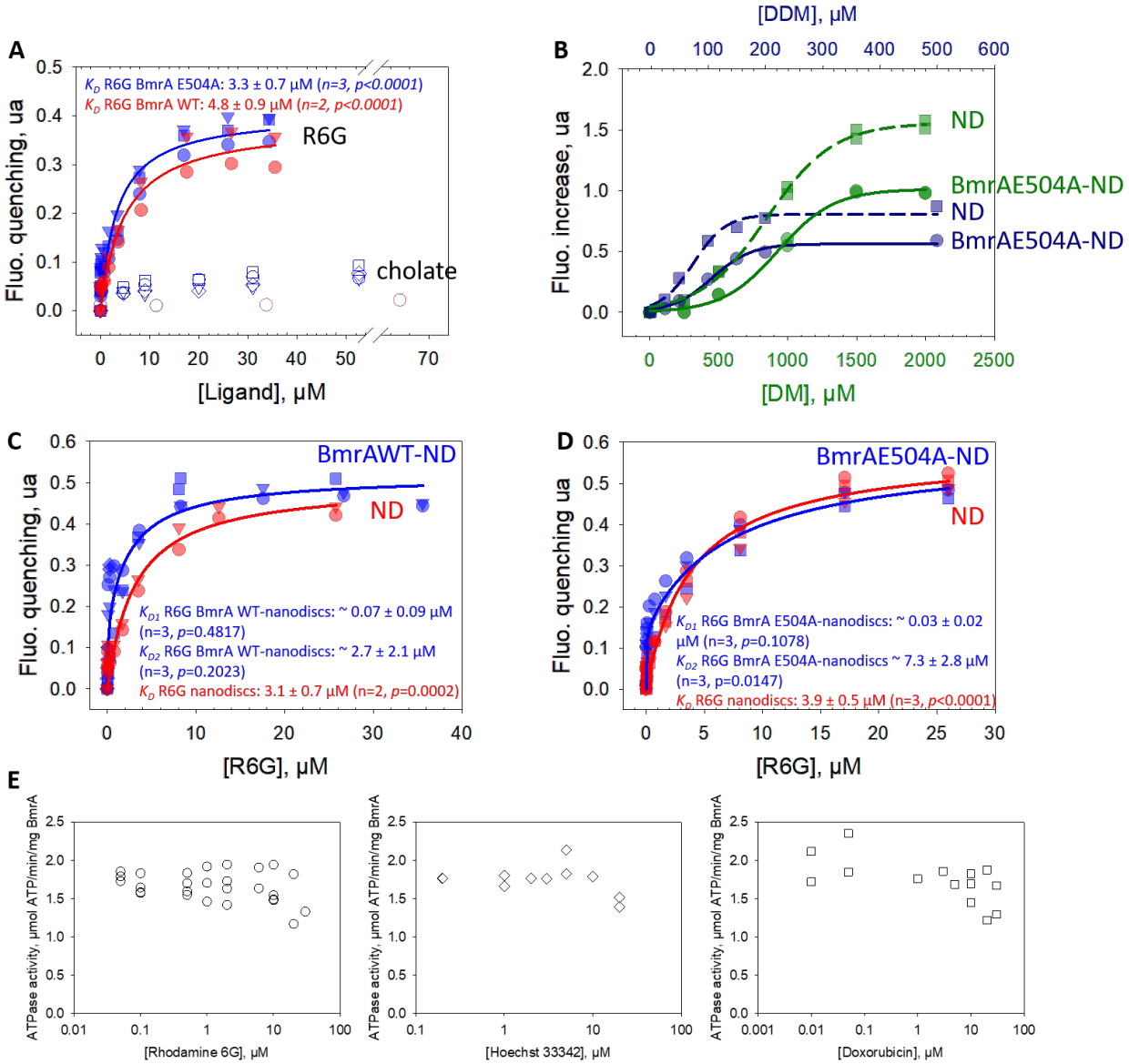


**Fig. S12**. **Binding of compounds to BmrA probed by intrinsic fluorescence.** (**A**) Binding of R6G (filled symbols) and cholate (empty symbols) to BmrA WT (red) or E504A mutant (blue) purified in DDM. Data were fitted with equation 1. No significant fluorescence change was observed upon cholate addition in same conditions. (**B**) Effect of DDM (blue) and decyl maltoside (DM, green) on empty nanodiscs (ND) and BmrA-nanodiscs complexes. BmrA E504A was purified in DDM and then reconstituted into nanodiscs to which DM or DDM were added. The same experiments were done with empty nanodiscs (ND). Data were fitted using equation 3, giving a half-maximal fluorescence increase detergent concentration, $[DDM]_{50}$, of ~106 ± 6 µM (n = 1, $p < 0.0001$) and ~74.1 ± 7.7 µM (n = 1, $p < 0.0006$), and $[DM]_{50}$ of 931 ± 23 µM (n = 2, $p < 0.0001$) and 850 ± 21 µM (n = 2, $p < 0.0001$) for the BmrA-nanodiscs complexes and empty nanodiscs, respectively. (**C**, **D**) Binding of R6G to BmrA WT-nanodiscs (**C**, blue), BmrA E504A-nanodiscs (**D**, blue) and corresponding empty nanodiscs (**C** or **D**, red). The amount of empty nanodiscs used in these experiments correspond to that of MSP1E3D1 proteins in complex with BmrA, estimated by SDS-PAGE using each purified protein as standard. Data best fitted with equation 1 for empty nanodiscs (one site saturation) and equation 4 for BmrA-nanodiscs complexes (two sites saturation). (**E**)

Specific ATPase activity of BmrA reconstituted into nanodiscs, in the presence of substrates. WT BmrA was purified in DDM and then reconstituted into nanodiscs as above to which the indicated concentrations of substrates were added, followed by the measure of the ATPase activity using the coupled-enzyme system. The amount of BmrA was determined by SDSPAGE. The ATPase activity in absence of substrate was ~1.8 µmol ATP/min/mg. Data correspond to 2 to 4 independent experiments.

**Fig. S13.**

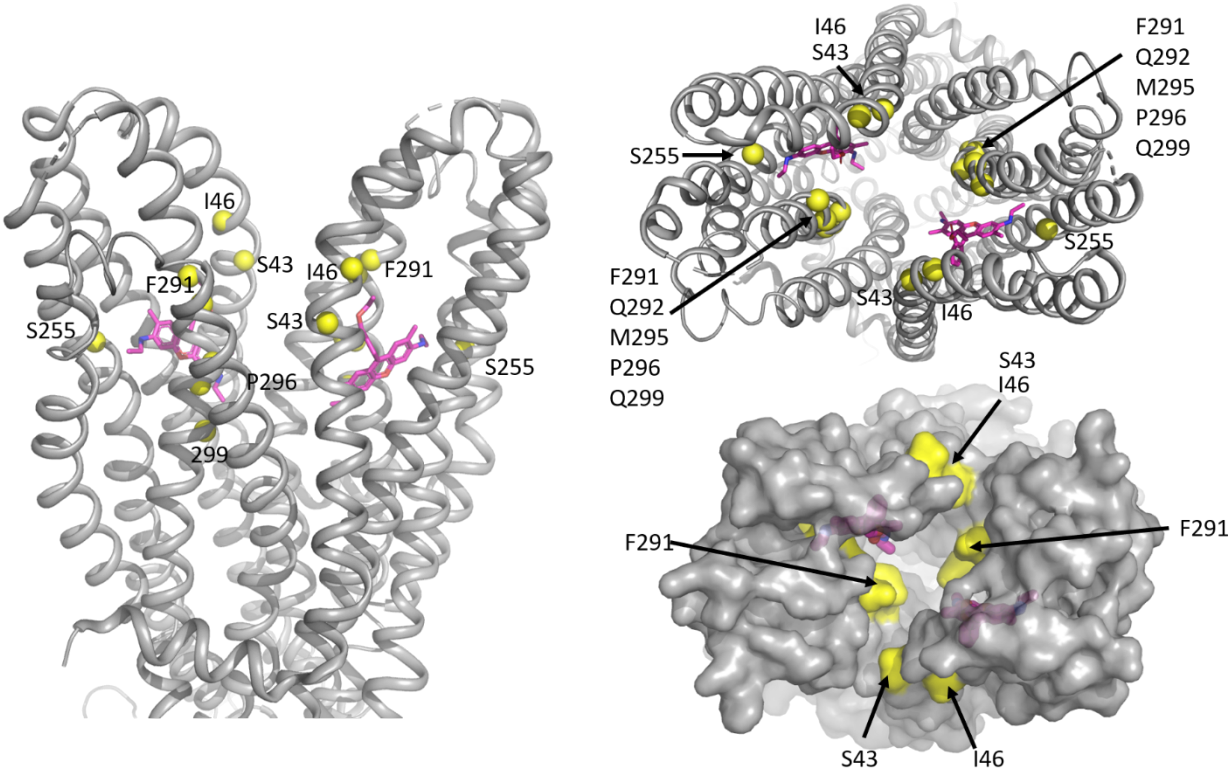


**Fig. S13. BmrA residues equivalent to those of the human ABCB1 involved in Taxol binding**. Cryo-EM BmrA structure is displayed in grey in which residues in yellow correspond to those involved in taxol binding in the human ABCB1 (*14*).

**Fig. S14.**

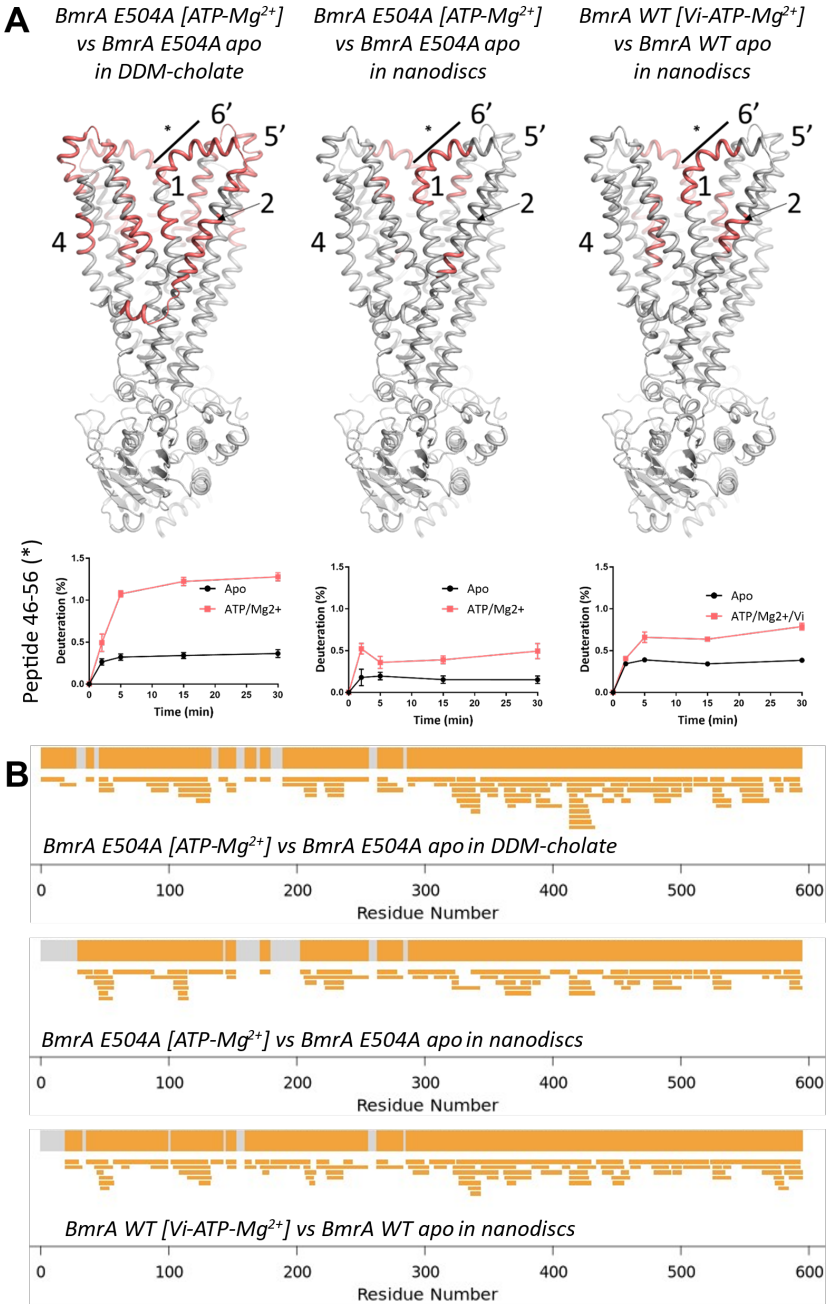


**Fig. S14. Transmembrane regions of BmrA showing an increased accessibility to deuterium upon transition to the OF state as probed by HDX-MS**. (**A**) BmrA WT or E504A were prepared either in DDM-cholate mixture or reconstituted in nanodiscs. Data were recorded after 30 min $D_2O$ exchange and only the transmembrane peptides with increased deuterium uptake in the ATP-bound (for E504A) or Vi-trapped (for WT) conformation as compared to the apo state are shown (salmon color, $p < 0.01$). The star indicates the position of the peptide 46-56 for which the deuterium uptake is plotted as a function of time. (**B**) BmrA sequence coverage maps. The sequence coverage was ~93% and ~86% for the E504A mutant in DDM-cholate and nanodiscs, respectively, and ~93% for the WT in nanodiscs.

**Fig. S15.**

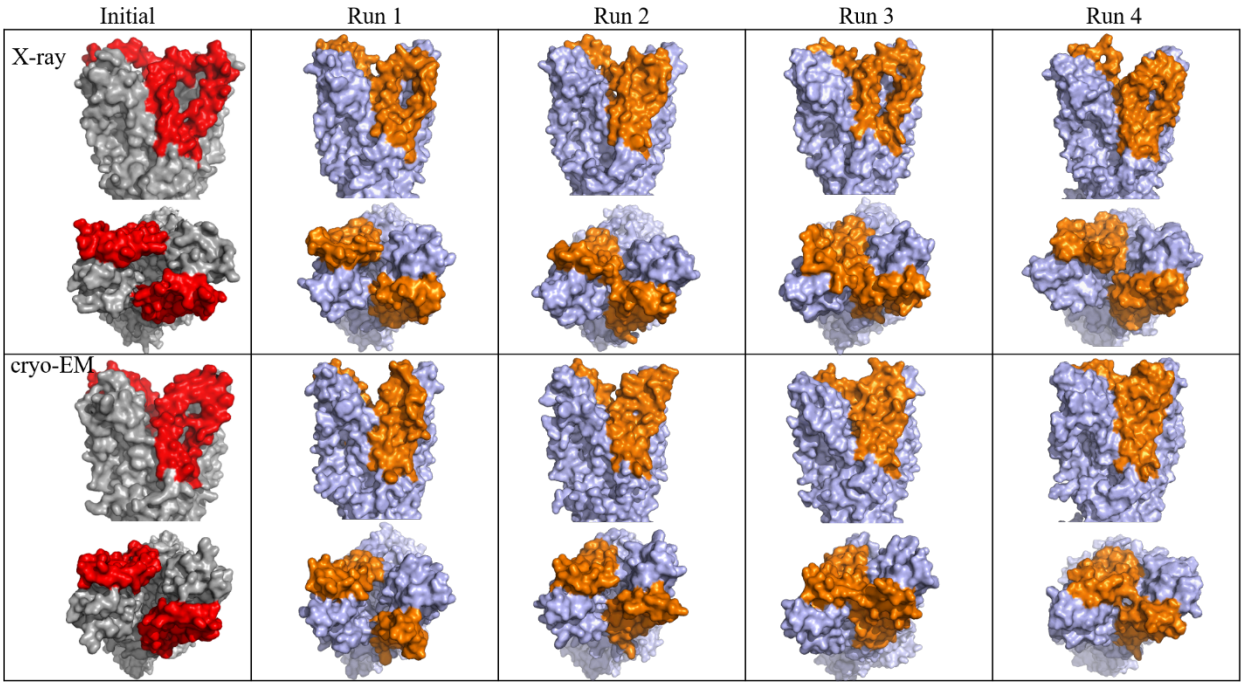


**Fig. S15. Molecular dynamic simulation results**. X-ray and cryo-EM structures are in grey and red (TM1-2). The final structures after 500 ns of simulation resulting from the four simulation runs are in light blue and orange (TM1-2). The side view (upper panel) and the top view (lower panel), from the outside of the membrane, are shown for each simulation.

**Fig. S16.**

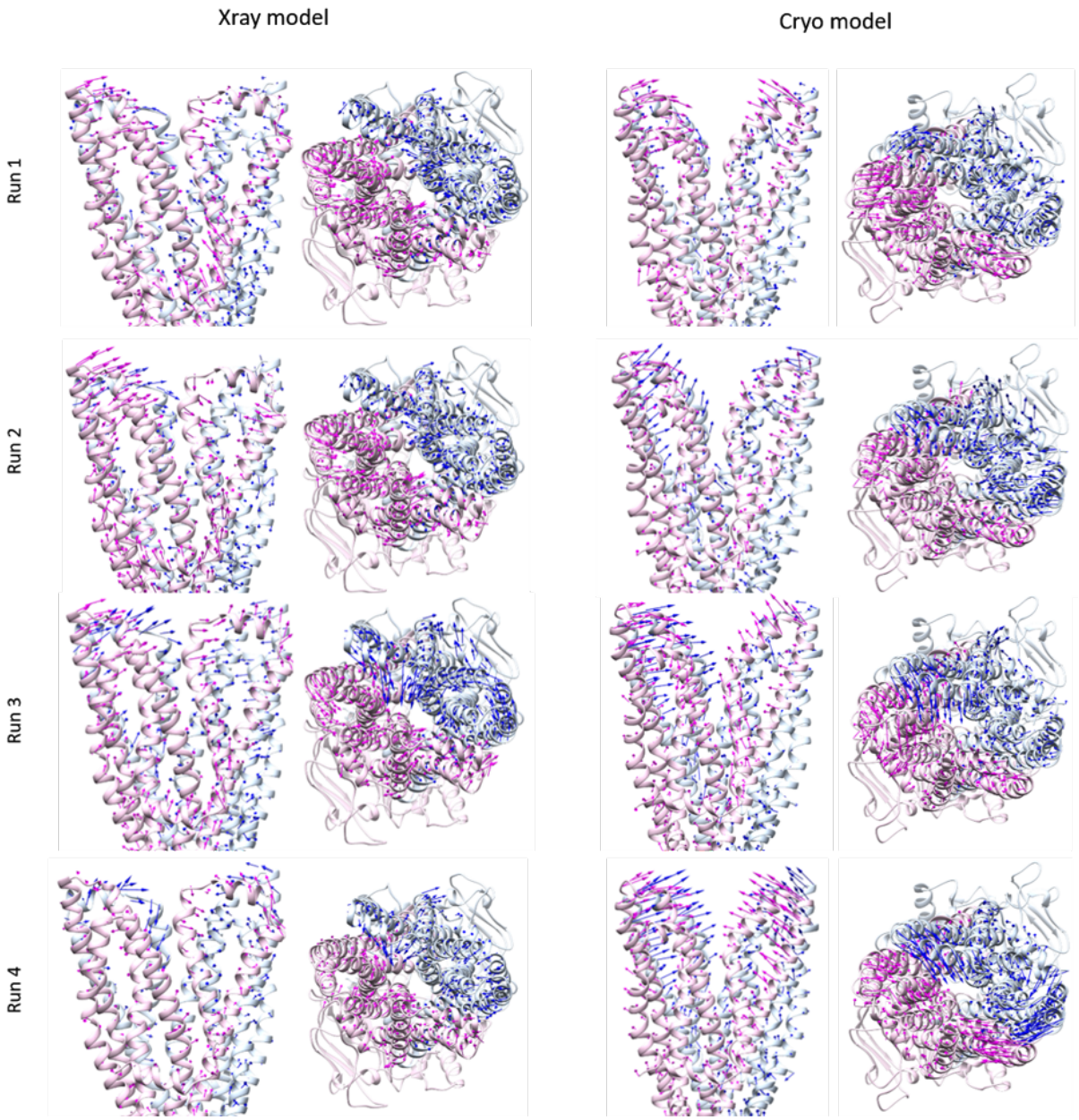


**Fig. S16.** Conformational changes of the TM region in the 8 simulations. Chain A is shown in pink and chain B in blue. Arrows indicate the displacement of the TM regions from the starting structures to the average structures.

**Fig. S17.**

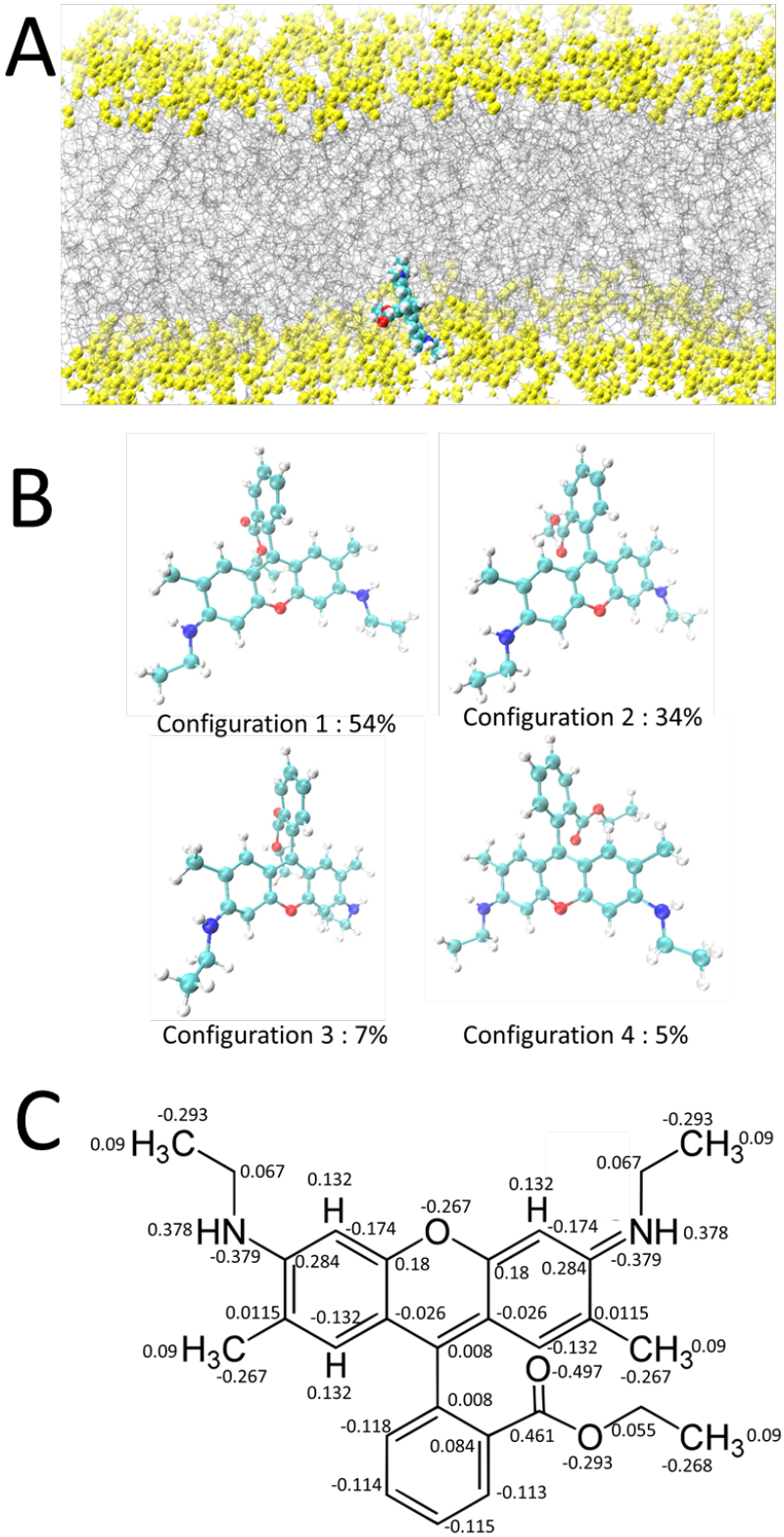


**Fig. S17. R6G parametrization.** (**A**) Snapshot from POPC:R6G simulation showing the R6G inside the lipid bilayer. (**B**) Four different conformations of R6G and their probabilities inside the membrane during the simulation run. (**C**) Weighted averages of the partial charges of R6G molecule after optimization.

**Fig. S18.**

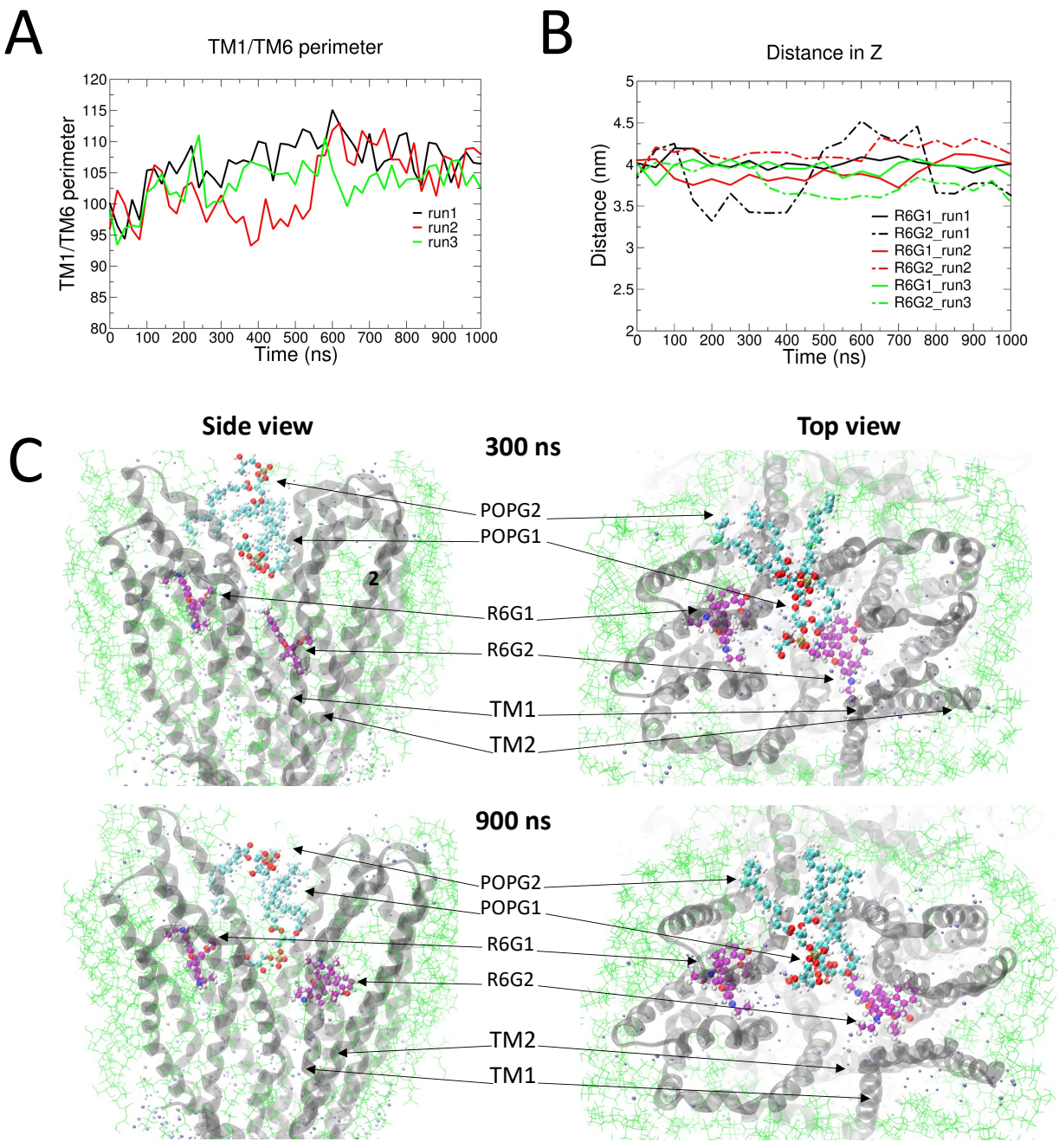


**Fig. S18. Molecular dynamics simulations of BmrA in complex with ATP-$Mg^{2+}$ and R6G.** (**A**) Time-evolution of the (Q52-G281-Q52'-G281') distance for each of the 3 simulations from cryo-EM+R6G model. (**B**) Distance between the center of mass (COM) of R6G molecules (R6G1 and R6G2) and the COM of BmrA in the three different runs. (**C**) Snapshots at 300 and 900 ns. Water is colored in ice blue and lipids in green. POPG1 and POPG2 invading the drug-binding pocket are in cyan balls and sticks

**Fig. S19.**

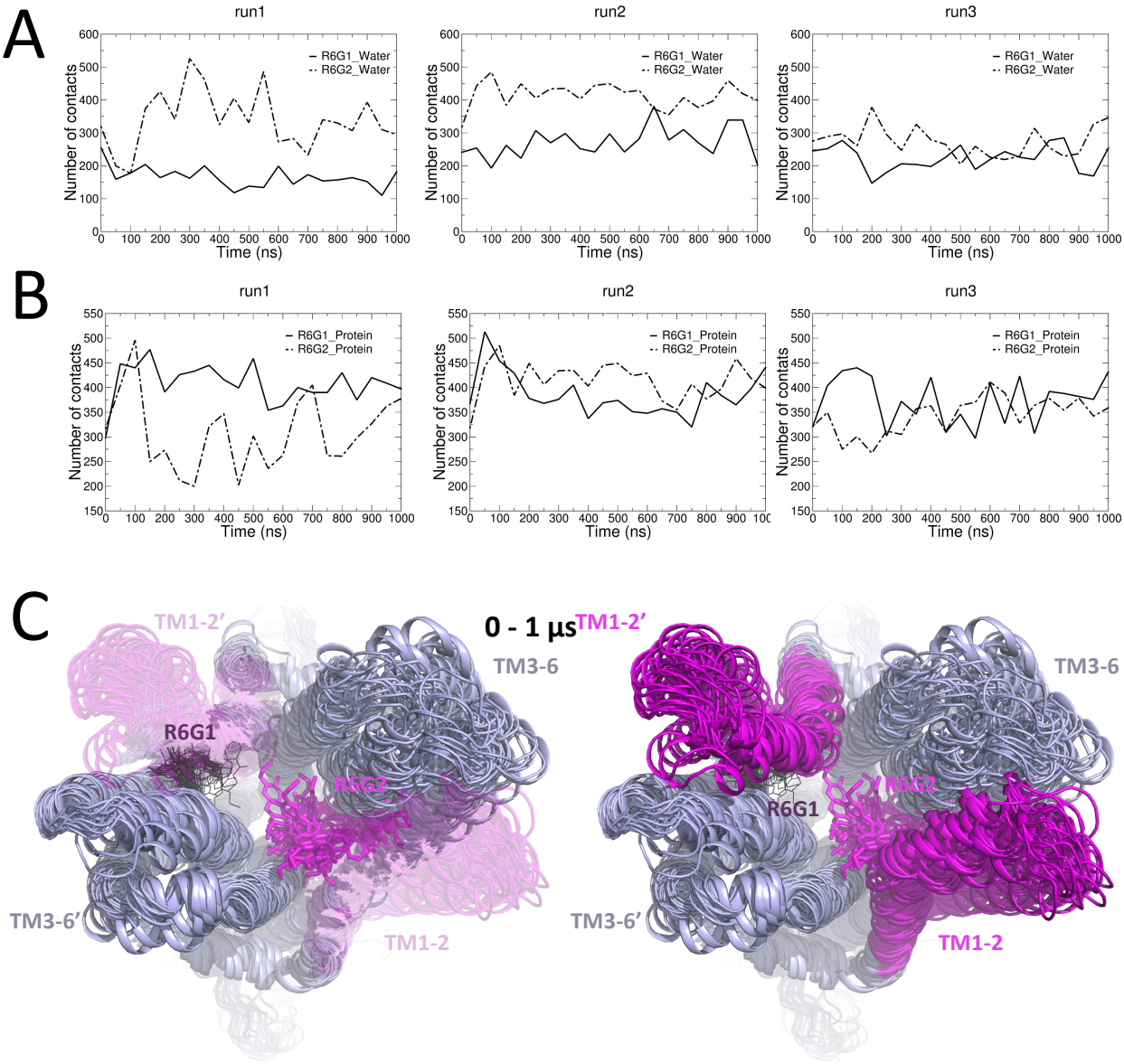


**Fig. S19. Molecular dynamics simulations of BmrA in complex with ATP-$Mg^{2+}$ and R6G. (A)** Number of contacts between the COM of R6G and water molecules in the three replicates. (**B**). Number of contacts between R6G molecules and BmrA in the three runs. (**C**) Overlay of every 50-ns snapshot over 1-µs simulation. BmrA is seen from the periplasmic side looking down the cavity. TM1 and 2 are transparent on the left panel to better see the R6G2 molecule movement. R6G1 is displayed in black magenta wireframe and R6G2 in magenta sticks.

**Table S1.** X-ray statistics.

| X-ray | Non-corrected data | Corrected data |
|---|---|---|
| Data collection | | |
| Space group | $P2_1$ | $P2_1$ |
| Cell dimensions | | |
| *a*, *b*, *c* (Å) | 117.8, 110.8, 155.6 | 117.8, 110.8, 155.6 |
| $\alpha, \beta, \gamma$ (°) | 90,93.2,90 | 90,93.2,90 |
| Resolution (Å) | 48.6-3.92(4.3-3.95)[a] | 80.6-3.95(4.3-3.95) |
| $R_{merge}$ | 0.068(3.7) | -(-) |
| $I/\sigma$ | 11.58(1.39) | 11.65(1.39) |
| Completeness (%) | 56.5(11.0) | 92(71.5) |
| Redundancy | 3.5(3.4) | -(-) |
| Ellipsoid[b] | | 0.851 a* + 0.525 c*<br>b*<br>-0.36 a* + 0.933 c* |
| Refinement | | |
| Resolution (Å) | | 28.5-3.95 |
| No. reflections | | 20484 |
| $R_{work}$/ $R_{free}$ | | 26.0/32.1 |
| No. atoms | | 17680 |
| Protein | | 17552 |
| Ligand/ion | | 128 |
| B-factors (Å$^2$) | | |
| Protein | | 114.4 |
| Ligand/ion | | 47.3 |
| R.m.s deviations | | |
| Bond lengths (Å) | | 0.013 |
| Bond angles (º) | | 1.97 |
| Ramachandran (%) | | |
| Favored | | 92.26 |
| Allowed | | 7.39 |
| Outliers | | 0.35 |

[a] Highest resolution shell is shown in parenthesis.

[b] Definition of ellipsoid: Data has been fitted to the ellipsoid defined by the following parameters:

Ellipsoid definition: 0.1742 0.2691 0.2191 2.0533

Diffraction limits & principal axes of ellipsoid fitted to diffraction cut-off surface:

| | | | | |
|---|---|---|---|---|
| 4.564 | 0.8858 | 0.0000 | 0.4640 | 0.851 _a_* + 0.525 _c_* |
| 3.717 | -0.0000 | 1.0000 | -0.0000 | _b_* |
| 5.739 | -0.4640 | -0.0000 | 0.8858 | -0.360 _a_* + 0.933 _c_* |

Worst diffraction limit after cut-off:

5.976 at reflection -1 1 26 in direction -0.038 _a_* + 0.038 _b_* + 0.999 _c_*

Best diffraction limit after cut-off:

3.917 at reflection -2 28 5 in direction -0.070 _a_* + 0.982 _b_* + 0.175 _c_*

**Table S2**. Cryo-EM data collection and refinement statistics.

| | EMDB-12170<br>PDB: 7bg4 | EMDB-4749<br>PDB: 6r81 | EMDB-13095<br>PDB: 7ow8 |
|---|---|---|---|
| **Data collection and processing** | | | |
| Magnification | 130000 | 130000 | 130000 |
| Voltage (kV) | 300 | 300 | 300 |
| Electron exposure (e–/Å$^2$) | 38.4 | 38.4 | 37.95 |
| Defocus range (μm) | 1.2 to 3.2 | 1.2 to 3.2 | 0.8 to 2.2 |
| Pixel size (Å) | 1.06 | 1.06 | 1.052 |
| Symmetry imposed | C1 | C2 | C2 |
| Initial particle images (no.) | 486404 | 486404 | 511984 |
| Final particle images (no.) | 128372 | 128372 | 327764 |
| Map resolution (Å) | 4.2 | 3.9 | 3.6 |
| FSC threshold | 0.143 | 0.143 | 0.143 |
| Map resolution range (Å) | 3.6 to 25 | 3.5 to 9.1 | 3.0 to 6.0 |
| | | | |
| **Refinement** | | | |
| Initial model used (PDB code) | 6R81 | 6R72 | 6R72 |
| Model resolution (Å) | 4.3 | 4.2 | 3.8 |
| FSC threshold | 0.5 | 0.5 | 0.5 |
| Model resolution range (Å) | 3.6 to 7.6 | 3.6 to 7.6 | 3.5 to 3.7 |
| Map sharpening *B* factors (Å$^2$)[a] | 187, 238 | 187, 218 | 217 |
| Model composition | | | |
| Non-hydrogen atoms | 8927 | 8861 | 8942 |
| Protein residues | 1141 | 1141 | 1154 |
| Ligands | 6 | 4 | 4 |
| *B* factors (Å$^2$) | | | |
| Protein | 95.8 | 170 | 94.6 |
| Ligand | 109 | 153 | 62.9 |
| R.m.s. deviations | | | |
| Bond lengths (Å) | 0.004 | 0.011 | 0.011 |
| Bond angles (°) | 0.834 | 1.61 | 1.608 |
| Validation | | | |
| MolProbity score | 2.24 | 2.33 | 2.43 |
| Clashscore | 16.2 | 14.1 | 10.2 |
| Poor rotamers (%) | 0.21 | 1.25 | 4.22 |
| | | | |
| Ramachandran plot | | | |
| Favored (%) | 90.6 | 88.1 | 93.6 |
| Allowed (%) | 9.40 | 11.5 | 6.3 |
| Disallowed (%) | 0.00 | 0.40 | 0.17 |

[a] Note that 2 different map sharpening levels were used to aid model building.

**Data S1. (separate file)**
Detergent quantitation.

**Data S2. (separate file)**
Thermostability assays.

**Rhodamine6G.itp (separate file)**
R6G parametrization

**ForcefieldR6G.itp (separate file)**
*In silico* system (BmrA, ATP-$Mg^{2+}$, R6G, POPG, POPE, water, KCl) parametrization file.

## REFERENCES AND NOTES


1. O. Jardetzky, Simple allosteric model for membrane pumps. *Nature* **211**, 969–970 (1966).

2. K. Linton, C. Higgins, Structure and function of ABC transporters: The ATP switch provides flexible control. *Pflügers Arch.* **453**, 555–567 (2007).

3. K. P. Locher, Mechanistic diversity in ATP-binding cassette (ABC) transporters. *Nat. Struct. Mol. Biol.* **23**, 487–493 (2016).

4. Y. Kim, J. Chen, Molecular structure of human P-glycoprotein in the ATP-bound, outward-facing conformation. *Science* **359**, 915–919 (2018).

5. R. J. Dawson, K. P. Locher, Structure of a bacterial multidrug ABC transporter. *Nature* **443**, 180–185 (2006).

6. A. Ward, C. L. Reyes, J. Yu, C. B. Roth, G. Chang, Flexibility in the ABC transporter MsbA: Alternating access with a twist. *Proc. Natl. Acad. Sci.* **104**, 19005–19010 (2007).

7. A. B. Ward, P. Szewczyk, V. Grimard, C.W. Lee, L. Martinez, R. Doshi, A. Caya, M. Villaluz, E. Pardon, C. Cregger, D. J. Swartz, P. G. Falson, I. L. Urbatsch, C. Govaerts, J. Steyaert, G. Chang, Structures of P-glycoprotein reveal its conformational flexibility and an epitope on the nucleotide-binding domain. *Proc. Natl. Acad. Sci. U.S.A.* **110**, 13386–13391 (2013).

8. H. G. Choudhury, Z. Tong, I. Mathavan, Y. Li, S. Iwata, S. Zirah, S. Rebuffat, H. W. van Veen, K. Beis, Structure of an antibacterial peptide ATP-binding cassette transporter in a novel outward occluded state. *Proc. Natl. Acad. Sci. U.S.A.* **111**, 9145–9150 (2014).

9. A. Blees, D. Januliene, T. Hofmann, N. Koller, C. Schmidt, S. Trowitzsch, A. Moeller, R. Tampé, Structure of the human MHC-I peptide-loading complex. *Nature* **551**, 525–528 (2017).

10. Z. L. Johnson, J. Chen, Structural basis of substrate recognition by the multidrug resistance protein MRP1. *Cell* **168**, 1075–1085.e9 (2017).

11. K. Bountra, G. Hagelueken, H. G. Choudhury, V. Corradi, K. el Omari, A. Wagner, I. Mathavan, S. Zirah, W. Yuan Wahlgren, D. P. Tieleman, O. Schiemann, S. Rebuffat, K. Beis, Structural basis for antibacterial peptide self-immunity by the bacterial ABC transporter McjD. *EMBO J.* **36**, 3062–3079 (2017).

12. H. Göddeke, M. H. Timachi, C. A. J. Hutter, L. Galazzo, M. A. Seeger, M. Karttunen, E. Bordignon, L. V. Schäfer, Atomistic mechanism of large-scale conformational transition in a heterodimeric ABC exporter. *J. Am. Chem. Soc.* **140**, 4543–4551 (2018).

13. S. Hofmann, D. Januliene, A. R. Mehdipour, C. Thomas, E. Stefan, S. Brüchert, B. T. Kuhn, E. R. Geertsma, G. Hummer, R. Tampé, A. Moeller, Conformation space of a heterodimeric ABC exporter under turnover conditions. *Nature* **571**, 580–583 (2019).

14. A. Alam, J. Kowal, E. Broude, I. Roninson, K. P. Locher, Structural insight into substrate and inhibitor discrimination by human P-glycoprotein. *Science* **363**, 753–756 (2019).

15. A. Kodan, T. Yamaguchi, T. Nakatsu, K. Matsuoka, Y. Kimura, K. Ueda, H. Kato, Inward- and outward-facing X-ray crystal structures of homodimeric P-glycoprotein CmABCB1. *Nat. Commun.* **10**, 88 (2019).

16. W. Mi, Y. Li, S. H. Yoon, R. K. Ernst, T. Walz, M. Liao, Structural basis of MsbA-mediated lipopolysaccharide transport. *Nature* **549**, 233–237 (2017).

17. O. Lewinson, C. Orelle, M. A. Seeger, Structures of ABC transporters: Handle with care. *FEBS Lett.* **594**, 3799–3814 (2020).

18. R. L. Juliano, V. Ling, A surface glycoprotein modulating drug permeability in Chinese hamster ovary cell mutants. *Biochim. Biophys. Acta* **455**, 152–162 (1976).

19. Z. L. Johnson, J. Chen, ATP binding enables substrate release from multidrug resistance protein 1. *Cell* **172**, 81–89.e10 (2018).

20. R. X. Gu, V. Corradi, G. Singh, H. G. Choudhury, K. Beis, D. P. Tieleman, Conformational changes of the antibacterial peptide ATP binding cassette transporter McjD revealed by molecular dynamics simulations. *Biochemistry* **54**, 5989–5998 (2015).

21. C. Thomas, R. Tampé, Structural and mechanistic principles of ABC transporters. *Annu. Rev. Biochem.* **89**, 605–636 (2020).

22. C. Thomas, S. G. Aller, K. Beis, E. P. Carpenter, G. Chang, L. Chen, E. Dassa, M. Dean, F. Duong van Hoa, D. Ekiert, R. Ford, R. Gaudet, X. Gong, I. B. Holland, Y. Huang, D. K. Kahne, H. Kato, V. Koronakis, C. M. Koth, Y. Lee, O. Lewinson, R. Lill, E. Martinoia, S. Murakami, H. W. Pinkett, B. Poolman, D. Rosenbaum, B. Sarkadi, L. Schmitt, E. Schneider, Y. Shi, S.L. Shyng, D. J. Slotboom, E. Tajkhorshid, D. P. Tieleman, K. Ueda, A. Váradi, P.C. Wen, N. Yan, P. Zhang, H. Zheng, J. Zimmer, R. Tampé, Structural and functional diversity calls for a new classification of ABC transporters. *FEBS Lett.* **594**, 3767–3775 (2020).

23. E. Steinfels, C. Orelle, J.R. Fantino, O. Dalmas, J.L. Rigaud, F. Denizot, A. di Pietro, J.M. Jault, Characterization of YvcC (BmrA), a multidrug ABC transporter constitutively expressed in *Bacillus subtilis*. *Biochemistry* **43**, 7491–7502 (2004).

24. H. Krügel, A. Licht, G. Biedermann, A. Petzold, J. Lassak, Y. Hupfer, B. Schlott, C. Hertweck, M. Platzer, S. Brantl, H.P. Saluz, Cervimycin C resistance in *Bacillus subtilis* is due to a promoter up-mutation and increased mRNA stability of the constitutive ABC-transporter gene bmrA. *FEMS Microbiol. Lett.* **313**, 155–163 (2010).

25. C. Orelle, O. Dalmas, P. Gros, A. Di Pietro, J. M. Jault, The conserved glutamate residue adjacent to the Walker-B motif is the catalytic base for ATP hydrolysis in the ATP-binding cassette transporter BmrA. *J. Biol. Chem.* **278**, 47002–47008 (2003).

26. H. W. van Veen, K. Venema, H. Bolhuis, I. Oussenko, J. Kok, B. Poolman, A. J. Driessen, W. N. Konings, Multidrug resistance mediated by a bacterial homolog of the human multidrug transporter MDR1. *Proc. Natl. Acad. Sci. U.S.A.* **93**, 10668–10672 (1996).

27. S. Nim, L. G. Lobato, A. Moreno, V. Chaptal, M. K. Rawal, P. Falson, R. Prasad, Atomic modelling and systematic mutagenesis identify residues in multiple drug binding sites that are essential for drug resistance in the major *Candida* transporter Cdr1. *Biochim. Biophys. Acta* **1858**, 2858–2870 (2016).

28. R. Ernst, P. Kueppers, C. M. Klein, T. Schwarzmueller, K. Kuchler, L. Schmitt, A mutation of the H-loop selectively affects rhodamine transport by the yeast multidrug ABC transporter Pdr5. *Proc. Natl. Acad. Sci. U.S.A.* **105**, 5069–5074 (2008).

29. M. Ahmed, L. Lyass, P. N. Markham, S. S. Taylor, N. Vázquez-Laslop, A. A. Neyfakh, Two highly similar multidrug transporters of *Bacillus subtilis* whose expression is differentially regulated. *J. Bacteriol.* **177**, 3904–3910 (1995).

30. H. Sjuts, A. V. Vargiu, S. M. Kwasny, S. T. Nguyen, H.S. Kim, X. Ding, A. R. Ornik, P. Ruggerone, T. L. Bowlin, H. Nikaido, K. M. Pos, T. J. Opperman, Molecular basis for inhibition of AcrB multidrug efflux pump by novel and powerful pyranopyridine derivatives. *Proc. Natl. Acad. Sci. U.S.A.* **113**, 3509–3514 (2016).

31. C. Orelle, F. Gubellini, A. Durand, S. Marco, D. Lévy, P. Gros, A. di Pietro, J.M. Jault, Conformational change induced by ATP binding in the multidrug ATP-binding cassette transporter BmrA. *Biochemistry* **47**, 2404–2412 (2008).

32. S. G. Aller, J. Yu, A. Ward, Y. Weng, S. Chittaboina, R. Zhuo, P. M. Harrell, Y. T. Trinh, Q. Zhang, I. L. Urbatsch, G. Chang, Structure of P-glycoprotein reveals a molecular basis for poly-specific drug binding. *Science* **323**, 1718–1722 (2009).

33. V. Chaptal, F. Delolme, A. Kilburg, S. Magnard, C. Montigny, M. Picard, C. Prier, L. Monticelli, O. Bornert, M. Agez, S. Ravaud, C. Orelle, R. Wagner, A. Jawhari, I. Broutin, E. Pebay-Peyroula, J.M. Jault, H. R. Kaback, M. le Maire, P. Falson, Quantification of detergents complexed with membrane proteins. *Sci. Rep.* **7**, 41751 (2017).

34. K. A. Nguyen, M. Peuchmaur, S. Magnard, R. Haudecoeur, C. Boyère, S. Mounien, I. Benammar, V. Zampieri, S. Igonet, V. Chaptal, A. Jawhari, A. Boumendjel, P. Falson, Glycosyl-substituted dicarboxylates as detergents for the extraction, overstabilization, and crystallization of membrane proteins. *Angew. Chem. Int. Ed. Engl.* **57**, 2948–2952 (2018).

35. D. Lacabanne, C. Orelle, L. Lecoq, B. Kunert, C. Chuilon, T. Wiegand, S. Ravaud, J.M. Jault, B. H. Meier, A. Böckmann, Flexible-to-rigid transition is central for substrate transport in the ABC transporter BmrA from *Bacillus subtilis*. *Commun. Biol.* **2**, 149 (2019).

36. F. J. Alvarez, C. Orelle, A. L. Davidson, Functional reconstitution of an ABC transporter in nanodiscs for use in electron paramagnetic resonance spectroscopy. *J. Am. Chem. Soc.* **132**, 9513–9515 (2010).

37. S. Shukla, V. Rai, D. Banerjee, R. Prasad, Characterization of Cdr1p, a major multidrug efflux protein of *Candida albicans*: Purified protein is amenable to intrinsic fluorescence analysis. *Biochemistry* **45**, 2425–2435 (2006).

38. C. A. J. Hutter, M. H. Timachi, L. M. Hürlimann, I. Zimmermann, P. Egloff, H. Göddeke, S. Kucher, S. Štefanić, M. Karttunen, L. V. Schäfer, E. Bordignon, M. A. Seeger, The extracellular gate shapes the energy profile of an ABC exporter. *Nat. Commun.* **10**, 2260 (2019).

39. S. Mehmood, C. Domene, E. Forest, J. M. Jault, Dynamics of a bacterial multidrug ABC transporter in the inward- and outward-facing conformations. *Proc. Natl. Acad. Sci. U.S.A.* **109**, 10832–10836 (2012).

40. P. C. Wen, B. Verhalen, S. Wilkens, H. S. McHaourab, E. Tajkhorshid, On the origin of large flexibility of P-glycoprotein in the inward-facing state. *J. Biol. Chem.* **288**, 19211–19220 (2013).

41. K. Barth, S. Hank, P. E. Spindler, T. F. Prisner, R. Tampé, B. Joseph, Conformational coupling and trans-inhibition in the human antigen transporter ortholog TmrAB resolved with dipolar EPR spectroscopy. *J. Am. Chem. Soc.* **140**, 4527–4533 (2018).

42. M. H. Timachi, C. A.J. Hutter, M. Hohl, T. Assafa, S. Böhm, A. Mittal, M. A. Seeger, E. Bordignon, Exploring conformational equilibria of a heterodimeric ABC transporter. *eLife* **6**, e20236 (2017).

43. F. Husada, K. Bountra, K. Tassis, M. Boer, M. Romano, S. Rebuffat, K. Beis, T. Cordes, Conformational dynamics of the ABC transporter McjD seen by single-molecule FRET. *EMBO J.* **37**, e100056 (2018).

44. V. Debruycker, A. Hutchin, M. Masureel, E. Ficici, C. Martens, P. Legrand, R. A. Stein, H. S. Mchaourab, J. D. Faraldo-Gómez, H. Remaut, C. Govaerts, An embedded lipid in the multidrug transporter LmrP suggests a mechanism for polyspecificity. *Nat. Struct. Mol. Biol.* **27**, 829–835 (2020).

45. M. O. Jensen, D. W. Borhani, K. Lindorff-Larsen, P. Maragakis, V. Jogini, M. P. Eastwood, R. O. Dror, D. E. Shaw, Principles of conduction and hydrophobic gating in K+ channels. *Proc. Natl. Acad. Sci. U.S.A.* **107**, 5833–5838 (2010).

46. P. P. Borbat, K. Surendhran, M. Bortolus, P. Zou, J. H. Freed, H. S. Mchaourab, Conformational motion of the ABC transporter MsbA induced by ATP hydrolysis. *PLoS Biol.* **5**, e271 (2007).

47. M. Yang, N. Livnat Levanon, B. Acar, B. Aykac Fas, G. Masrati, J. Rose, N. Ben-Tal, T. Haliloglu, Y. Zhao, O. Lewinson, Single-molecule probing of the conformational homogeneity of the ABC transporter BtuCD. *Nat. Chem. Biol.* **14**, 715–722 (2018).

48. B. Wiseman, A. Kilburg, V. Chaptal, G. C. Reyes-Mejia, J. Sarwan, P. Falson, J.M. Jault, Stubborn contaminants: Influence of detergents on the purity of the multidrug ABC transporter BmrA. *PLOS ONE* **9**, e114864 (2014).

49. E. Heftmann, S. T. Ko, R. D. Bennett, Response of steroids to sulfuric acid in thin-layer chromatography. *J. Chromatogr.* **21**, 490–494 (1966).

50. C. M. Hebling, C. R. Morgan, D. W. Stafford, J. W. Jorgenson, K. D. Rand, J. R. Engen, Conformational analysis of membrane proteins in phospholipid bilayer nanodiscs by hydrogen exchange mass spectrometry. *Anal. Chem.* **82**, 5415–5419 (2010).

51. A. M. Lau, J. Claesen, K. Hansen, A. Politis, Deuteros 2.0: Peptide-level significance testing of data from hydrogen deuterium exchange mass spectrometry. *Bioinformatics* **37**, 270–272 (2021).

52. Y. Perez-Riverol, A. Csordas, J. Bai, M. Bernal-Llinares, S. Hewapathirana, D. J. Kundu, A. Inuganti, J. Griss, G. Mayer, M. Eisenacher, E. Pérez, J. Uszkoreit, J. Pfeuffer, T. Sachsenberg, Ş. Yılmaz, S. Tiwary, J. Cox, E. Audain, M. Walzer, A. F. Jarnuczak, T. Ternent, A. Brazma, J. A. Vizcaíno, The PRIDE database and related tools and resources in 2019: Improving support for quantification data. *Nucleic Acids Res.* **47**, D442–D450 (2019).

53. J. Y. Lee, J. G. Yang, D. Zhitnitsky, O. Lewinson, D. C. Rees, Structural basis for heavy metal detoxification by an Atm1-type ABC exporter. *Science* **343**, 1133–1136 (2014).

54. L. Zimmermann, A. Stephens, S.Z. Nam, D. Rau, J. Kübler, M. Lozajic, F. Gabler, J. Söding, A. N. Lupas, V. Alva, A completely reimplemented MPI bioinformatics toolkit with a new HHpred server at its core. *J. Mol. Biol.* **430**, 2237–2243 (2018).

55. M. A. Lomize, I. D. Pogozheva, H. Joo, H. I. Mosberg, A. L. Lomize, OPM database and PPM web server: Resources for positioning of proteins in membranes. *Nucleic Acids Res.* **40**, D370–D376 (2012).

56. J. Lee, X. Cheng, J. M. Swails, M. S. Yeom, P. K. Eastman, J. A. Lemkul, S. Wei, J. Buckner, J. C. Jeong, Y. Qi, S. Jo, V. S. Pande, D. A. Case, C. L. Brooks III, A. D. MacKerell Jr, J. B. Klauda, W. Im, CHARMM-GUI input generator for NAMD, GROMACS, AMBER, OpenMM, and CHARMM/OpenMM simulations using the CHARMM36 additive force field. *J. Chem. Theory Comput.* **12**, 405–413 (2016).

57. B. Hess, C. Kutzner, D. van der Spoel, E. Lindahl, GROMACS 4: Algorithms for highly efficient, load-balanced, and scalable molecular simulation. *J. Chem. Theory Comput.* **4**, 435–447 (2008).

58. U. Essmann, L. Perera, M. L. Berkowitz, T. Darden, H. Lee, L. G. Pedersen, A smooth particle mesh Ewald method. *J. Chem. Phys.* **103**, 8577–8593 (1995).

59. S. Páll, B. Hess, A flexible algorithm for calculating pair interactions on SIMD architectures. *Comput. Phys. Commun.* **184**, 2641–2650 (2013).

60. G. Bussi, D. Donadio, M. Parrinello, Canonical sampling through velocity rescaling. *J. Chem. Phys.* **126**, 014101 (2007).

61. M. Parrinello, A. Rahman, Polymorphic transitions in single crystals: A new molecular dynamics method. *J. Appl. Phys.* **52**, 7182–7190 (1981).

62. K. Vanommeslaeghe, E. Hatcher, C. Acharya, S. Kundu, S. Zhong, J. Shim, E. Darian, O. Guvench, P. Lopes, I. Vorobyov, Mackerell AD Jr, CHARMM general force field: A force field for drug-like molecules compatible with the CHARMM all-atom additive biological force fields. *J. Comput. Chem.* **31**, 671–690 (2010).